Quantum interface

—

A fiber cavity perpendicular to a linear ion trap

DISSERTATION

zur Erlangung des Grades

DOCTOR OF PHILOSOPHY

an der Fakultät für
Mathematik, Informatik und Physik
der Leopold-Franzens-Universität Innsbruck

vorgelegt von
KLEMENS SCHÜPPERT

durchgeführt am Institut für Experimentalphysik
unter der Leitung von
o. Univ.-Prof. Dr. Rainer Blatt und Univ.-Prof. Dr. Tracy E. Northup

2020

Kurzfassung

Quantennetzwerken werden vielseitige Answendungsmöglichkeiten für Quantenmesstechnik, -kommunikation, -simulation und -computer zugesprochen. Solche Netzwerke bestehen aus Quantenknoten, die über Quantenkanäle und klassische Kanäle verbunden sind. Die dafür notwendigen Schnittstellen sind grundlegende Bausteine dieser Quantennetzwerke und verbinden die stationären Qubits, die in Knoten lokalisiert sind, mit fliegenden Qubits, die sich durch Quantenkanäle bewegen. Gefangene Ionen in optischen Hohlraumresonatoren sind ein vielversprechender Ansatz für Quantenschnittstellen, da Ionen nachweislich eine effiziente Initialisierung, kohärente Manipulation und Auslesung von Quantenzuständen ermöglichen und weiters die Hohlraumresonatoren die stationären Ionen effizient mit fliegenden Photonen verbinden. Wir beabsichtigen ein Ionenfallen-System mit einem Faserhohlraumresonator senkrecht zur Achse einer linearen Paul-Falle zu verwenden, um mehrere Ionen stark mit dem Lichtfeld des Hohlraumresonators zu koppeln. Aufgrund ihres kleinen Modenvolumens ermöglichen mikrofabrizierte Faserhohlraumresonatoren das Regime der starken Kopplung zu erreichen, wodurch eine Quantenkommunikation mit hoher Güte und gleichzeitig hoher Effizienz durchgeführt werden kann.

Diese Arbeit berichtet über die Entwicklung unseren Ionen-Faserhohlraumresonator Systems. Wir stellten Faserspiegel her, die für Längen von 400–500 µm des Hohlraumresonators optimiert sind. Eine dreidimensionale lineare Ionenfalle wurde entworfen, um darin solch einen Faserhohlraumresonator zu integrieren. Nach dem Aufbau und der Charakterisierung des Systems koppelten wir erfolgreich ein gefangenes Ion mit dem Lichtfeld des Hohlraumresonators. Ladungen auf den Fasern hinderten uns jedoch daran, diese Kopplung weiter zu optimieren. Nach kurzer Zeit waren wir nicht mehr in der Lage Ionen im Hohlraumresonator zu speichern.

Ladungen auf den Fasern stören das Fallenpotential und wenn die Fasern verschoben werden, ändern sich die Gleichgewichtsposition und die säkularen Bewegungsfrequenzen des Ions. Wir haben diese beiden Parameter für verschiedene Positionen der Fasern gemessen und diese Messungen mit Simulationen verglichen, bei denen unbekannte Ladungsdichten auf den Fasern einstellbare Parameter waren. Unter Verwendung eines Modells, das auf zwei homogenen Oberflächenladungsflächen pro Faser basiert, wurden Werte im Bereich von -10 bis +50 $e/\mu\mathrm{m}^2$ bestimmt.

Da die Ladungen auf unseren Fasern uns zwangen, einen gewissen Abstand zwischen Fasern und Ionen zu verwenden, wollten wir die Ionen-Photonen-Kopplung für eine bestimmte Länge des Hohlraumresonators optimieren. Durch einen verbesserten CO_2-Laser-Ablationsprozess konnten wir den Hohlraumresonator bestehend aus unseren Faserspiegeln dem konzentrischen Regime annähern. Messungen in diesem Regime zeigten eine dreimal höhere erwartete Kooperativität im Vergleich zu einem Hohlraumresonator im konfokalen Regime, der in Experimenten nach dem Stand der Technik üblich wäre. Dies bedeutet, dass die Ionen-Photonen-Kopplung im Vergleich zum Atomzerfall und dem Zerfall des Lichtfeldes im Hohlraumresonators verbessert wurde.

Abstract

Quantum networks promise versatile resources for quantum sensing, communication, simulation and computation. They are made out of quantum nodes connected via quantum and classical channels. Interfaces between stationary qubits localized in nodes and flying qubits traveling through quantum channels are fundamental building blocks for such quantum networks. Trapped ions in optical cavities are a promising approach for quantum interfaces, as ions have proven to provide efficient initialization, coherent manipulation, and readout of quantum states and cavities interconnect the stationary ions with flying photons efficiently. To strongly couple multiple ions with the light field of the cavity, we intend to use an ion-trap system with a fiber cavity perpendicular to the axis of a linear Paul trap. Due to their small mode volume, micro-fabricated fiber cavities enable access to the strong coupling regime, allowing quantum communication to be carried out with high fidelity and efficiency at the same time.

This thesis reports on the development of our ion-cavity system. We fabricated fiber mirrors optimized for cavity lengths of 400–$500\ \mu\mathrm{m}$. A three dimensional linear ion trap was designed to host such a fiber cavity. After building and characterizing the ion-cavity system, we successfully coupled a trapped ion with the cavity light field. However, charges on the fibers prevent us to improve this coupling. Later, we were no longer able to store ions inside the cavity.

Charges on fibers distort the trapping potential, and when the fibers are displaced, the ion's equilibrium position and secular motional frequencies are altered. We measured the latter quantities for different positions of the fibers and compared these measurements to simulations in which unknown charge densities on the fibers were adjustable parameters. Using a model based on two homogeneous surface charge areas per fiber, values ranging from -10 to +50 $e/\mu\mathrm{m}^2$ were determined.

As charges on our fibers restrict us to use a sufficient clearance between fibers and ions, we wanted to optimize the ion-photon coupling for a chosen cavity length. Due to an improved CO_2-laser ablation process, we are able to approach the concentric regime with our fiber mirrors. Measurements in this regime showed a three times higher expected cooperativity compared to a cavity in the confocal regime, which is common in state-of-the-art experiments. This means that the ion-photon coupling would be enhanced compared to the atom and cavity decays.

Contents

Chapter 1

Introduction

Today, we live in a fast-developing world impelled by the digital age. Our social life is connected closer and closer to the virtual world via the Internet, smartphones, social media, smart homes, and smart cities. Our industry is evolving to fully computerized factories enabled by the Internet of Things, cloud computing and artificial intelligence, so that every part of a production plant is connected and digitalized. Our academic and applied research is supported by supercomputers, big data, and, broadly speaking, information technology. This entire digital revolution is based on billions of modern computers, each one consisting of billions of transistors. One could claim that the transistor is the fundamental building block of today's social, economic, and scientific progress.

The origins of the transistor go back to the year 1900, when M. Planck derived the blackbody radiation law; A. Einstein discovered "the law of the photoelectric effect" only five years later[1]. Neither physical effect could be explained by classical physics. Driven by these discoveries, N. Bohr, W. Heisenberg, E. Schrödinger and others formulated the quantum theory in the 1920s. Several applications were deduced from the insights of quantum mechanics, so that this milestone was later called the first quantum revolution. Among other inventions based on quantum mechanics, the first blueprint of a transistor was patented by Julien Lilienfeld in 1926 [1]. Thirty years later, W. Shockley, J. Bardeen and W. Brattain were honored with the 1956 Nobel Prize in Physics for the first realization of such a transistor.

From then on, the transistor was quickly developed into a commercial product, starting the digital revolution. In 1965, G. Moore described the speed of this evolution with his famous "Moore's law" [2], stating that the number of transistors per unit area doubles every two years. Computer hardware obeyed this law for over 40 years, until G. Moore himself predicted the end of his law:

> *It can't continue forever. The nature of exponentials is that you push them out and eventually disaster happens. In terms of size [of transistor] you can see that we're approaching the size of atoms which is a fundamental barrier, but it'll be two or three generations before we get that far - but that's as far out as we've ever been able to see. We have another 10 to 20 years before we reach a fundamental limit. By then they'll be able to make bigger chips and have transistor budgets in the billions.*
>
> – Gordon Moore, 2010 [3]

[1] The 1918 Nobel Prize in Physics and the 1921 Nobel Prize in Physics

Since 2013, the industry has no longer been able to follow Moore's law, and the miniaturization of transistor size is running at a slower pace [4]. At the latest, the inevitable end of this progress will come at the size of single atoms, as explained by G. Moore. At the level of individual atoms, not only the desired tunneling effect of the transistor but also the entire system needs to be considered as a quantum system.

One special thing about quantum mechanical systems is that they can be in several different states at the same time. E. Schrödinger himself explained such a superposition with his famous gedankenexperiment of Schödinger's cat, which is dead and alive at the same time [5]. A quantum system with two possible states is called a quantum bit (qubit), and the state population of a qubit is described by a complex number for each state. In general, a classical description needs 2^N complex numbers to determine a quantum system with N qubits [6]. This exponential scaling shows that classical computers cannot completely describe quantum systems above some threshold, as 75 qubits already have more possible states than today's data storage capacity for the entire world. Note that certain superpositions of multiple qubits cannot be separated into superpositions of individual qubits, so that a measurement of one qubit can have immediate consequences for the measurement results of the other qubits, even if they are far apart. This "spooky action at a distance", as it was called by A. Einstein, B. Podolsky, and N. Rosen [7], is known as entanglement.

With superposition and entanglement, quantum systems have additional features compared to their classical counterparts. It is almost ironic that quantum mechanics not only describes the inevitable end of transistors at a size of single atoms but also opens up new possibilities to enrich our computational power. As scientists have developed methods to control quantum systems in their laboratories over the past decades, applications that exploit these advantages of quantum systems are now within reach. In analogy to the first quantum revolution, a second quantum revolution is predicted, and it is expected that this time, superposition and entanglement of quantum systems will be utilized [8]. Private companies, military organizations, and governmental institutes around the world are investing in the development of quantum devices. In the European Union, for example, the European Commission is supporting private companies collaborating with academic research with a "flagship" program worth one billion euros [9]. This funding is structured in four pillars, which reflect the expected future applications[2]:

I **Quantum sensors** are devices for the measurement of physical quantities through the use of quantum systems, properties or phenomena [10]. The most famous examples are atomic clocks, which have defined the second for more than 50 years [11], and thereby enable precise navigation via GPS and its European counterpart, Galileo. Further possible applications include magnetic field measurements [12] or quantum gravimeters, which are already commercially available[3].

II **Quantum communication** enables, as a first application, a provably secure method of key generation, in which attempts to eavesdrop can be detected [13]. Photons as flying qubits interconnecting remote nodes are one of the fundamental building blocks of this research field [14]. Commercial devices sending single photons over a couple of kilometers are already available[4]. Entanglement distribution over $1200\ \mathrm{km}$ via a satellite link was achieved

[2] qt.eu/discover/technology/

[3] muquans.com/

[4] ID Quantique SA, Geneva, Switzerland and MagiQ Technologies, Inc.

recently [15]. However, quantum connections via existing telecommunication infrastructure are limited due to photon losses, so that the maximal achieved length of quantum communication through an optical fiber is $404\ \mathrm{km}$ so far [16]. Quantum repeaters have been proposed [17] which promise to overcome the exponential photon loss with a polynomial scaling, thereby enabling more advanced tasks in quantum networks via distributed entanglement [18, 19] like quantum anonymous voting [20].

III **Quantum simulators** are controllable quantum systems which are used to mimic an unknown system of interest. In the early 1980s, the first ideas on quantum simulation were proposed by P. Benioff and R. Feynman [21, 22]. Today, simulations with only several tens of qubits are expected to bring important insights to investigated quantum systems for applications in materials science, biology, chemistry, or high-energy physics. In particular, with hybrid systems, where a classical computer benefits from a quantum simulator, the limit of classical computations is within reach [23].

IV **Quantum computers** are the most advanced devices in quantum information processing, as such a device would not only act as a universal quantum simulator, but also outperform classical computers in certain algorithms with a quadratic [24] or even exponential speed-up [25]. However, for the realization of a universal quantum computer, the quantum system used for computations needs to fulfill certain physical requirements [6]. In particular, the most significant outstanding challenge is to scale quantum computers beyond the capabilities of their classical counterparts.

Experiments on small-scale quantum systems of a few qubits have been carried out on several quantum systems, including photons, nuclear spins, quantum dots, superconducting circuits, and trapped ions. Notably, trapped ions have demonstrated a promising performance in all aspects of quantum information processing from the basics of initialization, manipulation and readout [26, 27] up to advanced algorithms like teleportation [28, 29], quantum memory [30] and quantum error correction [31]. Two methods have been proposed to scale trapped-ion platforms [32] beyond the limit of classical computations.

The first method is based on the Coulomb interaction between ions inside the same trapping potential. This phononic bus is used in small-scale quantum computers with ions in linear Paul traps. As the number of ions in the same trap potential is limited by certain physical effects, a quantum charge-coupled device divides the potential into several zones on a microfabricated chip [33], while these zones are interconnected by shuttling ions in between them. First proof-of-principle experiments have demonstrated individual features of this approach [34, 35], but a microchip trap which outperforms a single linear ion trap is still pending.

In the second method, a common technique in today's supercomputers is adopted. Just as classical computers are connected in clusters, nodes of small-scale quantum computers are interconnected via quantum communication to form a large-scale quantum processor [36–38]. In this architecture, trapped ions linked by the phononic bus act as stationary qubits, whereby photons acting as flying qubits connect spatially separated ion traps [39]. Consequently, light-matter interfaces between stationary and flying qubits are needed to transfer quantum information between different ion traps. For such a quantum interface, two different approaches are possible.

A probabilistic interface is based on collecting scattered photons from the ion. Even with a high numerical-aperture lens, only a small fraction of the emitted photons are accumulated [40], so that the efficiency is limited. In contrast, a deterministic interface enables the creation and absorption of photons with a near-unit efficiency [41]. A low-loss cavity offers an interaction between single ions and single photons [42, 43], so that a scalable quantum system is feasible [44]. Some fundamental quantum interface experiments were carried out in our research group [45–49], illustrating the deterministic interaction between ions and photons. However, the experimental apparatus used in these experiments is limited by the incoherent atomic decay.

In this thesis, an experimental setup is presented with the goal of enabling an ion-photon coupling strength dominating over all incoherent processes. Such a system would be the first step towards a highly efficient interface between ions and photons, which not only would enable a large-scale quantum computer but also efficient quantum repeaters for quantum networks. Furthermore, quantum simulations could be extended with a second interaction mediated by the cavity, and even quantum sensing is known to be enhanced by quantum networks [50–52]. Thus, linear ion traps coupled to cavities are suitable for applications of all four previously mentioned pillars: quantum sensing, communication, simulation and computation.

This thesis is structured as follows: The underlying processes of an optical cavity as a quantum interface between ions and photons are introduced in Chapter 2. Additionally, in this chapter, different technological implementations of cavities are discussed, motivating the approach of fiber-based optical cavities. Such fiber cavities are presented in Chapter 3, and their design, production and characterization is explained. Afterwards, in Chapter 4, the integration of a fiber cavity into our ion-trap system is discussed. Furthermore, independent measurements of both the ion trap and the fiber cavity are described. Next, a successful coupling between an ion and the fiber cavity is presented in Chapter 5. Unfortunately, this coupling did not work reproducibly and charges on the fibers were found to prevent us from further studies of our quantum interface. A method to characterize these charges is explained in Chapter 6. After that, in Chapter 7, measurements of a fiber cavity's finesse and TEM mode separations show evidence for the maximal expected coupling strength possible with our current fiber mirrors. Finally, Chapter 8 provides a summary of the knowledge gained in my PhD work and gives an outlook on how these insights have led to a new design for a linear ion trap, which provides robust protection for trapped ions against the influences of charges on fiber mirrors.

Chapter 2

Quantum interfaces based on optical cavities and ions

Our quantum interface, consisting of an ionized atom inside an optical cavity, is described by the theory of cavity quantum electrodynamics (CQED). This formalism defines the interaction between quantized matter, our ion, and the quantized electromagnetic field inside our cavity. Fundamental research is still continued in the area of CQED. For example, new regimes are still being entered, as recently the ultra-strong coupling regime was reached with superconducting circuits [53, 54]. Furthermore, known techniques are being adapted to new platforms, like the dispersive interaction in the optical domain [55]. However, CQED is also already established as a well-understood resource for quantum interfaces to build up quantum communication, as used in this thesis.

This chapter first introduces how a $^{40}Ca^{+}$ ion serves as a stationary qubit. Afterwards, the interaction of the ion with the light field of a cavity is described. Then, we compare different experimental setups with ions in cavities. In particular, we discuss the differences between two kinds of Fabry-Pérot cavities: "substrate cavities" built out of two highly reflective mirrors on super-polished glass substrates are compared with fiber-based Fabry-Pérot cavities, also called fiber cavities, whose mirrors are fabricated directly on the end facets of fibers. In the last section, the outstanding challenges for fiber cavities are explained, which provides an outlook to the possible advantages as a motivation for this thesis.

2.1 $^{40}Ca^{+}$ ions as stationary qubits

2.1.1 Basics of linear ion traps

In a linear ion trap, multiple ions can be stored as a string along one axis. Let us first consider one ion with one elementary charge e and mass M confined by an electrostatic field along this trap axis. In the "Innsbruck-style" linear ion trap of our research group, the electrostatic field is generated by two electrodes, called endcaps, with a distance d_{ax} to the ion. For ion positions $|x| \ll d_{\mathrm{ax}}$ from the trap center $x = 0$, the potential that the ion experiences can be approximated

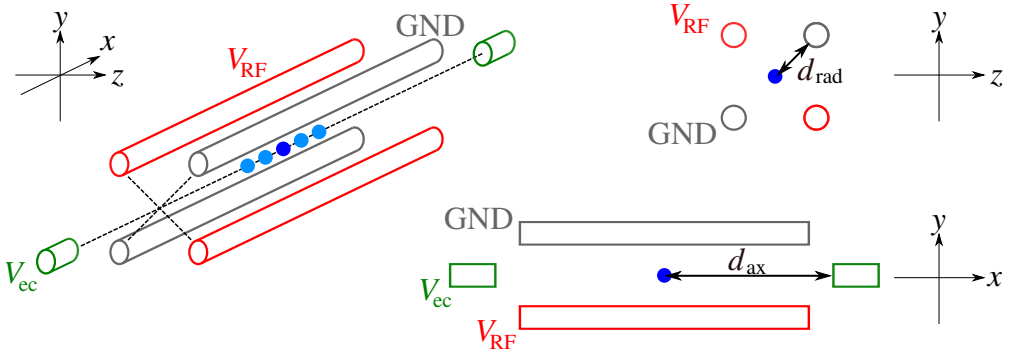

Figure 2.1: Schematics of a linear ion trap. The two red and two gray rods in a quadrupole configuration form the alternating field to trap ions in the radial yz plane. The two green endcaps provide confinement of the blue ions along the trap axis x.

as a harmonic trap potential [56]

$$\Phi_{\text{harm}}(x) = \frac{M}{2e}\omega_{\text{ax}}^2 x^2 = \frac{\alpha' V_{\text{ec}}}{d_{\text{ax}}^2} x^2, \tag{2.1}$$

with a DC voltage V_{ec} applied to the endcaps and a geometric factor α', that accounts for the shapes and locations of the electrodes. In this potential, the ion oscillates with an axial secular trap frequency

$$\omega_{\text{ax}} = \sqrt{\frac{2e\alpha' V_{\text{ec}}}{M d_{\text{ax}}^2}} = \sqrt{\alpha V_{\text{ec}}} \tag{2.2}$$

with the factor $\alpha = 2e\alpha'/(M d_{\text{ax}}^2)$.

The axial confinement causes an anti-confinement in at least one radial direction, as can be derived from the Laplace equation $\Delta\Phi = 0$. Our research group uses alternating electric fields in a quadrupole configuration as demonstrated by Paul *et al.* in 1958 [57], to circumvent this anti-confinement. (Other techniques to circumvent anti-confinement are possible, such as the Penning trap [58].) Four electrodes with length l are placed around the ion parallel to the trap axis with a distance d_{rad} between the ion and each electrode, as illustrated in Figure 2.1. In the original realization of such a Paul trap [57], two alternating RF voltages $\pm V_{\text{RF}}/2 \cos(\Omega_{\text{RF}} t)$ with frequency Ω_{RF} and two amplitudes $+V_{\text{RF}}/2$ and $-V_{\text{RF}}/2$ were applied to each pair of opposing electrodes. When $V_{\text{RF}} \cos(\Omega_{\text{RF}} t)$ is applied onto only one pair of electrodes, and the other pair is grounded, the residual RF field along the trap axis x can be neglected for $l, d_{\text{ax}} \gg d_{\text{rad}}$. Close to the trap center, the total trap potential, consisting of the electrostatic field and the RF field, can be approximated with the harmonic potential

$$\Phi(x,y,z,t) = \frac{\alpha' V_{\text{ec}}}{2 d_{\text{ax}}}\left(2x^2 - y^2 - z^2\right) + \frac{\eta' V_{\text{RF}}}{2 d_{\text{rad}}}\left(y^2 - z^2\right)\cos(\Omega_{\text{RF}} t) \tag{2.3}$$

with a factor η' that accounts for the radial trap geometry. The axial confinement is still described only by the previously discussed electrostatic potential of Equation (2.1). However, the radial potential depends on the time t. Note that the potentials along the two axes y and z

are equal except for a phase of π, so that in the following, only the solution for the y-axis is discussed, whereas the case of the z-axis could be solved equivalently. With the substitutions

$$a = -\frac{4e\alpha' V_{\mathrm{ec}}}{M\Omega_{\mathrm{RF}}^2 d_{\mathrm{ax}}^2} \text{ and } q = \frac{2e\eta' V_{\mathrm{RF}}}{M\Omega_{\mathrm{RF}}^2 d_{\mathrm{rad}}^2}, \tag{2.4}$$

the ion's motion along y can be described by the Mathieu equation [59, 60]. For stability parameters $(|a|, q^2) \ll 1$, stable solutions can be derived using the Floquet theorem, from which the approximate ion motion follows as

$$y(t) \propto \cos(\omega_{\mathrm{rad}} t)\left[1 - \frac{q}{2}\cos(\Omega_{\mathrm{RF}} t)\right] \tag{2.5}$$

with the secular radial trap frequency

$$\omega_{\mathrm{rad}} = \frac{\Omega_{\mathrm{RF}}}{2}\sqrt{\frac{q^2}{2} + a} = \sqrt{\omega_{\mathrm{RF}}^2 - \frac{\omega_{\mathrm{ax}}^2}{2}} \xrightarrow{\omega_{\mathrm{RF}} \gg \omega_{\mathrm{ax}}} \omega_{\mathrm{RF}} = \frac{eV_{\mathrm{RF}}\eta'}{\sqrt{2}\Omega_{\mathrm{RF}} d_{\mathrm{rad}}^2}. \tag{2.6}$$

The approximation of the total radial confinement ω_{rad} in Equation (2.6) holds for a weak axial anti-confinement compared to a strong radial RF confinement, $\omega_{\mathrm{ax}} \ll \omega_{\mathrm{RF}}$. This radial secular frequency describes the radial potential of the ion as a harmonic, time-independent pseudopotential.

The fast oscillation in Equation (2.5) follows the drive frequency Ω_{RF} of the RF fields. For small stability parameters q, as required for the solution, the corresponding amplitude of this motion is small with respect to the secular motion, and the motion is therefore called micromotion. The amplitude of this motion depends on the position of the ion in the RF field, so that in the center of the trap, where the quadrupole RF field is zero, the micromotion amplitude is minimal.

2.1.2 Ions as qubits

One basic unit of quantum information is a qubit, which is analogous to its classical counterpart, a digital bit [6]. Let us assume two quantum states $|S\rangle$ and $|D\rangle$. Here, we chose to label the states S and D rather than 0 and 1 because these labels correspond to the calcium states which form the qubit, as we will see later in this section. A qubit can be in a superposition of the two quantum states $|S\rangle$ and $|D\rangle$, which can be described as a vector

$$|\Psi\rangle = \alpha|S\rangle + \beta|D\rangle \tag{2.7}$$

by two complex numbers α and β, with $|\alpha|^2 + |\beta|^2 = 1$.

Similar to classical computer networks, quantum networks are incorporations of individual processing nodes. A quantum network allows individual stationary qubits to interact with each other via quantum channels, through which flying qubits are transmitted. In a quantum network, a stationary qubit of a single node needs to meet three requirements [17]. First, the stationary qubit needs to interact with flying qubits that transfer information throughout the network. This requirement is explained later in Section 2.2. Second, the qubit needs to function as a quantum memory to store quantum information longer than the propagation time through the network.

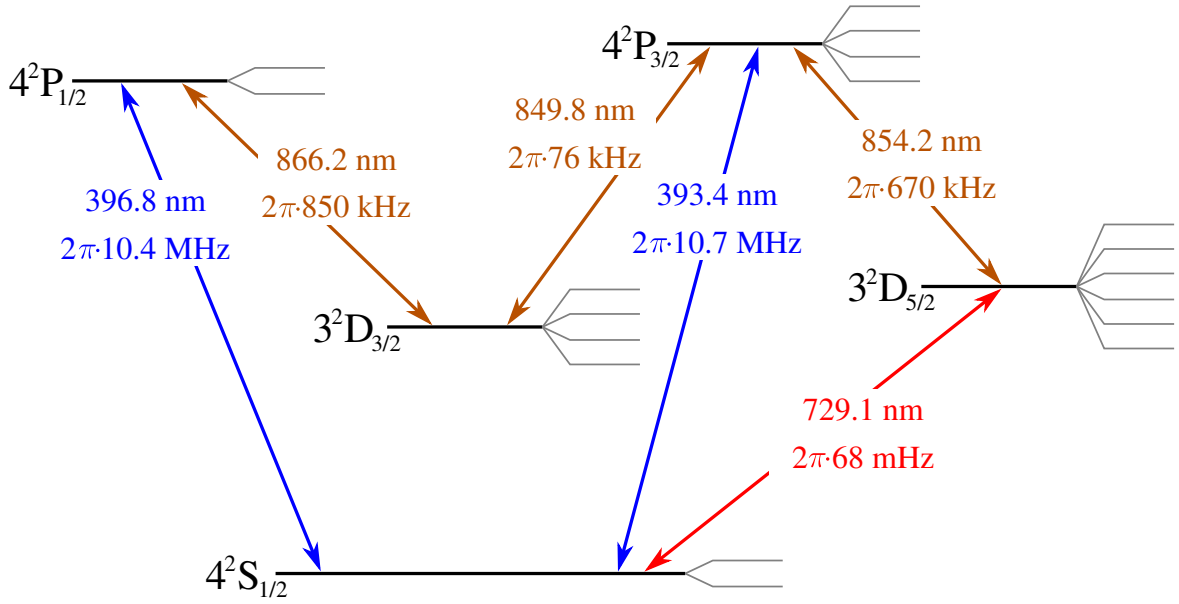

Figure 2.2: The energy-level scheme of $^{40}Ca^+$, with the 18 relevant states. Zeeman splittings generated by an external magnetic field are illustrated by the gray branches on the right side of each energy level. All relevant transitions are labeled with their wavelengths [62] and half width decay rate [63–66]. The $4^2S_{1/2}$, $4^2P_{1/2}$, and $3^2D_{3/2}$ energy levels on the left-hand side are used as a closed cycle for Doppler cooling and state readout. In contrast, the $4^2S_{1/2}$, $4^2P_{3/2}$, and $3^2D_{5/2}$ energy levels on the right-hand side are used for coherent manipulations. For example, an optical qubit can be defined between the ground state $4^2S_{1/2}$ and the metastable state $3^2D_{5/2}$, and the creation of single photons is carried out via a coherent Raman transition with a Λ-type level scheme from $4^2S_{1/2}$ to $3^2D_{5/2}$ via $4^2P_{3/2}$. Details on the Raman transition are given in Section 2.2.

Third, a node of quantum network requires the ability to process information. At least, the initialization, coherent manipulation and readout of the stationary qubit is required. The readout and further interaction of multiple qubits can be carried out by the transfer of quantum information to flying qubits, which then are measured or mediate the interaction with other local qubits [61]. However, deterministic multi-qubit gates within a single node could be beneficial and can improve the quantum communication between remote nodes [17]. With ions in linear traps, local and multi-qubit gate operations on stationary qubits are possible, as we now explain.

Different configurations of electronic states are able to function as stationary qubits. Let us consider the 18 relevant energy levels of the $^{40}Ca^+$ ion, as illustrated in Figure 2.2. The Zeeman substates are indicated as gray branches on the right side of each energy level, as they are split in energy by an external magnetic field. For $^{40}Ca^+$, there are two types of two-level systems that can serve as qubits.

Optical qubit

The first option is an optical qubit, which is defined between two energy levels connected by a weakly allowed transition in the optical regime. In our research group, one of the two Zeeman substates in the $4^2S_{1/2}$ manifold is chosen as the first state $|S\rangle$, and the second state $|D\rangle$ of the

qubit is selected from one of the six metastable Zeeman substates in the $3^2D_{5/2}$ manifold. The ion's state can be read out via illumination with 397 nm laser light. When the ion is in state $|S\rangle$, the laser excites the ion to the $4^2P_{1/2}$ manifold, and fluoresces when it subsequently decays back to $|S\rangle$. As there is also a decay channel to the $3^2D_{1/2}$ level, the population of $3^2D_{1/2}$ is repumped by an 866 nm laser field. In contrast, if the ion is in state $|D\rangle$, it remains dark, as the 397 nm laser light is not in resonance with any transition from the $3^2D_{5/2}$ manifold. It is possible to discriminate between a dark ion and a bright ion by capturing the ion's fluorescence by a photomultiplier tube (PMT) or a camera with a fidelity up to 99.99% within 145 µs [67]. The initialization of the qubit in a target Zeeman state is realized by well established techniques of optical pumping based on polarization or frequency selection [27].

For the coherent manipulation of the optical qubit, a laser beam with an electric field

$$\vec{E} = E_0 \cos(\omega_l t + \phi)\vec{e} \tag{2.8}$$

with amplitude E_0, frequency ω_l, phase ϕ, and polarization $\vec{e}$ is used. The interaction between the quantized two-level system and a classical electric field can be described by a semiclassical theory [60, 68]. Then, the interaction Hamiltonian is given by

$$\mathcal{H}_{\mathrm{int}} = \frac{1}{2}\hbar\Omega \left[|S\rangle\langle D| \, e^{i(\Delta t-\phi)} + |D\rangle\langle S| \, e^{-i(\Delta t-\phi)} \right] \tag{2.9}$$

with Rabi frequency Ω and detuning $\Delta = \omega_{\mathrm{SD}} - \omega_{\mathrm{l}}$ between the frequencies of the S–D transition ω_{SD} and the laser ω_{l}. When $\Delta = 0$, the unitary operation

$$U(t,\phi) = \begin{pmatrix} \cos(\Omega t) & -ie^{-\phi}\sin(\Omega t) \\ -ie^{-\phi}\sin(\Omega t) & \cos(\Omega t) \end{pmatrix} \tag{2.10}$$

is implemented by the laser field and coherently applied to the qubit. The population of the state $|S\rangle$ is thus transferred into the state $|D\rangle$ and vice versa, while the phase ϕ of the laser can be set to manipulate the phase of the qubit. With an initial state $|S\rangle$ at time $t = 0$ and detuning Δ, the population of the state $|D\rangle$ evolves as

$$p_{\mathrm{D}}(t) = \frac{\Omega^2}{\Omega^2+\Delta^2}\sin\left(\frac{1}{2}\sqrt{\Omega^2+\Delta^2}\cdot t\right) \xrightarrow{\Delta=0} p_{\mathrm{D}}(t) = \sin\left(\frac{1}{2}\Omega t\right). \tag{2.11}$$

With the passing of time, the population is exchanged between the two qubit states. These exchanges are known as Rabi oscillations.

For the special case of $\Delta \gg \Omega$, population transfer between the states is suppressed, but each energy level is shifted by an amount

$$\Delta E = \frac{\hbar\Omega^2}{4\Delta}, \tag{2.12}$$

which is known as the AC-Stark shift. For $\Delta < 0$, the laser light is red-detuned with respect to the ion's transition, and both the energy levels are pushed apart. For a blue-detuned laser ($\Delta > 0$), both energy levels are pushed closer.

With multiple ions in the trap, individual ions of the string can be manipulated by focusing the laser light field onto single ions. Furthermore, multiple-qubit operations can be carried out

by addressing common vibrational modes of the ions inside the trap [26, 69]. A combination of all these techniques enables a universal set of gates for the realization of a quantum information processor based on ions in a linear ion trap [70].

Note that the lifetime of the qubit state in the $3^2D_{5/2}$ manifold is 1.165 s [64], so that the decay of the upper qubit state takes orders of magnitude longer than usual gate times of tens of microseconds [70]. Additionally, dephasing of the qubit can occur due to fluctuations of the magnetic field and laser frequency [70]. These decoherence effects can be minimized, — in other words, the coherence times can be increased — by using a decoherence free subspace [71, 72], quantum error correction [31], or other qubit encodings, as introduced below.

Spin qubit

The second possible qubit implementation is a spin qubit encoded in two substates in the same Zeeman manifold, and therefore only separated in energy by the Zeeman splitting, which is defined by the applied magnetic field. In our research group, spin qubits are often used as temporary qubit states. For example, by using two substates in the $3^2D_{5/2}$ manifold, the quantum information stored in the ion is preserved while another ion is read out selectively [73]. Another application of such a spin state is as the initial state for a state transfer from the ion to a single photon, as reported in [47]. The underlying mechanism of this light-matter quantum interaction will be explained in the next section. Furthermore, encoding the qubit in the Zeeman substates of the $4^2S_{1/2}$ level of $^{40}Ca^+$, Ruster *et al.* showed a coherence time exceeding the lifetime of the optical qubit [74].

In principle, a third option is possible: the hyperfine electronic states could be used to encode a qubit. For that, an isotope with nuclear spin is required, such as $^{43}Ca^+$. This encoding opens up the possibility for long coherence times, as reported in [30], in which a qubit encoded in a $^{171}Yb^+$ ion was stored for ten minutes.

Besides these electronic qubits, the motional states of the ion in the trap can be used for a qubit [75]. Such a qubit encoding opens up possibilities for continuous-variable quantum information and hybrid schemes with both discrete qubits and continuous variables [76].

2.1.3 Ion cooling

Our quantum interface is based on the coupling between single ions and the standing wave of an optical resonator with a wavelength $\lambda \sim 800$ nm. A precise localization of the ion Δx in an antinode of the optical resonator, $\Delta x \ll \lambda/2$, is essential to achieve the maximal coupling strength between the light field and the ion. Therefore, the ion needs to be cooled, that is, the amplitude of its secular motion needs to be minimized. In our research group, trapped ions are usually cooled by two techniques.

First, the ion is illuminated by a 397 nm laser beam, which is red-detuned from the dipole transition between the ground state $4^2S_{1/2}$ and the excited state $4^2P_{1/2}$. The transition between these states has a half-width decay rate of $\gamma = 2\pi \cdot 10.4$ MHz: see Figure 2.2. The absorption of a red-detuned photon decelerates the ion opposite to the direction of the laser beam. In the following, the ion emits a photon in an arbitrary direction in $\tau = 1/(2\gamma)$, and the ion absorbs the next photon. The momentum gained by the emission of photons averages out due to the different directions, but the absorption of photons cools the ion in the direction of the laser

beam. As the electron decays with a probability of 8% from the $4^2P_{1/2}$ state to the $3^2D_{3/2}$ state, the population of the metastable $3^2D_{3/2}$ state needs to be repumped by an $866\ \mathrm{nm}$ laser to close the cooling cycle. Using appropriate detunings and amplitudes of these two cooling lasers and a suitable external magnetic field (typically $\sim 0.3\ \mathrm{mT}$ in our experiments), Doppler cooling can be achieved down to its limit [77, 78]. The limit is given by the minimum mean phonon number

$$\bar{n}_{\mathrm{Dop},i} = \frac{\gamma}{\omega_{\mathrm{i}}} \tag{2.13}$$

in the ion's quantized trap potential with a secular frequency ω_{i} in each direction $i \in \{x, y, z\}$. Then, the spatial extent of the ion's wave packet is

$$\Delta x_i = x_0 \sqrt{2\bar{n}_{\mathrm{Dop},i} + 1} \tag{2.14}$$

with the spatial extent of the ground state $x_0 = \sqrt{\hbar/(2M\omega_i)}$. For typical secular frequencies of $\omega_i \sim 1$–$3\ \mathrm{MHz}$, the spatial extent is $\Delta x_i \sim 20$–$50\ \mathrm{nm}$ for a Doppler-cooled ion in our trap.

Therefore, a second technique is necessary to cool the ion further, close to its ground state, in order to achieve a spatial extent $\Delta x \ll \lambda/2$. With the narrow linewidth of the qubit transition ($S_{1/2}$–$D_{5/2}$ for $^{40}Ca^{+}$), the red motional sideband of the ion can be addressed, and the ion can be excited to the $D_{5/2}$ manifold with a narrow laser, while the ion's motion is reduced by one phonon. Via the $P_{3/2}$ level, the ion is than repumped by an $854\ \mathrm{nm}$ laser beam back to the ground state $S_{1/2}$. This cooling cycle is then repeated until the ground state of the ion's motion is reached [79, 80]. A coherent excitation of the red motional sideband is only possible, in other words, the sidebands are resolved, when the ion is in the Lamb-Dicke regime, $\eta^2(2\bar{n} + 1) \ll 1$ with $\eta = 2\pi x_o/\lambda$. For $^{40}Ca^{+}$, secular trap frequencies $\omega \geq 1\ \mathrm{MHz}$ are required to reach the Lamb-Dicke regime and to enable this sideband cooling technique of previously Doppler-cooled ions [60]. As this requirement was not fulfilled in our system, and other problems kept us back from further progress, (Section 5.1), only Doppler cooling was implemented in our system.

2.2 Interaction between ions and photons inside cavities

In this section, the interaction between an atom and the light field of an optical cavity will be introduced. The underlying physics is described in the theory of cavity quantum electrodynamics (CQED). Detailed theoretical descriptions of calcium ions in an optical cavity can be found in several PhD theses of our research group [81, 43, 82–84]. Here, we only present the basics of this interaction to explain the calculations for discussions of different cavity configurations (Section 2.3). We start with the simple model of a two-level atomic system coupled to a cavity mode. This model is then extended to an interaction of the cavity mode with a three-level atomic system. Finally, a physical implementation of quantum information transfer between light and matter is described.

2.2.1 Simplified model of ion-photon coupling inside a cavity

The simplest theoretical model describing the coupling of an atom to a cavity is the interaction between an atom simplified to a two-level system and one electromagnetic field mode of an optical resonator. This model is known as the Jaynes-Cummings model [85]. We label the lower state of the systems as the state $|D\rangle$ and the higher level as the state $|P\rangle$, which are separated by the energy $\hbar\omega_{\mathrm{DP}}$. Again, this labeling is consistent with the used levels in $^{40}\mathrm{Ca}^{+}$. Single photons of the quantized light field with a frequency ω_c are described by states in the number basis (Fock states): $|n\rangle$ with $n \in \mathbb{N}$. The number of photons n is changed by the creation and annihilation operators $a^\dagger$ and a.

Then, the Hamiltonian $\mathcal{H}$ describing the Jaynes-Cummings model can be divided into three parts:

$$\mathcal{H} = \frac{1}{2}\hbar\omega_{\mathrm{DP}}(\,|S\rangle\langle S| + |D\rangle\langle D|\,) \qquad \text{- atom} \tag{2.15}$$

$$+ \hbar\omega_c(\hat{a}^\dagger + \hat{a}) \qquad \text{- cavity} \tag{2.16}$$

$$+ \hbar g_0\left(|D\rangle\langle S|\,\hat{a} + |S\rangle\langle D|\,\hat{a}^\dagger\right) \qquad \text{- interaction} \tag{2.17}$$

The interaction between light and matter

$$\hbar g_0 = -\vec{\mu}_{\mathrm{DP}} \cdot \vec{E} \tag{2.18}$$

is then given by the scalar product of the atomic dipole moment $\vec{\mu}_{\mathrm{DP}}$ and the electric field vector $\vec{E}$ of the cavity light field.

The coupled system is in the ground state $|D,0\rangle = |D\rangle \otimes |0\rangle$, when both subsystems are in their ground states: the atom is in $|D\rangle$, and no photon is in the cavity: $|0\rangle$. With one excitation in the system, nontrivial eigenstates can be found. In the resonant case, where $\omega_{\mathrm{DP}} = \omega_c$, these states are known as dressed states $|1,\pm\rangle = \sqrt{1/2}\,(\,|D,1\rangle \pm |P,0\rangle)$, and their energy splitting is $2g_0$ [86]. This so-called vacuum-Rabi splitting indicates that the excitation oscillates with the rate $2g_0$ between the atom and the cavity, similar to the Rabi oscillation of the qubit between the classical light field and the quantized two-level system in Subsection 2.1.2.

The Jaynes-Cummings model needs to be extended, as two significant loss mechanisms for an optical cavity have to be considered [87]. First, the atom decays with a rate 2γ from the excited state, which in the case of $^{40}\mathrm{Ca}^{+}$ is non-negligible. Second, both transmission through

the cavity mirrors and scattering and absorption losses in the cavity mirrors contribute to the decay rate 2κ of the cavity. The coherent atom-photon coupling rate g_0 is now in competition with these two dissipative parameters γ and κ.

This competition can be expressed as the ratio between the coherent coupling rate g_0 and the dissipative decay rates γ and κ, which is known as the cooperativity

$$C = \frac{g_0^2}{2\kappa\gamma}. \tag{2.19}$$

The atom-photon coupling rate g_0, defined in Equation (2.18), can be expressed as

$$g_0 = \sqrt{\frac{3c\gamma_{\mathrm{PD}}\lambda^2}{\pi^2 L w_0^2}}. \tag{2.20}$$

In this notation, the transition between the two atomic levels has a decay rate of $\gamma_{\mathrm{PD}} = \gamma$ and a wavelength $\lambda = 2\pi c/\omega_c$, with c the speed of light. Furthermore, the cavity has a length L and waist w_0, at which the atom is located. Then, the cooperativity can be rewritten as

$$C = \frac{3\lambda^2\mathcal{F}}{\pi^3 w_0^2} \tag{2.21}$$

with $\mathcal{F} = \pi c/(2L\kappa)$ the finesse of the cavity. The finesse describes the quality of the cavity mirrors, and can be rewritten as $\mathcal{F} = 2\pi/\mathcal{L}_{\mathrm{tot}}$, with the total losses $\mathcal{L}_{\mathrm{tot}}$ of both mirrors.

2.2.2 Extension to a three-level system

For quantum state transfer and entanglement distribution among distant nodes, Cirac *et al.* proposed a three-level atomic system coupled to a cavity [88]. Thus, a second lower state $|S\rangle$ is introduced. The two lower states $|S\rangle$ and $|D\rangle$ form a Λ-type three-level system with the upper state $|P\rangle$, which is connected via a electric dipole transition to each lower state, $|S\rangle$ and $|D\rangle$. By driving both transitions with lasers, each of which has the same detuning Δ from the excited state, one can directly transfer the population of one ground state to the other. This direct transfer without the excitation of the bright state $|P\rangle$ is known as a Raman transition [89]. If the laser field between $|P\rangle$ and $|D\rangle$ is replaced by a cavity field, a photon is created inside the cavity while the electron is transferred from $|S\rangle$ to $|D\rangle$. As the cavity light field decays with a rate 2κ, the photon leaves the cavity. Then the remaining state $|D\rangle$ does not interact further with the laser field, and only one photon is created. This process is called a vacuum-stimulated Raman transition [90]. When the respective detunings of the cavity and the laser from $|P\rangle$, Δ_{C} and Δ_{L}, are equal to one another, $\Delta = \Delta_{\mathrm{C}} = \Delta_{\mathrm{L}}$, and when Δ is sufficiently large with respect to the excited state linewidth γ_{P}, $\Delta \gg \gamma_{\mathrm{P}}$, the three-level system can be described by an effective two-level system with an effective Rabi frequency

$$\Omega_{\mathrm{eff}} = \frac{g\Omega_{\mathrm{L}}}{2\Delta} \tag{2.22}$$

between $|S\rangle$ and $|D\rangle$. This Rabi frequency Ω_{eff}, that is, the transition rate between $|S\rangle$ and $|D\rangle$, can be increased by increasing the Rabi frequency Ω_{L} of the laser or by decreasing the

detuning Δ. However, when the effective Rabi frequency is increased, the effective decay rate

$$\gamma_{\text{eff}} = \left(\frac{\Omega_{\text{L}}}{2\Delta}\right)^2 \gamma_{\text{P}} \tag{2.23}$$

needs to be considered. Here, γ_{P} is the decay rate from $|P\rangle$ via all possible decay channels into both lower states. Note that a calculation of the effective cooperativity for this three-level system

$$C_{\text{eff}} = \frac{\Omega_{\text{eff}}^2}{2\kappa\gamma_{\text{eff}}} = \frac{g^2}{2\kappa\gamma_{\text{P}}} = C \tag{2.24}$$

yields the same cooperativity as for the two-level system, except that now all possible decay channels of the excited state $|P\rangle$ must be considered. Again, the cooperativity can be rewritten as

$$C = \frac{3\lambda^2\mathcal{F}}{\pi^3 w_0^2}\frac{\gamma_{\text{DP}}}{\gamma_{\text{P}}}, \tag{2.25}$$

with the additional ratio between the decay rate γ_{DP} of the cavity transition and the decay rate $\gamma_{\text{P}} = \gamma_{\text{SP}} + \gamma_{\text{DP}}$ from $|P\rangle$ via both decay channels to $|S\rangle$ and $|D\rangle$. Note that this formula can also be extended to consider more decay channels to additional states, such as Zeeman substates.

2.2.3 Physical implementation

As explained in Chapter 1, quantum networks are able to improve all four disciplines: quantum computing, simulation, sensing and communication. In quantum networks, the fundamental building block is an interface between stationary qubits and flying qubits, which are then transmitted to other remote stationary qubits [18]. The vacuum-stimulated Raman transition presented in the previous section provides the basis to realize this interaction between flying and stationary qubits in three ways. The first option is the creation of flying qubits which are entangled with the stationary qubits. In the second method, a quantum state is transferred from a stationary to a flying qubit. The reversed process, state transfer from a flying to a stationary qubit, is the third option.

In our research group, the first and second methods have been realized in experiments with photons as flying qubits and $^{40}Ca^{+}$ ions as stationary qubits, as suggested in [91]. In both cases, two Λ-type three-level systems consist of states in the excited-state manifold $4^2P_{3/2}$, the ground-state manifold $4^2S_{1/2}$, and the metastable-state manifold $3^2D_{5/2}$. A high-finesse cavity is coupled to the transitions between $3^2D_{5/2}$ and $4^2P_{3/2}$, while the transitions between $4^2S_{1/2}$ and $4^2P_{3/2}$ are driven by lasers. In the first experiment, a photon was created whose polarization state was entangled with the electronic state of a trapped ion [82]. In the second experiment, a qubit encoded in the ground state of the trapped ion was transferred to the polarization state of a photon [47].

For both experiments, the Raman transition with the creation of a photon was the fundamental process of both entanglement creation and state transfer. The performance of this transition is determined by the maximal success probability [92]

$$P_{\text{s}} = \frac{2C}{2C+1} \tag{2.26}$$

to create a photon inside the cavity. This probability is equal to the probability of the reversed process, the absorption of photon inside the cavity of a CQED system [93]. Moreover, Goto *et al.* derived a lower bound on the failure probability

$$P_{\mathrm{F}} \geq \frac{2}{1+\sqrt{1+2C_{\mathrm{in}}}} \approx \sqrt{\frac{2}{C_{\mathrm{in}}}} \tag{2.27}$$

to generate a single photon in the desired optical mode outside the cavity. Therefore, they have introduced the *internal cooperativity* $C_{\mathrm{in}} = g^2/(2\kappa_{\mathrm{in}}\gamma)$, with the internal cavity decay rate κ_{in} given only by losses that do not contribute to the transmission into the desired output mode. To achieve this lower bound of failure probability, the losses of the cavity need to be known precisely and the transmission of the mirrors need to be optimized. As this optimization was not carried out for most of the presented cavities, we focus onto the cooperativity C in this thesis. This cooperativity is still a important figure of merit for CQED experiments, and also indicates the efficiency of an interface based on the coupling between cavities and atoms [94].

2.3 Comparison of different experimental setups

As optical cavities are promising candidates to extent the physical opportunities of trapped ions, several research groups are investigating such systems. In this section, first, an overview of different experimental setups is presented. Here, two technologies are used: conventional "substrate" cavities built with two mirrors on glass substrates and, fiber-based cavities. In the second subsection, these two technologies are compared in more detail.

2.3.1 Overview of experiments

The first CQED setups with trapped ions were built in the group of H. Walther [95] and in our research group [96]. By modifying the cavity geometry and the cavity transition, experiments in both groups [97] and [43] showed the deterministic generation of photons. In the same year, Leibrandt *et al.* demonstrated cavity sideband cooling of trapped ions [98]. Later in V. Vuletić's and of C. Monroe's groups, CQED setups with trapped ions were also built ([99] and [100], respectively). Recently, a CQED project was started by B. Lanyon here in Innsbruck [101]. A broader history of CQED can be found in review articles such as [102, 103, 39, 104]. Konstantin Friebe has recently summarized in particular CQED experiments in Innsbruck in his PhD thesis [84].

All cavity configurations discussed in this section are based on highly reflective mirrors which were coated onto super-polished glass substrates. In the following, these cavities are called "substrate" cavities, and their parameters are listed in first part of Table 2.1. For each configuration of these substrate cavities, we used Equation (2.20) to calculate the ion-photon coupling strength g_0. Although the experiments referenced above used different ion species and coupled transitions, here all coupling rates are calculated for the transition from $3^2D_{5/2}$ to $4^2P_{3/2}$ of $^{40}Ca^+$ to make a direct comparison of the cavity geometries possible. The geometry of a cavity consisting of two mirrors with radius of curvature R can be defined by the two parameters: the cavity length L and the dimensionless parameter $g = 1 - L/R$. The coupling strength given in Equation (2.20) can be rearranged as a function of these parameters:

$$g_0 = \sqrt{\frac{6c\gamma_{\mathrm{PD}}}{\pi}}\frac{1}{L}\left(\frac{1-g}{1+g}\right)^{1/4}. \tag{2.28}$$

For a certain cavity length L, the g-parameter describes the stable configurations of the cavity, ranging from $g = -1$ to $g = 1$. For g approaching 1 ($R \gg L$), the mirrors behave like two plane mirrors at a distance L. This configuration is known as the plane-parallel limit. In this limit, the cavity waist is defocused, and the coupling strength approaches zero. A second regime is the confocal regime, where $g = 0$, for which the radius of curvature of the mirrors R is equal to the cavity length L. Most interesting for our purposes is the concentric regime, where $g \to -1 (L \to 2R)$. Here, the coupling strength is increased by the focused cavity waist. A two-dimensional landscape of the coupling strength g_0, depending on L and g, is plotted in Figure 2.3. Note that the y-axis has two different scales to illustrate the enhancement of the coupling strength in the concentric limit. The calculated values of the experiments considered here are indicated as crosses in this figure. Compared to other experiments with substrate cavities, the experiments [43] and [101] have the highest coupling strength $g_0 \approx 2\pi \cdot 1.5\ \mathrm{MHz}$, because they are closer to the concentric limit despite the relatively long cavity $L \approx 20\ \mathrm{mm}$. Note that

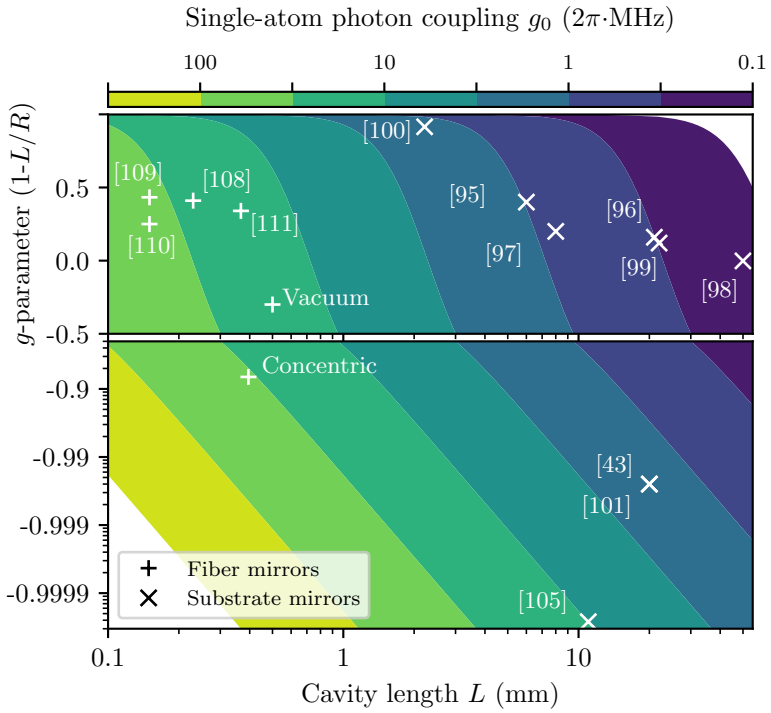

Figure 2.3: Calculated ion-photon coupling strength g_0 depending on the cavity length L and the parameter $g = 1 - L/R$. The calculations of all experiments are carried out for the transition D–P of $^{40}Ca^{+}$. Experimental setups with cavities based on two mirrors on glass substrates are indicated as crosses. Note that [105] was actually developed for a neutral-atom experiment. Fiber cavity setups with trapped ions are shown as pluses. The fiber cavities evaluated within this work are indicated as "Vacuum" and "Concentric", and are presented in Subsection 4.5.1 and Chapter 7, respectively.

for these two substrate cavities, the atomic decay rate $\gamma_\mathrm{P} = 2\pi \cdot 11.4\ \mathrm{MHz}$ is dominant over the coupling rate. However, with high-finesse substrate cavities, a cavity decay $\kappa < 100\ \mathrm{kHz}$ can be achieved so that a cooperativity $C > 1$ is feasible in the concentric regime.

Recently, an interesting limit was reached in a setup developed for neutral-atom experiments. Nguyen *et al.* operated a near-concentric cavity at the last stable resonance [105]. That means the cavity was only $207\ \mathrm{nm}$ shorter than the critical concentric point at a cavity length $L = 2R$, so that the next resonance would be beyond the stable geometry $g < -1$. For the $11\ \mathrm{mm}$-long cavity in this experiment, a coupling strength $g_0 \approx 2\pi \cdot 10\ \mathrm{MHz}$ is expected for $^{40}Ca^{+}$, which would be on the order of the atomic decay rate, $g_0 \sim \gamma_\mathrm{P}$. A further discussion of how this extreme cavity configuration behaves with respect to the other experimental setups is presented in the next subsection.

To achieve a coupling strength larger than the atomic decay rate, $g_0 > \gamma_\mathrm{P}$, a new mirror technology was adopted from experiments with neutral atoms. Fiber-based Fabry-Pérot cavities [106, 107], which are based on mirrors on the end facets of fibers, can be placed closer than substrate mirrors to a trapped ion. The size of these fiber cavities is characterized by the cladding diameter of the fiber with a few hundreds of micrometers. In contrast, the glass of substrate

mirrors has usually a diameter of couple of millimeters that makes the implementation into an ion trap challenging. At the same time, fiber cavities also offer small mirror radii of curvature, so that the g-parameter can be small even for sub-millimeter cavity lengths, and a high ion-photon coupling strength can be achieved. Three different experimental setups [108], [109], and [110], in M. Köhl's group have been used to demonstrate coupling between a single trapped ytterbium ion and a fiber cavity. Furthermore, in M. Keller's group, Takahashi *et al.* [111] achieved the coupling between a fiber cavity and a trapped calcium ion. In Figure 2.3, these fiber-cavity configurations are all located at a coupling strength $g_0 > 20$ MHz, which exceeds the atomic decay rate γ_{P}. However, the challenging part is now to find a trade-off between the cavity decay rate κ and the ion-mirror distance d. On the one hand, a small distance d between the trapped ion and the dielectric surface of a fiber mirror makes it challenging to trap ions without serious disturbance to the ion's potential. This is even true when the dielectric fibers are shielded by electrodes, as the electric field noise of electrodes scales polynomially [112]. On the other hand, the cavity decay rate $\kappa = \pi c/(2L\mathcal{F}) = c/(4L\mathcal{L}_{\mathrm{tot}})$ could exceed the coupling strength for large $d = L/2$ because the fiber mirrors introduce additional losses for long cavities, as later discussed.

Further attempts to implement a fiber cavity into an ion trap were carried out in F. Schmidt-Kaler's group [113]. Recently, in J. Home's research group, the development of a fiber cavity experiment was started [114]. In the scope of an ongoing collaboration between our research groups, we provided them with some fiber mirrors which were produced and measured during my PhD work (Chapter 7).

Table 2.1: Cavity configurations of past ion-cavity experiments. Values with asterisk were not found in the references and were calculated from given parameters. Note that each waist is defined by the wavelength used in the corresponding experiment, and could differ from the waist used for the calculation in Figure 2.3

Ref.	Group	Length	radius of curvature	Transition	Waist	Finesse
x[95]	Walther	6 mm	10 mm	Ca-397 nm	24 µm	3,000
x[96]	Blatt	21 mm	25 mm	Ca-729 nm	54 µm	35,000
x[42, 97]	Walther	8 mm	10 mm	Ca-866 nm	37 µm*	49,000*
x[43, 45]	Blatt	19.98 mm	10 mm	Ca-866 nm	13 µm	70,000
x[98]	Chuang	50 mm	50 mm*	Sr-422 nm	57.9 µm	25,600
x[99]	Vuletić	22 mm	25 mm*	Yb-369 nm	38 µm	12,500
x[100]	Monroe	2.126 mm	25 mm	Yb-369 nm	25 µm*	3790→1490
x[101]	Blatt	19.90 mm	9.98 mm	Ca-866 nm	12.3 µm	54,000
+[105]	Kurtsiefer	11 mm	5.5 mm	Rb-780 nm	2.4 µm	603
+[108]	Köhl	230 µm	390 µm*	Yb-935 nm	7 µm	1000
+[109]	Köhl	150 µm*	300 µm	Yb-935 nm	6.1 µm	20000
+[110]	Köhl	150 µm*	200 µm	Yb-935 nm	3.1 µm	1140→207
+[111]	Keller	367 µm	560 µm	Ca-866 nm	8.5 µm	48,000

2.3.2 Substrate cavities versus fiber cavities

As discussed in Subsection 2.2.3, the cooperativity is an important figure of merit for a light-matter quantum interface, which we aim to implement in our experiments [91]. A high cooperativity can be achieved by either a high finesse $\mathcal{F}$ or a small waist w_0: see Equation (2.21). The finesse $\mathcal{F} = 2\pi/(\mathcal{L}+\mathcal{T})$ is determined by the cavity losses $\mathcal{L}$ and by the chosen transmission $\mathcal{T}$ of the highly reflective mirrors. Consequently, for a given mirror coating, only the waist w_0 can be minimized to increase the cooperativity further. In the following, we consider a symmetric cavity, consisting of two mirrors with the same radius of curvature R.

For a given cavity length L, the waist

$$w_0 = \sqrt{\frac{L\lambda}{2\pi}\sqrt{\frac{1+g}{1-g}}} = \sqrt{\frac{\lambda}{2\pi}\sqrt{2RL-L^2}} \tag{2.29}$$

is minimized by approaching the concentric regime with $g \to -1$ ($L \to 2R$). This optimization leads to the increase of the ion-photon coupling strength g_0, as shown in Figure 2.3. At the same time, while approaching the concentric regime, the spot size of the light field at the mirrors is enlarged. When the diameter of the light field is larger than the mirror diameter, the cavity mode is clipped and additional losses are introduced, or in other words, the finesse is decreased. For fiber cavities, such clipping losses are common, and a model has been introduced to approximate the losses [107]. The surface of fiber mirrors is not spherical over the entire fiber tip, so that an effective useful diameter D can be determined for which clipping losses

$$\mathcal{L}_{\text{clip}} = e^{-\frac{D^2}{2w^2}} \tag{2.30}$$

are found, with a diameter $2w$ of the cavity mode at the fiber mirror. Hereby, the amplitude of the electric field inside the cavity drops at a radius w to $1/e$ of the maximum value.

Note that this cavity mode radius

$$w = \sqrt{\frac{L\lambda}{\pi}\sqrt{\frac{1}{1-g^2}}} = \sqrt{\frac{\lambda RL}{\pi}\sqrt{\frac{1}{2RL-L^2}}} = \sqrt{\frac{RL}{2}}\frac{\lambda}{\pi w_0} \tag{2.31}$$

at a mirror also depends on the cavity length L. For a given set of mirrors with a radius of curvature R, losses $\mathcal{L}$, transmission $\mathcal{T}$, and an effective useful diameter D, the cooperativity can be calculated as a function of the cavity length L:

$$C(L) = \frac{6\lambda^2\gamma_{\text{DP}}}{\pi^2\gamma_{\text{P}}}\frac{1}{w_0^2(L)\left(\mathcal{L}+\mathcal{T}+e^{-\frac{D^2\pi^2}{\lambda RLw^2(L)}}\right)}. \tag{2.32}$$

In general, an analytical solution to find extrema of $C(L)$ is not possible without further assumptions or simplifications. However, the maximal cooperativity $C_{\max}$ in the concentric regime could be determined numerically by selecting the maximal value of calculated values $C(L)$ for $L > R$. The corresponding g-parameter $g_{\max}$ is calculated for the length $L_{\max}$ at $C_{\max}$. These two values are determined for three different sets of mirrors: the two setups with substrate mirrors of [45] and [105], and the fiber cavity presented in Chapter 7.

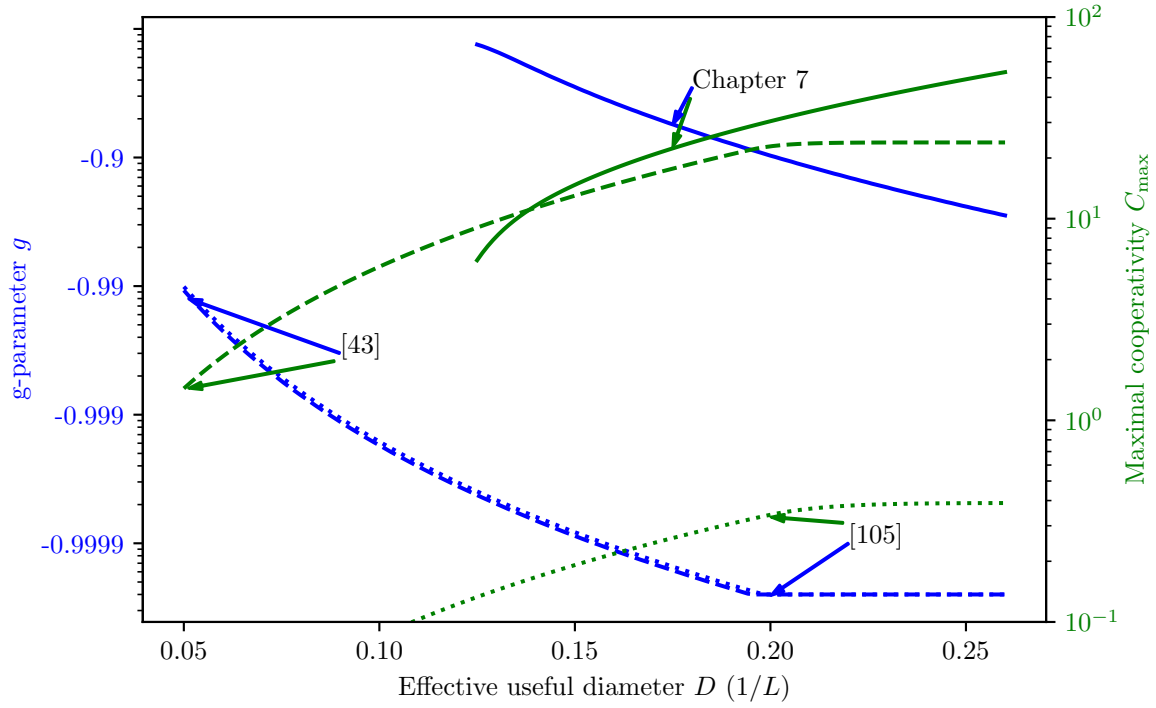

Figure 2.4: Maximal achievable cooperativity as a function of effective useful diameter (green lines). The corresponding g-parameters of the cavity configuration are plotted as orange lines. Both parameters are determined for the three sets of mirrors: [45], [105] and the fiber mirrors presented in 7.

In Figure 2.4, the maximal achievable cooperativities $C_{\max}$ (green lines) are plotted as a function of the effective useful diameter D, normalized to the cavity length L. In the same figure, the corresponding g-parameters are plotted as orange lines. The larger the radius of curvature the smaller the normalized effective useful diameter D/L needs to be to approach the concentric regime. At the same time, the higher the finesse of a cavity the larger the effective useful diameter D needs to be. The two substrate cavities, [43] with $R = 10\,\mathrm{mm}$ and [105] with $R = 5.5\,\mathrm{mm}$, have almost identical values of the g-parameter, as the differences in radius of curvature and finesse cancel each other out. However, the maximal achievable cooperativities of [105] are almost two orders of magnitudes smaller than [43] due to the different finesses of the two cavities ($\mathcal{F} = 70\,000$ for [43] compared to $\mathcal{F} = 603$ for [105]). As [105] is at the last stable mode, an improved effective useful diameter D would not increase the maximal cooperativity anymore. The only way to improve the cooperativity further is a higher finesse. For example, with a finesse of 70,000 as [43], a cooperativity $C > 10$ is feasible by approaching the concentric regime, see dashed green line in Figure 2.4.

With such a substrate cavity configuration, there are still two further issues possible besides the challenging alignment without any losses. First, the spacing of TEM modes decreases in the frequency domain by approaching the concentric regime [105]. That means, an unwanted coupling of TEM modes is enhanced by increasing the cooperativity. Second, with a higher finesse, the cavity decay rate κ is decreased, so that generated photons take more time to leave

or enter the cavity. In particular, quantum communication on short scales, such as used for distributed quantum communications, could be limited by the long cavity decay time.

With our fiber cavity, labeled as "Chapter 7" in Figure 2.4, we achieve a calculated ratio $D/L \approx 0.18 \mathrel{\widehat{=}} 70\ \mu\mathrm{m}$, similar to $D/L \approx 0.2 \mathrel{\widehat{=}} 1.1\ \mathrm{mm}$ of [105]. However, the high finesse $\mathcal{F} = 100\,000$ of the fiber cavity enables an expected achievable cooperativity of $C = 20$, compared to $C = 0.4$ for [105]. An improvement of our fiber cavity's cooperativity up to $C \approx 40$ with an effective useful diameter $D \approx 100\ \mu\mathrm{m} \mathrel{\widehat{=}} D/L \approx 0.25$ is within reach [115], see solid green line in Figure 2.4. In contrast, the maximal cooperativity of substrate cavities in the concentric regime is limited to $C < 10$ with the two further limitations as discussed previously.

These different maximal cooperativities for the three sets of mirrors result from the different value of the radius of curvature R. Mirrors of substrate cavities, such as used in [45], are limited to $R \geq 10\ \mathrm{mm}$ due to their super-polish fabrication. In contrast, the fabrication techniques for fiber cavities, as described in Chapter 3, enable the production of high-finesse mirrors over the range $5\ \mu\mathrm{m} < R < 2\ \mathrm{mm}$. These small radii of curvature opens up short fiber cavities and therefore fast quantum communication in the concentric regime.

2.4 Outstanding challenges of trapped ions coupled to fiber cavities

Following the same approach used in designing substrate cavities for trapped-ion experiments, it would be possible to increase the coupling between trapped ions and fiber cavities by approaching the concentric limit. First, the cavity length should be optimized to fit best the requirements of the ion-trap design. Next, the radius of curvature can be adjusted to approach the concentric regime for the desired cavity length. Here, as discussed in Section 2.3.2, we have the freedom to select the radius of curvature from a range of possible values spanning almost three orders of magnitude, and we are not limited by the centimeter-scale lower bound that exists for super-polished substrate mirrors. In a last step, the transmission of the mirrors should be chosen in such a way that the minimal failure probability is achieved to create a photon and transmitting it out of the cavity [92], see Equation (2.27).

In recent years, experiments have been carried out in which single trapped ions were coupled to fiber cavities [108–111]. Besides the demonstration of strong coupling of a single ion to fiber cavity, $g_0 \gg \kappa, \gamma_\mathrm{P}$, – recently a step towards this regime was shown in [116] – a further goal is still missing. So far, all demonstrated setups with fiber cavities have been realized with ions in point-like traps [108–111, 116]. Such ion traps have significant micromotion when the ion is displaced from the trap center in all three dimensions, and therefore the coherent manipulation of motion is limited to only one ion in the trap. However, as stated in Chapter 1, the coupling of single ions in a *linear* trap to an optical cavity provides a beneficial quantum platform to scale a quantum computer. Via an efficient and fast quantum communication between remote ion traps, the limited number of ions in a single *linear* trap can be overcome. In such a way, quantum processors could be scaled beyond the limit of classical computations, or quantum communication could be enhanced, e.g. by entanglement purification [117]. Therefore, it would be a breakthrough to couple a single ion in a linear ion trap to a fiber cavity with a cooperativity $C \gg 1$, so that the coherent coupling is dominant.

Chapter 3

Technology of our fiber cavities

This chapter presents the first key part of our experiment: the fiber cavity. First, the relevant cavity parameters are calculated to establish which specifications are necessary for our fiber mirrors. Next, the fabrication of our fiber mirrors is described; we focus on details besides our previously published information [115]. In the last part of this chapter, our characterization of the fiber mirrors is explained.

3.1 Calculation of desired cavity characteristics

In 2012, we decided to produce new fiber mirrors to extend the maximum possible cavity length, as our fiber mirrors of that time restricted us to a maximal cavity length $L \sim 350$ µm [83]. Before the fabrication of new fiber mirrors, known analytical formulas were used to calculate the expected performance of our fiber cavity as a quantum interface (Subsections 3.1.1 and 3.1.2). Based on the known limitations from literature [107], the realistic performance of our desired fiber mirrors was calculated to estimate the required specifications for our new fiber mirrors (see Subsection 3.1.3).

3.1.1 Cavity geometry parameters

The geometry of the cavity is determined by the two curved mirrors, M_1 and M_2, with radii of curvature R_1 and R_2. These mirrors are separated by the cavity length L. A light field with wavelength λ is constrained by the mirrors as boundaries. The first important property of the light mode inside such a cavity is the resonance criterion, which states that the cavity length L equals an integer multiple of half of the wavelength λ [118],

$$L = q \cdot \frac{\lambda}{2} \text{ with } q \in \mathbb{N}. \tag{3.1}$$

The cavity is transmissive and enhances the light field only at these resonances. In the frequency domain, the distance between two resonances can be expressed as the free spectral range [118]

$$\nu_{\text{FSR}} = \frac{c}{2L}, \tag{3.2}$$

where c is the speed of light.

In the paraxial approximation, the light field of the resonator can be described by Gaussian beams [119]. For an asymmetric cavity with $R_1 \neq R_2$, the waist w_0 can be derived as [119]

$$w_0^2 = \frac{L\lambda}{\pi}\sqrt{\frac{g_1 g_2(1-g_1 g_2)}{(g_1+g_2-2g_1 g_2)^2}} \tag{3.3}$$

with $g_i = 1 - L/R_i$ the dimensionless g-parameter of each mirror M_i. Hereby, the amplitude of the electric field inside the cavity drops at a radius w_0 to $1/e$ of the maximum value.

Similarly, the $1/e$ mode radius w_1 and w_2 at each mirror are determined by

$$w_1^2 = \frac{L\lambda}{\pi}\sqrt{\frac{g_2}{g_1(1-g_1 g_2)}}, w_2^2 = \frac{L\lambda}{\pi}\sqrt{\frac{g_1}{g_2(1-g_1 g_2)}}. \tag{3.4}$$

If the waist of this cavity field is defined as the origin, the positions z_1 and z_2 of the two mirrors can be calculated as

$$z_1 = -\frac{g_2(1-g_1)}{g_1+g_2-2g_1 g_2}L, z_2 = +\frac{g_1(1-g_2)}{g_1+g_2-2g_1 g_2}L. \tag{3.5}$$

Then the $1/e$ radius of the light field in the middle of the cavity can be calculated by

$$w_{\text{mid}} = w_0\sqrt{1+\left(\frac{(z_1+z_2)/2}{z_R}\right)^2} \tag{3.6}$$

with $z_R = \pi w_0^2/\lambda$ the Rayleigh length.

To derive real and finite solutions of the equations (3.3) – (3.6), the stability condition has to be fulfilled [118]:

$$0 \leq g_1 g_2 \leq 1. \tag{3.7}$$

This condition means that cavity modes are only stable for cavity lengths

$$0 < L \leq R_s \text{ or } R_b \leq L \leq (R_s + R_b), \tag{3.8}$$

where R_s and R_b are the smaller and bigger radii of curvature, respectively. Consequently, in the instability region, $R_s \leq L \leq R_b$, no stable resonator modes are found.

In Figure 3.1 (a), two mirrors M_1 and M_2 with radii of curvature R_1 and R_2 and diameters D_1 and D_2 are placed in a distance $L = z_2 - z_1$. With the formulas (3.3) – (3.6), the light field between these mirrors can be calculated. The cavity mode is plotted in Figure 3.1 as a red solid line with the waist w_0 at the beam focus, beam radii w_1 and w_2 at the mirrors M_1 and M_2, and beam radius w_{mid} in the center of the two mirrors at positions $z = 0$, z_1, z_2, and $z = (z_1+z_2)/2$, respectively. Additionally, the light mode of a single-mode fiber with waist w_f, is plotted in Figure 3.1 (a) as a green dashed line. Another light mode of a fiber with larger waist w_f', is also drawn as a green dotted line in Figure 3.1 (a).

The coupling from such fiber modes into the light mode of the cavity and vice versa is of special interest as the fiber mode is fixed to its mirror. The coupling efficiency is given by [120, 107]

$$\varepsilon = \frac{4}{\left(\frac{w_f}{w_0}+\frac{w_0}{w_f}\right)^2+\left(\frac{s}{z_R z_R'}\right)^2} = \frac{4}{\left(\frac{w_f}{w_1}+\frac{w_1}{w_f}\right)^2+\left(\frac{\pi n_f w_f w_1}{\lambda R_1}\right)^2} \tag{3.9}$$

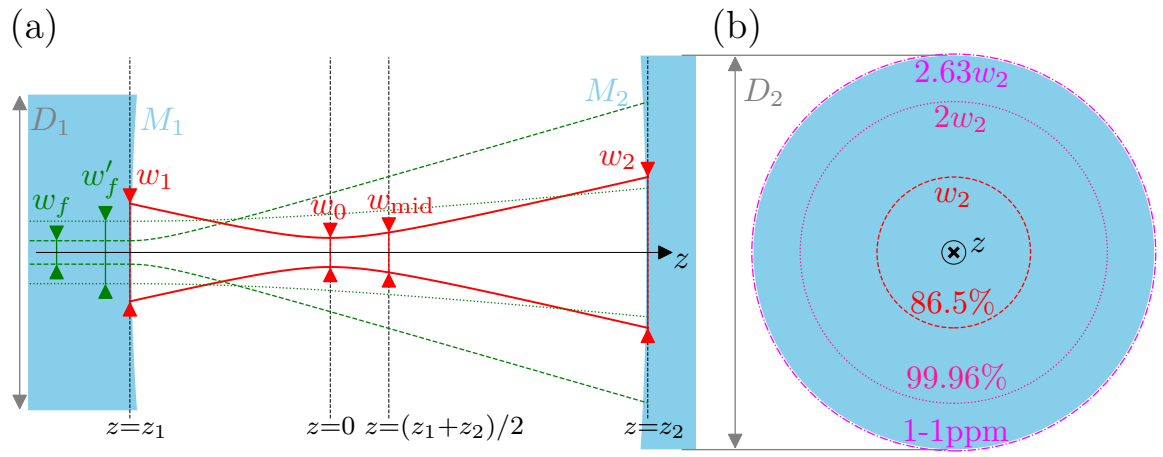

Figure 3.1: Radial and axial sketches of the cavity mode. (a) The radial cavity mode is drawn as a solid line with the mode radius w_1 at the mirror M_1 ($z = z_1$), the waist w_0 at $z = 0$, the mode radius w_{mid} at the center of the two mirrors $z = (z_1 + z_2)/2$, and w_1 at M_2 ($z = z_2$). Furthermore, the dashed line indicates a light field defined by the fiber of mirror M_1 with waist w_f. The dotted line shows the light of the fiber with a larger waist w'_f. The sizes of the mirrors M_1 and M_2 are radially determined by effective useful diameters D_1 and D_2, respectively. (b) The axial view onto the mirror M_2. The dashed circle shows the 1/e mode radius w_2 in which 86.5% of the light power is located. 99.96% of the light is located in the dotted circle. The diameter D_2 is roughly as big as 2.63 w_2, so that only 1ppm of the light is outside of the mirror M_2.

with $s = |z_1|$ the distance between surface of the fiber mirror and the cavity waist w_0, w_f the waist of the fiber, and z'_R the Rayleigh length of the light mode exiting the fiber. Alternatively, the coupling efficiency can be expressed in terms of w_f, w_1, R_1, λ, and n_f the refraction index of the fiber. Note that Equation (3.9) does not consider the penetration depth of the light field into a dielectric coating, which can usually be neglected for our cavity lengths and for resonant light [121].

3.1.2 Cavity QED parameters for asymmetric cavities

The atom-photon coupling strength g_0, the cavity decay rate κ and the atom decay rate γ were introduced in Chapter 2. Here, the formulas of Section 2.2.1 are extended to consider also asymmetric cavities with different radii of curvature ($R_1 \neq R_2$) and mirror coatings.

Similar to the description in Section 2.2, the coupling between a calcium ion and the light at the center of our cavity can be calculated as

$$g_0 = \sqrt{\frac{3c\gamma\lambda^2}{L w_{\text{mid}}^2 \pi^2}}. \tag{3.10}$$

Note that the mode radius w_{mid} in the middle of the cavity does not need to be identical with the waist of cavity. Only for the special case of a symmetric cavity with $R = R_1 = R_2$ is the mode radius w_{mid} equal to the waist of the cavity, w_0; compare Equation (3.6). In Figure 3.1 (a), the

both positions, the waist at $z = 0$ and the center of a asymmetric cavity at $z = (z_1 + z_2)/2$, are illustrated with their different beam mode radii w_0 and w_{mid}.

The cavity decay is also determined by the mirror properties. Each mirror i is characterized by its transmission $\mathcal{T}_i$ and losses $\mathcal{L}_i$. For highly reflective mirrors, the finesse of a cavity simplifies to [119]

$$\mathcal{F} = \frac{\nu_{\text{FSR}}}{\delta\nu} = \frac{2\pi}{\mathcal{L}_{\text{tot}}} = \frac{2\pi}{\mathcal{T}_1 + \mathcal{L}_1 + \mathcal{T}_2 + \mathcal{L}_2}, \tag{3.11}$$

where $\delta\nu$ is the full-width-at-half-maximum (FWHM) linewidth of the cavity and $\mathcal{L}_{\text{tot}}$ describes the total losses of the cavity. Then, the half-width cavity field decay rate can be rewritten as

$$\kappa = \frac{\pi c}{2L\mathcal{F}} = \frac{c\mathcal{L}_{\text{tot}}}{4L}. \tag{3.12}$$

3.1.3 Realistic model for fiber cavities

For fiber cavities, the losses $\mathcal{L}_i$ associated with each fiber mirror M_i not only consist of scatter losses $\mathcal{L}_{\text{scat}}$ and absorption losses $\mathcal{L}_{\text{abs}}$, as known from substrate mirrors, but also may include losses due to the geometry of the cavity. As described in Section 2.3.2, such losses can be approximated by clipping losses which were introduced by Hunger *et al.* for fiber cavities [107]. For an asymmetric cavity, clipping losses

$$\mathcal{L}_{i,\text{clip}}(D_i) = e^{-2\left(\frac{D_i}{2w_i}\right)^2} \tag{3.13}$$

for each mirror M_i are given by w_i the radius of the cavity field at that mirror and D_i the diameter of the mirror M_i. With Equation (3.13), the fraction of the light field is calculated which is not reflected by the mirror. As the size of the light mode with regard to the mirror is illustrated in Figure 3.1 (b), one part per million (ppm) of the light field is clipped for a mirror diameter $D_2 = 2.63w_2$. For fiber cavities, D_i is usually not characterized by the actual cladding diameter of the fiber, but rather by the part of the spherical shape of the mirror. Therefore, the diameter D_i corresponds to an effective useful diameter whose size is given by the losses of its mirrors reflection.

Including these clipping losses in the total losses, using Equation (3.12), the cavity parameters can now be calculated as expected in reality. This brings us to the target parameters for our fiber mirrors. Our main goal was to go beyond the maximal length $L \approx 350$ µm of fiber cavities to which we were limited before 2013 [83]. We noticed that, with a longer fiber cavity, the ion trap could be symmetric and less miniaturized, so that a coupling between ion and cavity is feasible. However, the coupling strength g_0 is inversely proportional to the cavity length L, see Equation (3.10). To keep an atom-photon coupling strength $g_0 > \gamma$, a target cavity length $L = 400 - 500$ µm was chosen. Furthermore, a high finesse up to $\mathcal{F} \approx 140\,000$ should be maintained for such long cavities in order that the cavity decay rate $\kappa < g_0$. For the following cavity configurations, the maximal finesse in the absence of clipping losses is determined by expected absorption and scatter losses of super-polished substrates, additional scatter losses due to a possibly increased surface roughness, and the mirror transmissions; which sum up to $\mathcal{L}_{\text{tot}}(D = \infty) = 45$ ppm, see Table 3.1. To be prepared for fabrication tolerances, we consider additional scatter losses although we have found evidence for our previous fiber mirrors as smooth as super-polished substrates [124].

Table 3.1: Losses of fiber cavities as considered in the presented calculations. The clipping losses depend on the geometry of the cavity and mirrors, so that they are calculated with the Equation (3.13).

Type	Symbol	Mirror 1 (ppm)	Mirror 2 (ppm)	Sum
Scatter & absorption[a]	$\mathcal{L}_{i,\text{sup}}$	2	2	4
Additional scatter[b]	$\mathcal{L}_{i,\text{scat}}$	≤ 12	≤ 12	24
Clipping	$\mathcal{L}_{i,\text{clip}}(D, w_i)$	≥ 0	≥ 0	–
Transmission	$\mathcal{T}_i$	15	2	17
Per mirror	$\mathcal{L}_i$	29	16	–
Total	$\mathcal{L}_{\text{tot}}$	–	–	45

[a] Measured with super-polished mirrors in [122]

[b] Maximal expected scatter losses for $850\,\text{nm}$ light on a CO_2-laser ablated surface with roughness $\leq 0.22(1)\,\text{nm}$ [123, 107]

As presented in Section 2.3, all fiber cavities with ions have been built in a configuration such that the cavity length is smaller than the radii of curvature. Following this state-of-the-art in our community, the easiest approach would be to fabricate mirrors with larger radii of curvature R to build cavities with a length $L < R$. Actually, for fiber mirrors, it is challenging to manufacture mirrors with identical radii of curvature. As one sees from in equation (3.8), both radii of curvature need to be larger than the target cavity length to keep the instability region beyond the target cavity length.

Let us assume a cavity with $R_1 = 600\,\mu\text{m}$, $R_2 = 550\,\mu\text{m}$ and equal effective useful diameters $D = D_1 = D_2$ to achieve the target cavity length of $400 - 500\,\mu\text{m}$. In Figure 3.2(a), the calculated finesse is plotted as a function of the cavity length for $D = 60\,\mu\text{m}$, $D = 65\,\mu\text{m}$, $D = 70\,\mu\text{m}$, and $D = 80\,\mu\text{m}$ considering the losses listed in Table 3.1. A finesse $\mathcal{F} \sim 140\,000$ can be preserved up to $500\,\mu\text{m}$, if the effective useful diameters exceed $D = 70\,\mu\text{m}$. When the quality of the fiber mirrors is further improved such that D is increased, a high finesse of $140\,000$ is possible for longer cavities even up to the instability region, close to the confocal limit ($L = R_2$), indicated as a light green area in Figure 3.2. This configuration would minimize the cavity decay rate κ close to the instability region; see Figure 3.2(b). Additionally, close to the instability region, the waist w_0 of the cavity becomes smaller. You could naively expect the atom-photon coupling g_0' ($\propto 1/w_0$) to increase as a result. However, the waist for the parameters we have chosen in this example, is no longer located in the middle of the cavity (the atom's position) due to the unequal radii of curvature, $R_1 \neq R_2$. In contrast, with the mode radius w_{mid}, the atom-photon coupling strength decreases close to instability region, as seen in the light green shaded area in Figure 3.2(b). The advantage of larger D is therefore canceled out, but actually, a waist w_0 close to a mirror is beneficial for the efficient coupling of light from the fiber to the cavity or vice versa.

The coupling efficiency from the input fiber into the cavity mode is calculated with Equation (3.9), and plotted in Figure 3.2(c) for a single-mode (SM) fiber with a waist of $w_f = 3\,\mu\text{m}$ and parameters listed in Table 3.2. If we choose a larger radius of curvature $R_1 > R_2$ at the SM fiber, the waist is pushed towards that fiber as the cavity further approaches the instability region. The coupling efficiency thereby increases, as shown in the light green area of Figure 3.2(c). Let

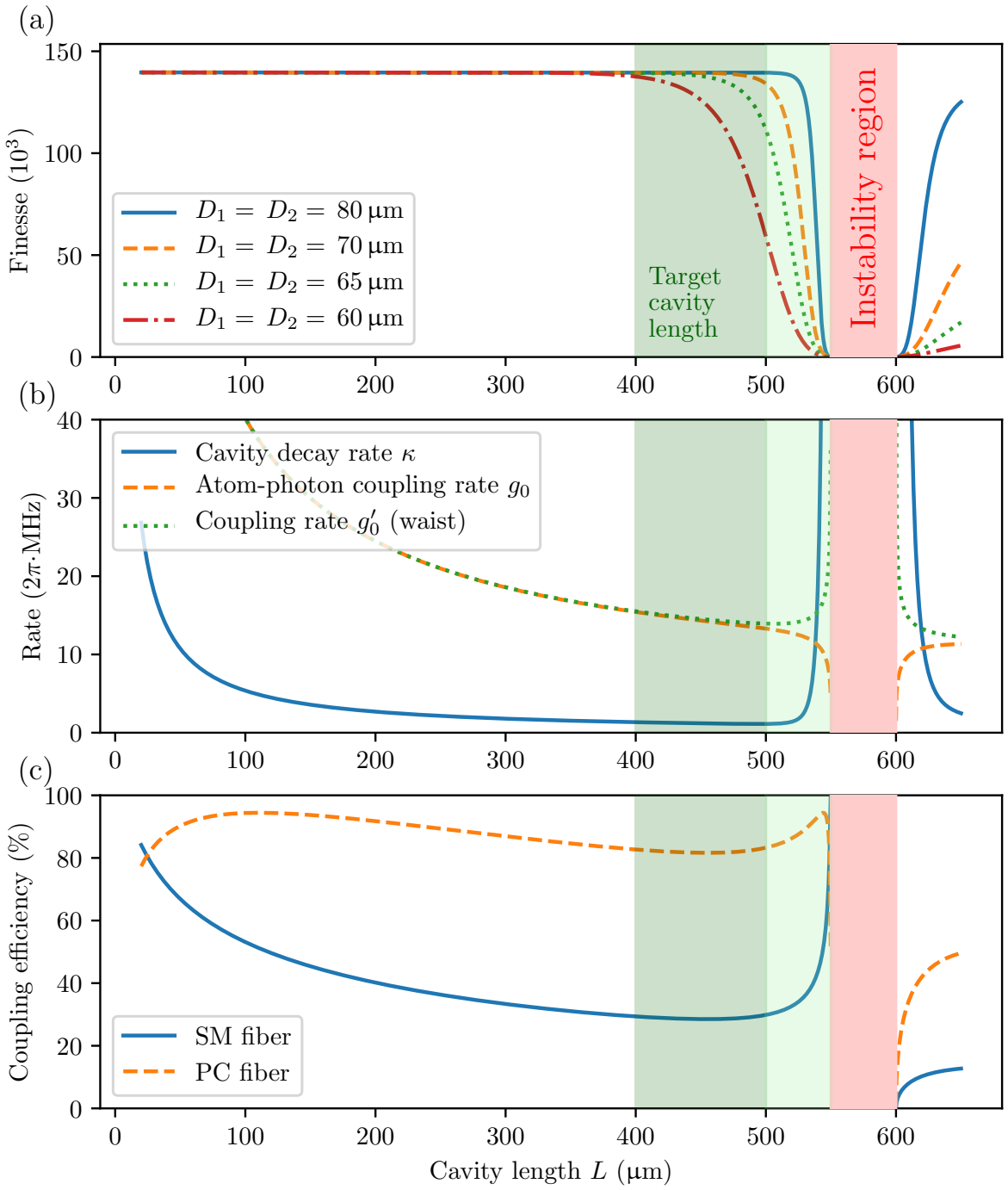

Figure 3.2: Cavity parameters for a cavity with $R_1 = 600$ µm, $R_2 = 550$ µm. Note that the instability region is defined by R_1 and R_2. (a) The finesse is calculated with the Equation (3.11) including losses given in Table 3.1 and additional clipping losses given by Equation (3.13) and (3.4). With $D > 65$ µm, a finesse above 100 000 can be preserved up to the target cavity length, indicated by the dark green shaded area. For $D = 70$ µm, the cavity decay rate κ (Equation (3.12)) is plotted in (b). Additionally, the atom-photon coupling rate g_0 is calculated for the waist w_0 of the cavity (Equation (2.20)) and the mode radius w_{mid} (Equation (3.10) and 3.6)). By approaching the L towards R_2, g_0 decreases for an ion in the middle of cavity (light green area) because the waist moves towards mirror M_1. (c) The coupling from the fiber mode to the cavity-mode is plotted for a SM and a PC fiber; see Equation (3.9) and Table 3.2.

us assume another input fiber with waist $w_f' = 8\,\mu\mathrm{m}$, for example a large mode area (LMA) photonic-crystal (PC) fiber can guide a single-mode with such a waist. The light field of both fibers, SM fiber with w_f and PC fiber with w_f', are sketched in Figure 3.1 (a). Considering this figure, the mode overlap between the PC fiber and the cavity looks larger compared to mode overlap of the SM fiber with the cavity. Accordingly in Figure 3.2 (c), the calculated mode-coupling efficiency of the PC fiber with value from 80% to 95%, as defined in Equation (3.9), exceeds the SM fiber with value from 40%-60% for cavity lengths from $400\,\mu\mathrm{m}$ to $550\,\mu\mathrm{m}$.

The goal of this PhD work was to achieve strong atom-photon coupling, $g_0 \gg \kappa, \gamma$. For this purpose, it is more advantageous than the first cavity configuration, presented in Figure 3.2, to design the cavity such that the target cavity length ($400 - 500$ µm) is beyond the instability region. Therefore, another analysis was carried out for a second cavity configuration with radii of curvature $R_1 = 300$ µm and $R_2 = 350$ µm, and the same calculations were plotted in Figure 3.3 in the same way as in Figure 3.2. Thus for the second cavity configuration, a finesse $\mathcal{F} = 140\,000$ is also achieved at the target cavity length for $D = 70(5)$ µm; see the dark green area in Figure 3.3(a). The second cavity configuration enables a coupling strength $g_0 = 2\pi \cdot 20\,\mathrm{MHz}$, compared to $g_0 \approx 2\pi \cdot 14\,\mathrm{MHz}$ for the first configuration; compare Figure 3.3(b) with Figure 3.2(b). Additionally, now a larger value of D enables a higher atom-photon coupling strength g_0, as seen in Figure 3.3(b). For a value of D exceeding $80\,\mu\mathrm{m}$, the cavity can be brought to the concentric regime, $L \approx R_1 + R_2$, with a coupling strength up to $g_0 = 2\pi \cdot 30\,\mathrm{MHz}$. However, for longer cavities, the mode-coupling efficiency will be reduced by approaching the concentric limit. For the target cavity length, the coupling efficiency $\varepsilon \approx 50 - 70\%$ for PC fibers is again higher instead of only $\varepsilon \approx 30 - 40\%$ for SM fibers; see the green shaded area in Figure 3.3(c).

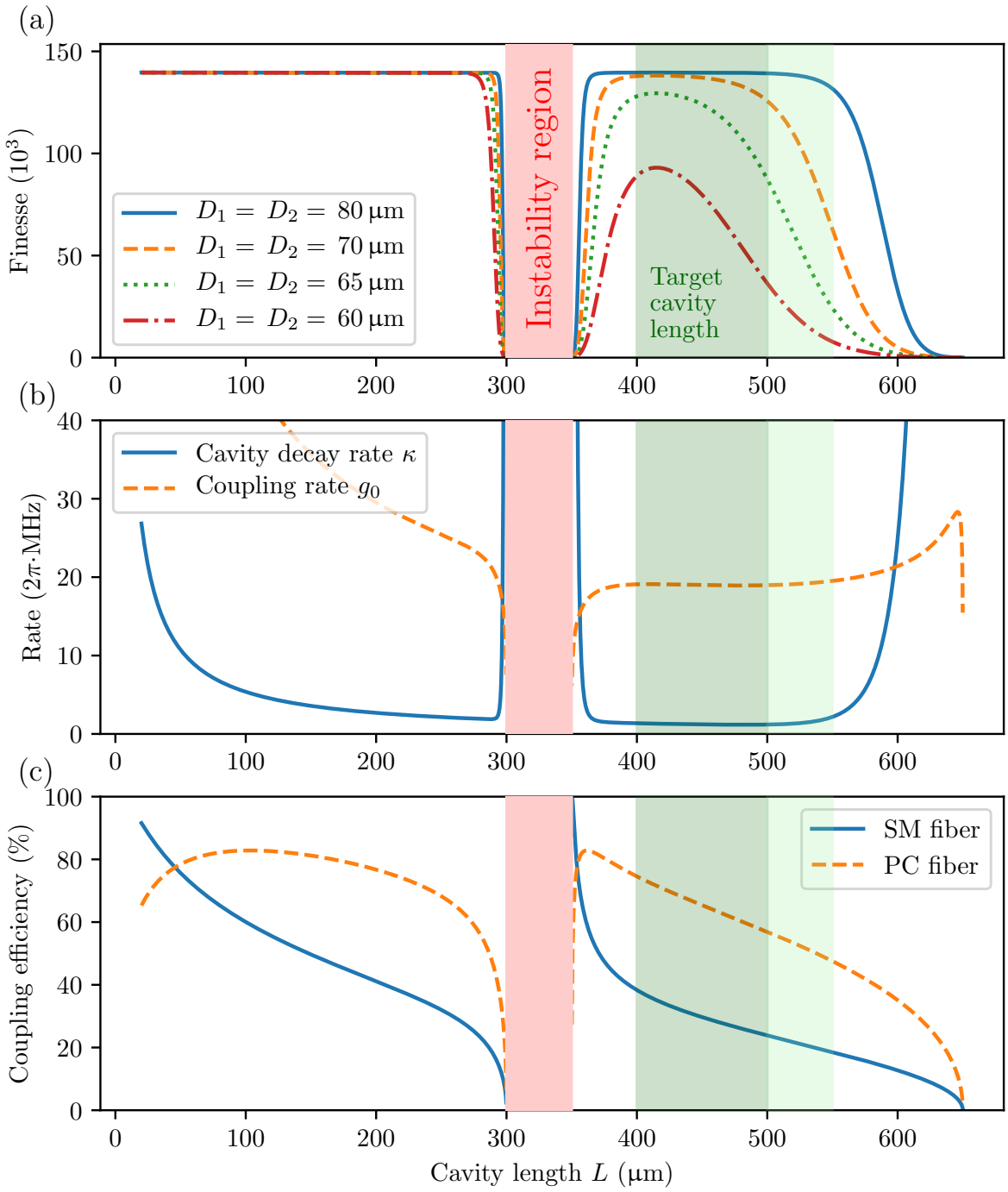

Figure 3.3: Cavity parameters for an optimized atom-photon coupling around $400 - 500$ μm, green shaded area. All calculations were carried out in the same way as in Figure 3.2. (a) With the same values for D as in Figure 3.2, a high finesse $\mathcal{F} = 140,000$ at the target cavity length (dark green area) is achieved by choosing $R_1 = 300$ μm and $R_2 = 350$ μm. (b) The atom-photon coupling rate is increased by one third with respect to that of Figure 3.2. In contrast to Figure 3.2, it stays stable or even increases for longer cavities, light green area. With larger D than $D = 70$ μm plotted here, the cavity decay rate would be maintained low approaching the concentric regime, $L = R_1 + R_2$. (c) The fiber-mode to cavity-mode coupling with a PC fiber is almost three times higher than with a SM fiber for the target cavity length. For longer cavities, both coupling efficiencies are limited and approaching zero in the concentric regime.

3.2 Fiber mirror production

The target parameters of the fiber mirrors were studied in section 3.1. This section presents the methods by which fiber mirrors with the required parameters are produced.

For high-finesse cavities in the visible to near-infrared optical domain with wavelength λ, as used in our experiments, mirrors with losses around a couple of parts per million (ppm) are necessary to achieve a feasible efficiency of the state transfer from ions to photons and vice versa [39]. Stacks of dielectric $\lambda/4$-layers, so-called distributed Bragg reflectors, are able to support reflectivities of $> 99.999\%$, transmissions of a few ppm, and consequently low losses at the same time. Such highly reflective coatings are commercially available. Usually, they are applied to super-polished mirror substrates with a sub-Angstrom roughness [122] to avoid adding additional scatter losses due to the substrate surface. Unfortunately, super-polished substrates are only available commercially for radii of curvature $R > 10\ \mathrm{mm}$ due to the macroscopic polishing technique.

Currently, there are several methods to produce substrates with radii of curvature of $R \approx 0.1 - 1\ \mathrm{mm}$. Femtosecond laser ablation [125] results in a thin layer of molten material or fractures and cracks, neither of which are consistent with the low roughness necessary for high-finesse mirrors. More suitable for high-finesse cavities is the focused-ion-beam sputtering (FIBS) process [126]. Here, surface roughnesses ranging from 0.3 to $0.7\ \mathrm{nm}$ have been achieved [127, 128], but the demonstration of losses in the range of a couple of parts per million are pending. Additionally, an expensive scanning electron microscope with an additional ion beam is required.

The third method is based on laser ablation with a CO_2-laser. As roughnesses less than $0.2\ \mathrm{nm}$ have been achieved [107, 124], we decided in 2014 to continue our collaboration with Prof. Jakob Reichel from 2009 [83]. In the scope of this renewed collaboration, we wanted to set up an improved version of the CO_2-laser setup to fabricate fiber mirrors, suitable for longer fiber cavities. It was not clear if we would be able to meet the required size of the effective useful diameter D, as presented in section 3.1. Especially problematic was whether the mirror surface could be spherically shaped over such a large area, determined by D. Consequently, we searched for further alternatives, and investigated another possibility to achieve spherical fiber facets.

Besides the three methods mentioned above, we found an interesting approach of imprinting the curvature of heated spheres onto fiber facets [129]. Experiments with bare fibers, showing a first successful proof of principle, have been previously carried out as part of a master's thesis project in Stuttgart. So we asked Prof. Giessen whether we could continue these experiments. With expertise and hardware from the Stuttgart group[1], I supervised master's student Dario Fioretto in reconstructing this alternative method of fiber-mirror production [130].

In the end, the successful CO_2-laser ablation in Paris [115] superseded this alternative approach. This section describes the process to fabricate our fiber mirrors. The process is divided into four parts: preparing fibers, ablating fibers with a CO_2-laser, applying highly reflective coatings, and postprocessing PC fibers.

[1] Thanks to Prof. Harald Giessen and Daniel Kunert for sharing their knowledge and for the loan of a couple of devices.

3.2.1 Fiber treatment before CO_2-laser ablation

We decided to fabricate our mirrors on four different types of fibers. The technical specifications are listed in Table 3.2. As suggested in [107], a single-mode (SM) fiber is used to have a defined mode for coupling light into the cavity and later for coupling single photons out of the cavity. Here, we are accepting the given mode coupling, as calculated in Section 3.1, whereas the spatial shape and polarization of the photons are preserved. On the other side, a multi-mode (MM) fiber is used, which provides an efficient way to collect the light of the cavity, but at the cost of losing the spatial shape and polarization of the transmitted light. As shown in section 3.1, photonic-crystal (PC) fibers with a larger mode diameter than SM fibers promise higher mode-coupling efficiencies than SM fibers, especially for long cavities. Therefore, fiber mirrors were additionally fabricated on two kinds of PC fibers with a large mode area (LMA). Our collaborators followed the same strategy, and we published a comparison between PC and SM fibers [115]. Unfortunately, these PC fibers with LMA are only available with an acrylate coating. As this acrylate coating has a high outgassing rate[2], and consequently, the coating is not vacuum compatible, some extra treatment was necessary, described below. Nevertheless, the PC fibers open up new possibilities, whereby the SM and MM fibers, previously used in several fiber cavity experiments worldwide including our own, provide us a safe backup option [83].

Table 3.2: Fibers used for mirror production.

Type	Article	Producer	Core size (µm)	Cladding size (µm)	Coating (inner layer)
MM	Cu200/220[131]	IVG Fiber	200(3)	220(3)	Copper alloy (Carbon)
SM	Cu800/200[132]	IVG Fiber	6(0.5)	200(2)	Copper alloy (Carbon)
PC	LMA-20[133]	NKT Photonics	20(1)	230(5)	Acrylate
PC	LMA-25[134]	NKT Photonics	25(1)	258(5)	Acrylate

Cleaning and stripping fibers

For a successful and reproducible CO_2-laser ablation, as described in the following section, a cleave angle as small as possible is desired. A perfect cleave angle means that the end facet is exactly perpendicular to the fiber axis. To achieve reproducible, precise fiber cleaves, well-stripped and clean fibers are necessary.

Cleaning fibers: A clean lateral surface is achieved by wiping the fiber with an acetone-soaked tissue. A second wipe with methanol helps to end up with less chemical residue. This procedure leaves the end facet of the fiber untouched by the tissue and therefore dirty. This is not a problem because a later cleave of the fiber will produce a clean end facet. Furthermore, for the PC fibers, this untouched end facet is desired to avoid any chemicals penetrating into the holes.

[2]Outgassing Data for Selecting Spacecraft Materials Online: Fiber Recoating Material, PN NSC-06, Secondary Acrylate coating, Total Mass Loss 4.84%, Collected Volatile Condensable Material 0.02%, Data Ref GSC32959

Etching copper coated fibers: For stripping the copper-coated SM and MM fibers, two different etching procedures were used. The first variant is to place the fibers in a one-to-four mixture of iron(III) chloride ($FeCl_3$) with water. Heating the solution in an ultrasonic bath up to $50°C$ accelerates the process, and the fibers are etched within 20 to 30 minutes. This procedure is used for etching a larger number of fibers. The second alternative is a 25% nitric acid (HNO_3) solution. The removal of the copper is then finished in two to three minutes. This method is preferred for etching single fibers, as it is faster but requires handling stronger acids.

Beneath the removed copper coating, an inner layer of carbon remains. For ion-trap experiments this conductive layer needs to be taken into account or should be removed, as problems were reported by colleagues [83]. In contrast to my predecessor Birgit Brandstätter, I removed this carbon layer by burning it with a lighter. This method leaves no obvious residue or damages to the fiber. Birgit scratched the layer off with a diamond paste[3], with the result that scratches in the cladding of the fibers were observed under a microscope.

Stripping PC fibers: The PC fibers with their acrylate coating are not suited for vacuum. Vacuum compatibility is required not only for our experiments but also for applying the highly reflective mirror coating. The coating company allows us only to insert materials which are rated as vacuum compatible into the ion-beam sputtering machines. Therefore, we decided to cut the fibers into pieces of about $15\ \mathrm{cm}$ in length and to remove the acrylate completely. These short fibers can now be stripped by putting them into an ultrasonic bath filled with acetone. After a couple of minutes, the acrylate coating can be pulled off by hand. For this procedure, at least one end of the fiber needs to be closed by melting the holes with a splicer. Otherwise, the holes of the PC fiber will be filled with acetone due to capillary action. In steps of about $5\ \mathrm{cm}$, single fibers can also be mechanically stripped by hand[4].

Special treatment of PC fibers

Bare fibers without any coating are vulnerable. Minor damage to the cladding causes the fiber to break with the next stress, such as bending, pulling or twisting. Therefore, the short bare PC fibers need to be coated with an ultra-high-vacuum (UHV) compatible coating. We decided to use a polyimide coating[5].

Before the polyimide was applied, it was heated for about two to three minutes at $100°C$ on a heating plate. This pre-curing[6] prevents the applied polyimide from forming a bead chain on the fiber, as shown in the inset of Figure 3.4. For a homogeneous coating, the polyimide was applied by the following technique: The fiber was slid through a small droplet of polyimide on a glove at the tip of a finger. By simultaneously rotating the fiber, the coating was applied homogeneously; see Figure 3.4. To increase the thickness of the coating and to avoid the bead chain effect, several layers were applied, one after the other. The applied coating was then cured in an oven under nitrogen atmosphere according to the manual. In a later test, a fiber which was simply cured on a heating plate at $200°C$ for $2\ \mathrm{h}$ without a nitrogen atmosphere was pumped down to $4.5 \cdot 10^{-11}\ \mathrm{mbar}$. We concluded that the applied polyimide coating is UHV compatible for our ion-trap experiments.

[3] Struers, DP-Paste (1 µm)

[4] Micro-Strip precision stripper: MS1-12S-18-FS

[5] PI-2525[135]

[6] Thanks to Yves Colombe for this hint.

Figure 3.4: Polyimide coating of PC fibers after curing in an oven. The inset at the lower right corner shows an unsuccessful application of polyimide without the pre-curing step.

Cleaving fibers

A proper cleave is important not only for the CO_2-laser ablation process [136] but also for splicing fibers. Both techniques are key ingredients of our fiber mirror fabrication. Several different cleavers were used in Innsbruck and Paris, and in the following, some experiences are summarized. For reproducible cleaves, only cleavers should be used which are designed for the cladding size being used. In Innsbruck, we sometimes cleaved thick fibers with unsuitable cleavers[7]. With a maximal tension adjustment, these cleavers were not able to cut the thick fibers. Only by applying an extra force by hand was the fiber cleaved. This technique resulted in end facets with angles larger than $0.3\,^\circ$ with respect to the radial plane [136]. Such cleave angles are inappropriate for CO_2-laser ablation and splicing.

Suitable cleavers include the pneumatic cleaver[8] in Paris and our angle cleaver[9] in Innsbruck. Both cleavers support enough tension to cleave even the PC fiber LMA-25, which has a cladding of $260\,\mu\mathrm{m}$. In adjusting the tension to a new cladding diameter, one should avoid using insufficient tension such that the fiber is not cut at all, because such events probably damage the cleave blade. A starting point for the new tension can be found in the cleaver's manual, or the tension should be increased proportional to the ratio between the new cladding diameter and a known configuration. Then, the tension can be decreased in small steps until artifacts at the fiber facet vanished. Along with the tension, the alignment of the fiber inside the cleaver is also essential, which means that the fiber is clamped as straight as possible into the cleaver. For copper-coated fibers, it is further recommended to straighten the fiber. For example, a pre-pull, by cancelling a first cleave, is suitable, as described in [136].

[7]For example, Vytran FFS-2000 and Photon Kinetics FK11 Precision Fiber Cleaver
[8]NYFORS Autocleaver, Stockholm, Sweden
[9]Fujikura CT-100

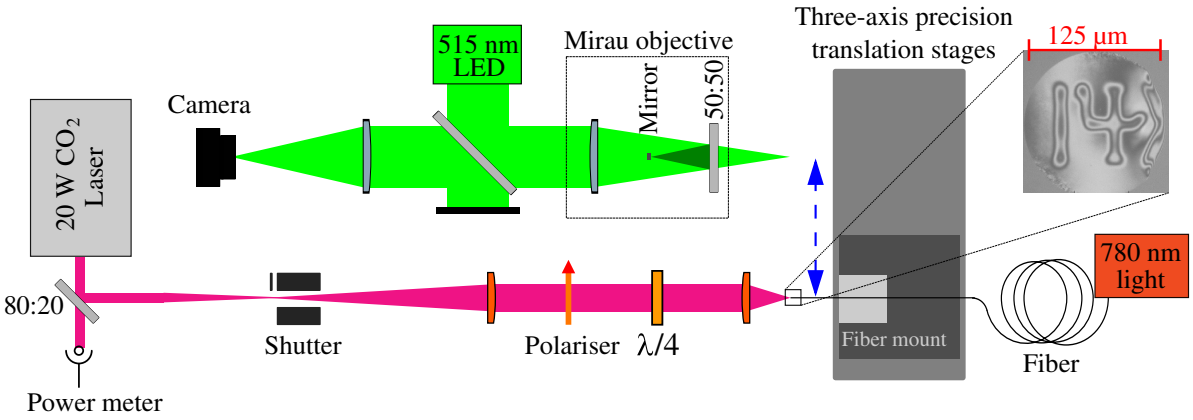

Figure 3.5: CO_2-laser setup in Paris; figure taken from [115], and modified. First, the fiber is ablated by the CO_2-laser beam, indicated by the pink line. Second, the fiber is measured in front of the home-built profilometer; see the green beam path. The inset shows an example of the smallest ablated structures: A $|\Psi\rangle$ was imprinted on the end facet of fiber with standard cladding.

3.2.2 CO_2-laser ablation

The first part of the fabrication of our fiber mirrors was to imprint a spherical, concave shape into the end facet of the fibers. Such a form acts then as a substrate to carry the highly reflective coating. To achieve shapes with the target radius of curvature $R \sim 0.3$–$0.5\,\mu\mathrm{m}$ and a low surface roughness of $\sigma < 0.2\,\mathrm{nm}$, we decided to continue our collaboration with Prof. Jakob Reichel at the Laboratoire Kastler Brossel (LKB) at ENS-Sorbonne Université in Paris. The main task in this collaboration was to set up an improved version of the Reichel group's CO_2-laser ablation setup. In the labs at the LKB, I worked for over 15 weeks, distributed over two years. My coworkers were mainly two PhD students from Prof. Reichel's research group, Konstantin Ott and Sébastien Garcia. During my time back in Innsbruck, I contributed to the Python-based control and analysis software, which I wrote together with Konstantin and Sébastien.

In the CO_2-laser ablation process, light pulses of a CO_2-laser are focused onto the end facets of fibers. The laser pulses, with a length of a few milliseconds and a wavelength of $10.6\,\mu\mathrm{m}$, are absorbed at the surface of the fused silica fibers, and the fiber's facet is heated up so quickly that the fused silica of the fiber evaporates [137]. As a lot of details about our CO_2-ablation process have already been published in the PhD theses of Konstantin Ott [136] and Sébastien Garcia [138] and in two journal articles [115, 139], this subsection gives an overview of the setup, and lists the main achievements and my contributions.

CO_2-laser setup

A CO_2-laser beam[10] was divided by an 80:20 beam splitter; see Figure 3.5. The majority of the power is monitored at a thermal power meter. As the laser was more stable running at a high power, this waste of laser power allowed us to use the appropriate power for the ablation with an increased power stability. The other beam was expanded and collimated by a telescope. At the

[10] water-cooled Synrad V-20

focus of this telescope, a shutter could quickly switch the beam off within 7–9 ms. For proper switching, the laser's duty cycle was switch to 0% while the shutter was being moved. Besides these short interruptions, the CO_2 laser ran continuously with a 20 kHz duty cycle ranging from 70% to 100%. Consequently, the laser was well thermalized, and its power was stable with fluctuation below 1%, which was important for a reproducible ablation process. Afterwards, a polariser cleans the polarization, and a $\lambda/4$-waveplate rotated the polarization of the light to circular polarization, so that the ellipticity of the ablation was minimized [140]. A last lens with a focal length of 25 mm focused the beam onto the fiber's facet. Depending on the position of the second lens of the telescope, the size of the CO_2-laser beam could be adjusted. With this setup, a single ablation pulse could produce Gaussian-like shaped ablations with a waist as small as 5 µm; see inset in Figure 3.5.

The key elements of this improved CO_2-ablation setup were the three-dimensional translation stages[11], which allowed us to move the fibers with respect to the CO_2 laser, and to move the fiber between two positions. At the first position, the fiber was in the focus of the CO_2-laser beam, and the ablation is carried out. At the second position, the fiber could be measured in situ by a home-built profilometer[12], and a surface profile could be reconstructed; see Figure 3.6(a). This procedure superseded a bichromatic mirror, which in an earlier version of the setup has been suspected to disturb the CO_2-laser beam. Furthermore, the fiber could even be automatically aligned in front of the profilometer by coupling 780 nm-light[13] into the opposite end of the fiber. A direct analysis, as described later, allowed us to characterize the CO_2-laser ablation immediately, and as a result, optimizations within minutes were possible by iterations of ablations and characterizations.

Additionally, the translation stages allowed us to apply multiple pulses to a single fiber in a precise way. The translation stages are specified by the manufacturer for a bidirectional repeatability within less than ± 100 nm. Temperature stabilization of the entire setup with fluctuation less than $0.2\,^{\circ}\mathrm{C}$ made it possible for us to position the fiber with a precision of ± 100 nm [138]. With this precise and reproducible movement, spherical surfaces with effective useful diameters up to $D = 100$ µm were possible, as reported in [115]. The major difference between our fibers and the fibers analyzed in [115] is the target radius of curvature R. In contrast to $R \approx 1.5$ mm in [115], for our experiments we aimed for $R \approx 300 - 500$ µm. For smaller radii of curvature, more material needed to be evaporated. Therefore, the CO_2-laser power was increased. With this increased power, the holes of the PC fiber were melted together within the CO_2-laser ablation process. Consequently, the fabrication process was simplified and we saved ourselves the extra fabrication step of collapsing the fiber with a splicer [115, 141].

Analysis of mirror profiles

Besides my work in the laboratories in Paris, I contributed to the programming of the control and analysis software. In particular, I developed major parts of the in-situ analysis in Innsbruck and debugged it afterwards in Paris. Starting with the measured profile of the ablated fiber, the analysis is now carried out in two-dimensions, instead of the one dimensional cuts formerly used [83]. Before a two-dimensional (2D) fit is performed, initial parameters have to be determined

[11] Newport GTS150 and GTS30V, Attocube ECS5050/NUM

[12] Mirau objective Nikon CF IC EPI Plan DI20x, Thorlabs Camera, and green LED (≈ 515 nm).

[13] Thorlabs M780D2

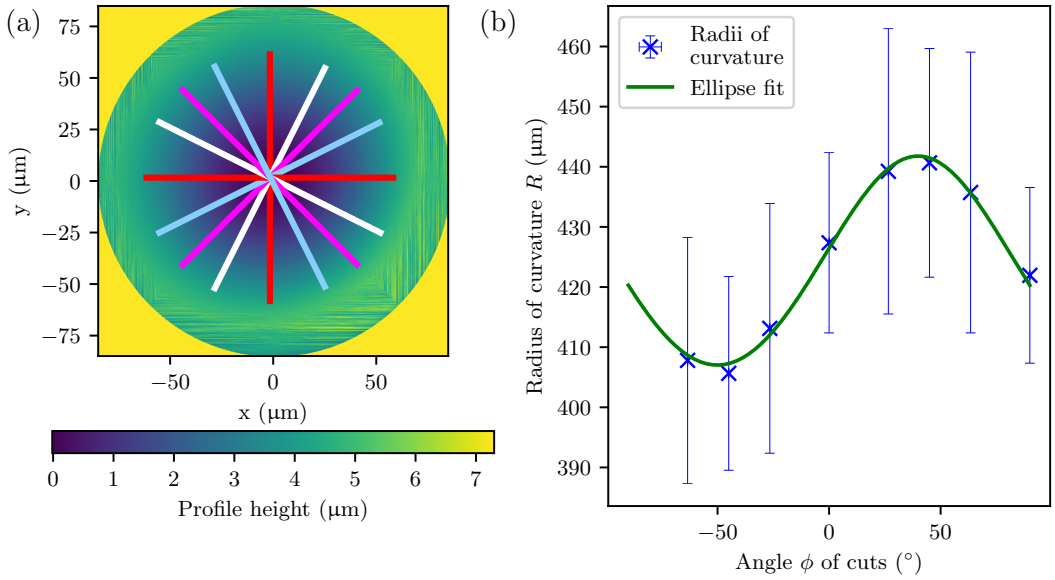

Figure 3.6: (a) Cuts at different angles through the 2D profile of an ablated fiber surface are indicated by different colors. (b) Each cut is fitted with a Gaussian curve. From this fit, the radius of curvature is extracted and plotted against the angle of direction. With a second fit, see Equation (3.14), the direction of semi-axes of the elliptical 2D shape is determined.

so that the 2D fit will converge efficiently. For this purpose, one-dimensional cuts were selected in eight different directions around the minimum of the profile; see Figure 3.6(a). Each cut is fitted with a parabolic function, and the radius of curvature is determined at the center of this parabola. In Figure 3.6(b), these radii of curvature are plotted as a function of the angle of each cut so that the ellipticity of the imprinted structure can be evaluated. The eccentricity ε and angle ϕ of the semi-axes is determined by fitting the function

$$R(\phi) = \frac{R_s}{\sqrt{1 - \varepsilon^2 \cos^2(\phi)}} \tag{3.14}$$

to the data, where the free fit parameters are minor radius of curvature R_s and eccentricity

$$\varepsilon = \frac{\sqrt{R_b - R_s}}{R_b}. \tag{3.15}$$

In particular, a correct orientation of the semi-axes is essential for the 2D fit to converge. The minor radius of curvature R_s, major radius of curvature R_b, and translational shifts of the cuts, determined by the minimum, are used then as initial parameters for the 2D fit.

Several different 2D functions were implemented into the analysis program. A 2D Gaussian curve is close to the shape created by ablation with a single CO_2-laser pulse. A parabolic function closely approximates the desired spherical mirror for small effective useful diameter D compared to the radii of curvature R_s and R_b. Furthermore, for small R_s and R_b and large D, a three-dimensional ellipsoid is also implemented as a fitting function. As the main goal is a mirror shape that is as spherical as possible for a given value of D, these 2D fits can be carried out for different circular region of interests. In this case, the profile is cut to a circular area with

a variable radius of interest around the minimum before it is fitted. Investigating the profile with varying sizes of the region of interest is a useful tool to estimate the effective useful diameter D, as described below.

Comparison of single- and multi-pulse ablation

A good approximation of the fiber surface after a single CO_2-laser pulse is a Gaussian curve [142], but only the inner part of a Gaussian curve can be approximated as a sphere and is suitable as a mirror substrates in fiber cavities. To extend the effective useful diameters D, one can ablate larger structures by selecting larger waists of the ablation laser. However, the maximum waist of the ablation laser is limited by the cladding diameter of the fibers. The edges of the fiber facet are more sensitive to the ablation process because there is less material to absorb the energy of the laser. As a consequence, for a larger waist of the ablation laser, more material at the edge will be ablated. This edge effect creates a convex shape at the outer part of the mirrors which limits the desired concave structure in the middle, so that the size of the spherical structure is again narrowed. With a single ablation pulse, the only way to increase the area over which the ablated region is spherical is to increase the fiber diameters. However, our fibers already have a non-standard cladding diameter of about 200 µm; see Table 3.2. If we were to increase the cladding diameter further, it would restrict our optical access to the ion in between the fiber mirrors.

To overcome this limitation, we developed an ablation scheme with multiple CO_2-laser pulses. For spherical structures, the individual pulses are located along multiple concentric circles. The ellipticity, the diameter, and the number of pulses of each circle is adjustable to optimize the ablation to the desired shape. More details of this dot-milling scheme are explained in [115, 139]. By means of this method, we were not only able to enlarge the effective useful diameters that we can produce, but also to compensate for the different absorption outcomes of the CO_2-laser at the cladding and at the core of a SM fiber. As an example, we now compare the dot-milling process to the earlier method of ablation with a single laser pulse at fibers with a target radius of curvature $R = 330$ µm.

In Figure 3.7, the analysis of two fibers ablated using the two different methods is shown. Fiber SP was fabricated by single-pulse ablation. In contrast, fiber MP was ablated with multiple pulses. In Figure 3.7(a), the two radii of curvature R_1 and R_2 of each fiber are plotted as a function of D. The radii were extracted as the semi-axes of a 2D parabolic fit with different sizes of the fitting area with diameter D. For small $D = 30-40$ µm, the fitted radii of curvatures are found to be around the target $R = 330$ µm. However, already for these diameters, the multi-pulse scheme is found to outperform single-pulse ablation by achieving a significantly smaller ellipticity. Considering D up to 100 µm, the fitted radii of curvature due to single-pulse ablation have increased by $\Delta R > 10\%$, whereas the radius of curvature of multi-pulse ablation has only changed by $\Delta R < 2\%$. The mean difference Δ_{mean} between the 2D fit and the measured profile is shown in Figure 3.7(b) as a function of the diameter D. Again the multiple-pulse ablation is found to be superior to the single-pulse one: The fiber SP has a $\Delta_{\text{mean}}(D = 100\ \mu\text{m}) = 45$ nm, whereas, fiber MP has just $\Delta_{\text{mean}}(D = 100\ \mu\text{m}) = 8$ nm. Consequently, the fiber MP is closer to a spherical surface over a larger area of the mirror.

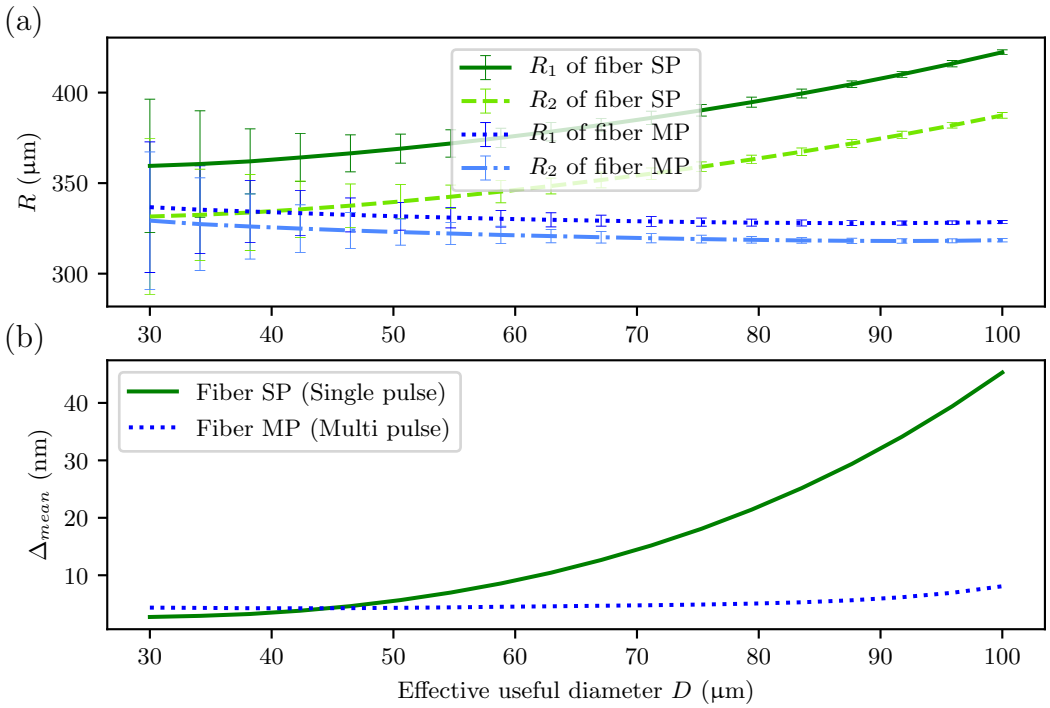

Figure 3.7: (a) With an elliptical 2D parabolic fit of each fiber's measured profile, the two radii of curvature along the two main axes are extracted. The radii of curvature are plotted for the two fibers MP and SP as a function of the size of the fitting area characterized by the diameter D. Fiber MP was produced by multi-pulse ablation, and is found to have nearly constant radii of curvatures up to $D = 100$ µm. Fiber SP was ablated by a single pulse, and the radii of curvature are found to have a strong dependence on D. (b) The mean deviation Δ_{mean} between the 2D fit and the measured profile increases with D for the single-ablation-pulse production. In contrast, Δ_{mean} for the multi-pulse-ablation fabricated fiber MP shows a much smaller increase with D.

3.2.3 Highly reflective coating

After the CO_2-laser ablation, the second part of the fiber-mirror fabrication is the highly reflective coating. Here, it is very important that the coating has ultra low scatter and absorption losses, as listed in Table 3.1, such that our target transmission is optimized for these expected losses. Dielectric highly reflective coatings are applied by ion beam sputtering. They are commercially available at a couple of companies including Advanced Thin Films and Five Nine Optics, both in Boulder, Colorado, and Laseroptik in Garbsen, Germany. As Five Nine Optics was just founded recently and Laseroptik only recently started to coat fiber mirrors, we decided in 2013 that our new batch of fibers should be coated by Advanced Thin Films (ATFilms). We had good experiences and a personal contact with this company from our first batch of fibers in 2009 [83].

Characteristics

For an optimized CQED experiment, the fiber cavity mirror coatings were designed to be asymmetric. On the one hand, the MM fiber should be as reflective as possible. On the other hand,

the goal for the SM or PC fiber is to couple photons out of the cavity, but there is a trade-off between a high finesse and high transmission. With losses expected on the order of those in Table 3.1, the target transmissions for the SM fiber $\mathcal{T}_{\mathrm{SM}}$ and for the MM fiber $\mathcal{T}_{\mathrm{MM}}$ at the ion-transition wavelength $\lambda = 854\ \mathrm{nm}$ were chosen as the following:

$$\mathcal{T}_{\mathrm{SM}}(\lambda = 854\ \mathrm{nm}) = 15\ \mathrm{ppm}, \tag{3.16}$$

$$\mathcal{T}_{\mathrm{MM}}(\lambda = 854\ \mathrm{nm}) = 2\ \mathrm{ppm}. \tag{3.17}$$

As we intended to use another laser with $\lambda \approx 785\ \mathrm{nm}$ to stabilize the fiber cavity to the ion's transition wavelength (see Section 4.5.2), the cavity mirrors also require well-chosen transmissions for that laser. From experiences in our research group, we estimated that the finesse for locking should be $30\,000$ or less so that we aimed for coatings with:

$$\mathcal{T}_{\mathrm{MM}} \cup \mathcal{T}_{\mathrm{SM}}(\lambda = 785\ \mathrm{nm}) < 100\ \mathrm{ppm}. \tag{3.18}$$

ATFilms designed two coating runs to reach our goals: The coating of the MM fiber has 47 alternating layers of SiO_2 and Ta_2O_5, including an SiO_2 base layer and cap layer, and is designed for transmission of 1.8 ppm. The coating of the SM fiber has 41 layers (including the SiO_2 cap and base) and is designed for transmission of 13 ppm. To fulfill the desired transmissions at $\lambda = 785\ \mathrm{nm}$, the resonance wavelength for the 2 ppm-coating run was shifted from our target of $\lambda = 854\ \mathrm{nm}$ to a smaller wavelength $\sim 850\ \mathrm{nm}$. We have chosen SiO_2 as the cap layer to increase the robustness against ultra-violet laser light [143]. Both coating runs were applied without any active-set radius-of-curvature compensation[14].

Measurements of substrate mirrors

Along with our fibers, super-polished substrates purchased from ATFilms with radii of curvature of 50, 100, and 1000 mm and planar substrates were coated in both coating runs. These substrate mirrors were used to characterize the coating independently of the contributions from the fiber mirrors, such as from the non-spherical shape or from potential additional roughness. First, the transmission of the mirrors was tested. ATFilms provided us data from a spectrophotometer[15] from 700 to $1000\ \mathrm{nm}$ for both coating runs. In Figure 3.8, their measurement of the 15 ppm coating is plotted as a function of the wavelength as a light red solid line between $700-1000\ \mathrm{nm}$. The entire spectrum was covered by two gratings. At $861\ \mathrm{nm}$, these two gratings are changed, and thus the measured data is noisy. For the 2 ppm curve, the light green solid line in Figure 3.8, the sensitivity of the spectrophotometer is only rated to a transmission of 10 ppm, which is seen to be in the noise between 800 and $900\ \mathrm{nm}$. Nevertheless, a mean transmission of $2(3)$ ppm and $17(3)$ ppm between 800 and $860\ \mathrm{nm}$ can be determined for the 2 ppm and 15 ppm coatings, respectively. With the measured transmissions of 8 ppm and 50 ppm at $\lambda = 785\ \mathrm{nm}$, all requirements are met; see Equations (3.16), (3.17) and (3.18).

A transmission measurement was also carried out in our labs. Josef Schupp of the Quantum Frequency Conversion Team measured the transmission through mirrors of the same coating runs with a power meter. The laser light[16] was focused with a $75\ \mathrm{mm}$ lens to avoid any etalon

[14] Personal e-mail contact with Howard Champoux, technician at ATFilms

[15] Perkin Elmer 900

[16] M Squared SolsTiS narrow linewidth Ti:sapph laser

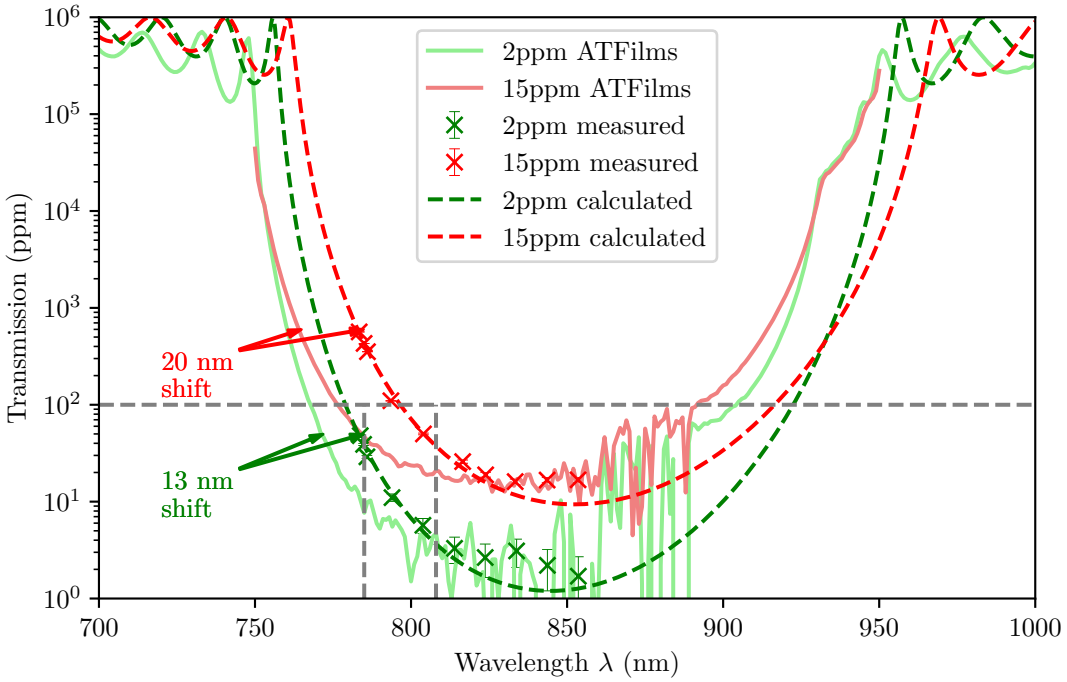

Figure 3.8: Coating spectra. Spectrometer measurements provided by ATFilms are plotted as light green and light red solid lines for the 2 ppm and 15 ppm coating runs. Courtesy of ATFilms. The crosses present our measurements in the lab with the same color coding. Shifts of 13 nm and 20 nm were found between the measurements of ATFilms and us for the coating with 2 ppm and 13 ppm, respectively. Calculated transmissions (dashed lines), following [144], were fitted to our measurements. The known materials and number of layers of the coating were set, and the resonance frequency was the only free parameter. The gray dashed horizontal line shows the target maximum transmission at 785 nm (left vertical dashed line). To fulfill our requirement, Equation (3.18), we changed the wavelength of our locking-laser from the intended value of 785 nm to 808 nm, indicated by the right vertical dashed line.

effect by the non-coated back of the mirror. Beforehand, a measurement error of 1 ppm of the power meter was determined by measurements with different configurations of neutral density filters. The wavelength was measured by a wavemeter[17] with an uncertainty of 2 MHz. At 853 nm, both coating runs met the specifications: 16(1) ppm and 2(1) ppm; see crosses in Figure 3.8. At 785 nm, the transmission of the 15 ppm coating is above the target value of 100 ppm; see above the maximum target transmission, indicated by the crossing point of the horizontal dashed line and left vertical dashed line in Figure 3.8. As indicated in Figure 3.8 at a wavelength of 785 nm, we found a shift of 13 nm and 20 nm, between the measurement of ATFilms and the measurements in our labs of the 15 ppm and 2 ppm curves, respectively. Such shifts can be explained by annealing the mirrors [145], as we annealed the mirrors ourselves between the measurements.

Using the specifications of ATFilms, namely the refraction indices of the materials for used

[17] High Finesse Wavelength Meter WS8-2

range of wavelengths ($n_{\mathrm{air}} \approx n_{\mathrm{vac}} = 1$, $n_{\mathrm{Ta_2 0_5}} = 2.05$, and $n_{\mathrm{SiO_2}} = 1.457$) and the number of layers, I calculated the transmissions of the quarter-wave stacks, following the formulas for thin films given in [144]. Only the resonance wavelength of the stacks, meaning the thickness of the layers, is fitted to our measurements; resulting in resonance wavelengths of $845\ \mathrm{nm}$ and $852\ \mathrm{nm}$ for the 2 ppm and 15 ppm curves, respectively. The dashed colored lines in Figure 3.8 show these calculated transmissions.

To determine the coating properties fully, the losses of the substrate mirrors were investigated. Such super-polished substrate mirrors can have scatter and absorption losses as low as $\mathcal{L} \approx 1.1$ ppm [122], while clipping losses are negligible. A cavity built with these mirrors is an appropriate tool to characterize the coatings. Via cavity ring-down measurements [81], Josef Schupp determined the finesses of different configurations of our mirrors with radius of curvatures of $50\ \mathrm{mm}$; see Table 3.3. With Equation (3.11) and subtracting the measured transmissions at the wavelength of $853\ \mathrm{nm}$, these measurements show mean scatter and absorption losses of $\mathcal{L} = 21(2)$ ppm independent on the coating run. To achieve mirror losses of a few ppm, an annealing process is required to homogenize the oxide layers [146]. As materials coated on the fibers' claddings and clamped in the fibers' holders would not sustain the temperatures of an annealing process [83], the annealing was not carried out by ATFilms. In our labs, after these measurements, the mirrors were heated up to $450\ ^{\circ}\mathrm{C}$ over $4\ \mathrm{h}$, held at that temperature for another $2\ \mathrm{h}$, and ramped down to room temperature in $4\ \mathrm{h}$, as suggested by ATFilms. Actually, due to the well-insulated oven, the ramp-down took almost one day. After this annealing process, the finesse measurements were carried out again, which demonstrated mean losses $\mathcal{L} = 3(2)$ ppm per annealed mirror. Thus, we see that the annealing reduced the losses by $18(2)$ ppm per mirror, equal for both coating runs.

Table 3.3: Finesse measurements of substrate mirrors before and after annealing. The losses were determined by calculating the total losses from the measured finesse and subtracting the measured transmissions.

Mirror	Finesse		Losses (ppm)	
configuration	before	after	before	after
15ppm/15ppm	90,000	175,000	38(2)	4(2)
2ppm/15ppm	101,000	252,000	44(2)	7(2)
2ppm/2ppm	135,000	708,000	43(2)	5(2)

Annealing of fiber mirrors

Like the substrate mirror coatings, the coatings of the fiber mirrors were annealed in our lab to reduce their losses. However, the entire fibers could not be heated up in the annealing process, as the annealing of the copper-coated fibers did not work for us in the past in an ordinary oven [83]. We suspect that the copper oxidizes at the annealing process, which then deposits on the mirror coating. In Paris, a home-built fiber annealing station was developed which heated just the tips of the fibers [138]. We rebuilt this annealing device in our lab. A detailed description of this setup is given in Section A.1. The temperature of this setup was calibrated by a dummy run in which a thermocouple sensor attached to a multimeter was heated instead of a fiber. Here, we observed that the setup could not reliably heat up the thermocouple to more than $350^{\circ}\mathrm{C}$.

Higher temperatures caused a change of the resistor of the heating wire or even melted glass which enveloped the fiber. Consequently, the heating recipe of ATFilms was not suitable for this setup, so we used another annealing process suggested by Laseroptik Garbsen with a maximal temperature of $300°\mathrm{C}$ for 8 hours. This annealing recipe was also used in Paris.

Table 3.4: Losses (scatter, absorption, and clipping losses) of fiber cavities determined by finesse measurements at a certain cavity length before and after annealing. The names of the fibers follow our internal labeling of fibers.

Name of fibers SM*/PC - MM	Before annealing $\mathcal{L}$ (ppm) @ L (µm)	One annealed $\mathcal{L}$ (ppm) @ L (µm)	Both annealed $\mathcal{L}$ (ppm) @ L (µm)
D9* - B10	80(5) @ 250	65(5) @ 250	48(5) @ 250
L5 - O5	73(5) @ 200	57(5) @ 200	—
K9 - O7	—	73(5) @ 200	46(5) @ 200
G5 - P1	—	59(5) @ 200	40(5) @ 200

During my PhD work, several fiber cavities were measured under different conditions: before any annealing, with only one fiber annealed, and with both fibers annealed. Table 3.4 lists losses extracted from different finesse measurements of cavities formed from these mirrors, which were measured under at the least two different annealing conditions at the same cavity length. Additionally, this list contains only annealing processes with an increased finesse afterwards, as a reduction in finesse is considered to be caused by a contamination or damage of the mirror surface. Such reduction in finesses can happen by handling the fibers; for example at the process of inserting the fibers into the annealer or taking them out again, the fiber could be contaminated by dust particles in the air. An unchanged finesse is also neglected, as it is possible that the annealing process did not work.

Note that the measured transmissions of the substrate mirrors have already been subtracted from the losses in Table 3.4. For our purposes, only the change between the two annealing conditions is interesting. Here, we found a mean improvement of $19(9)$ ppm per annealing step, which agrees with the change observed when annealing the substrate mirrors within the margin of error. In conclusion, these measurements indicate that annealing reduces the fiber mirror losses. However, a systematic study which relies on statistically convincing data without any human filtering has not yet been carried out.

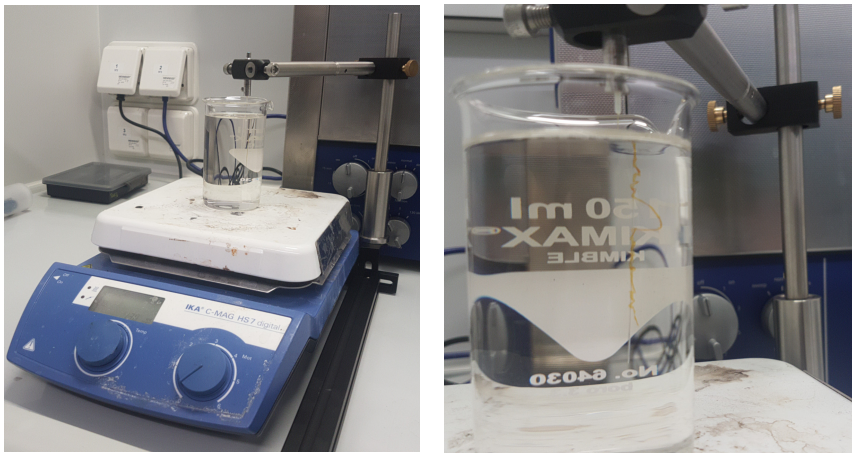

Figure 3.9: Etching polyimide coating of a PC fiber with highly concentrated sulfuric acid. Left: A glass beaker with sulfuric acid on a heating plate. Right: A close-up photo with the polyimide fiber coating loosely connected to the fiber.

3.2.4 Preparing photonic-crystal fibers for vacuum

The PC fiber mirrors were fabricated on fiber pieces with a length of about $15\ \mathrm{cm}$. These short pieces were necessary so that we could easily remove the entire acrylate coating along each piece and recoat it completely with a UHV-compatible polyimide coating, as described in Subsection 3.2.1. Additionally, these short fiber pieces saved money, as the PC fiber costed roughly 100 EUR/m. To prepare the mirrors on the PC fibers for our experimental setup, PC fibers with a length of roughly $1.2\ \mathrm{m}$ were spliced onto the short fiber mirrors. For some splices, it was necessary to remove a part of the polyimide coating that we have applied before.

Polyimide etching

For our polyimide-coated PC fibers, etching was the best way to strip the polyimide before splicing. Highly concentrated (95%-97%) sulfuric acid was prepared in a glass beaker on a heating plate at a temperature of $130-150^{\circ}\mathrm{C}$. Then, the fiber with the polyimide coating was dipped into the acid as deep as the coating should have been removed. The coating was released within $2-5\ \mathrm{min}$; see Figure 3.9. Afterwards, the fiber was cleaned in deionized water. With an acetone-soaked tissue, the fiber was wiped off to remove the loose polyimide-coating pieces. This etching process was repeated as long as there were coating residues. As we used PC fibers, it was essential that the holes on at least at one side of the fiber have been collapsed prior to etching. Otherwise, the acid would be sucked into these holes by capillary action. A subsequent splice would have burned the fiber in an unpredictable way. If the polyimide coating were removed on the side with the open holes and the fiber were only collapsed on the other side, the acid could still penetrate a couple of centimeters. Thus, the cleave needed to be placed at a distance sufficiently far from the end of the fiber that no acid residues remained at the splice.

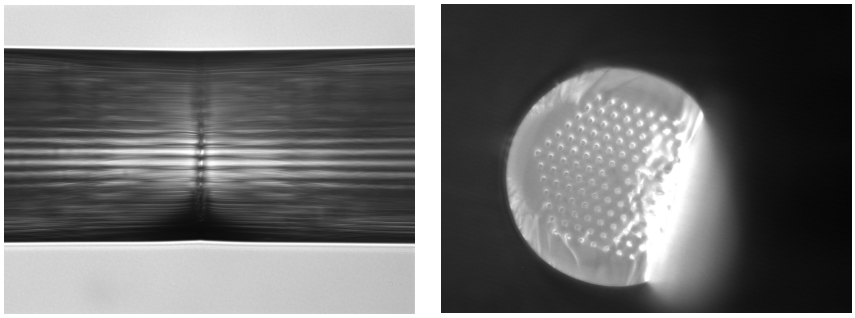

Figure 3.10: Left: Successfully spliced PC fiber. The holes are preserved and no final gap is visible. Right: Broken fiber splice that was melted together only at the right side.

Splicing PC fibers

The process of splicing PC fibers was different than the process for conventional solid fibers. As a starting point, the producer of the PC fibers has provided an application note that explains how to splice PC fibers [147]. In our laboratories the same fusion splicer[18] that was used in their guidelines was available. The cleaved fibers were aligned automatically by the splicer to a defined gap of a couple micrometers, called Pre-Gap. Before the splice, the gap between the fibers was reduced to $1\ \mu\mathrm{m}$ manually instead of using the Pre-Push option of the splicer that moves the fibers by a configurable distance before the actual splice. This procedure allowed us to use the automated aligning system of the splicer in a reliable way and to check that the fibers were still properly aligned after the manual fiber movement. Finally, the actual splice was carried out. A splice consists of a movement of the fiber (Hot-Push) with a adjustable speed (Hot-Push-Velocity), which could be delayed by the Hot-Push-Delay, and heating of the filament with a settable power (Power) for a adjustable duration (Duration).

As mentioned in NKT's guidelines, there is a trade-off between optical transmission and mechanical stability. For transmission-optimized splices of PC fibers, we have seen that the splice was performed only weakly, that was for a short duration and with low power; see Table 3.5 which lists all values for the adjustable parameters. Additional pulses with reduced power (After-Pulses) and without any movement of the fiber (no Hot-Push) were applied after the first splice, which were observed to increase the mechanical stability, as also reported in the guidelines. The guidelines also report that an increased mechanical stability is achieved with a minor Hot-Push of a few micrometers. With a diode laser beam[19] coupled into one fiber, the transmitted power was measured at the other side of the fiber before, during, and after splicing. With optimized parameters and cleaves with angles smaller than $0.2°$, transmissions up to 98% were achieved. However, the mechanical strength of these splices was not reliable, as such spliced fibers often broke at a bending radius $\sim 5{-}10\ \mathrm{cm}$. After breaking at such large bending radii, the spliced fiber facet usually was found to have only one melted connection at one side of the edge, as seen on the right-hand side of Figure 3.10. With a splice protection, commercially available, these weak splices could be protected against mechanical stress.

As there are already optical losses at the cavity mirrors and at the coupling between the cavity and the fiber mode, we can tolerate additional losses at the splice. With this compromise,

[18] Vytran FFS 2000 filament fusion splicer, nowadays distributed and maintained by Thorlabs
[19] Toptica DL 100: $\lambda \approx 854\ \mathrm{nm}$

Table 3.5: Parameters and values for splicing PC fibers.

Parameter	High Transmission	Mechanical Stability
Pre-Gap	5 µm	8 µm
Pre-Push (manually moved)	4 µm	7 µm
Hot-Push	10 µm	18 µm
Hot-Push-Velocity	10 µm/s	9 µm/s
Hot-Push-Delay	0 s	0 s
Power	22.5 W	$23 - 24.5$ W
Duration	1 s	2 s
After-Pulse-Power	22.5 W	-
After-Pulse-Duration (without Hot-Push)	4×1 s and 1×1 s	-

we can favor greater mechanical strength by sacrificing optical transmission. By means of stronger splices, that is splices of longer duration and greater power (see Table 3.5) bending radii down to several millimeters were achieved. Actually, the fibers spliced using these parameters broke mostly next to the splice during our tests, indicating that the splice is even more stable than a bare fiber. However, the transmission of such fibers was found to be reduced to 65–80% of their pre-splice value. Other approaches like using larger values for the Pre-Gap for melting the entire surface of the fiber facet were tested, but correspond to worse performance compared to the two methods presented.

3.3 Characterization of fiber mirrors

As previously discussed in Section 3.1, the main challenge in constructing fiber cavities is to achieve a spherical mirror shape, which is characterized by the effective useful diameter D. To evaluate whether multiple pulses have improved the CO_2-laser ablation process, we characterized the produced fiber mirrors, mainly by measuring the finesse of fiber cavities as a function of the length of the cavity. Through the comparison of the measurements with theory, the effective useful diameter could be determined.

First, the experimental setup is presented with which we measure the finesse as a function of the cavity length. Then, a short summary is given of Florian Kranzl's master thesis project, about measurements of a hybrid cavity consisting of a fiber mirror and a substrate mirror. Afterwards, two measurements are presented which demonstrate the restrictions that we face in implementing fiber mirrors into the design of the ion trap. The corresponding ion-trap design with integrated fiber cavity is presented afterwards in the next chapter.

3.3.1 Experimental setup and measurement method

The finesse is the ratio between the free spectral range ν_{FSR} and the linewidth $\delta\nu$ of the cavity; see Equation (3.11). Combining Equation (3.11) with Equation (3.2), we can express the finesse in terms of the linewidth $\delta\nu$ and cavity length L:

$$\mathcal{F} = \frac{c}{2\delta\nu L}. \tag{3.19}$$

To determine both of these parameters, the following setup was used (Figure 3.11). The beam of a diode laser[20] with wavelength $\lambda = 840 - 850\ \text{nm}$ was coupled into the SM or PC fiber. The entire wavelength range of the diode laser was within the target transmissions defined for our coatings; see Figure 3.8. With the MM fiber mounted on a six-axis positioner[21], the fiber cavity was aligned by adjusting all three translational degrees of freedom and all three angles. In the plane transverse to the fiber cavity axis, micrometer screws[22] allowed us an alignment with a precision of a few micrometers. For a more precise alignment down to tens of nanometers, we applied voltages to the piezos built into the six-axis positioner. The length of the cavity was controlled by a stepper motor[23] for rough alignment and scanned by applying an alternating voltage on the built-in piezo. A frequency generator was connected in the Bias-T configuration with the diode laser to modulate the laser light in frequency. Transmission peaks of the cavity with the carrier and the two sidebands were detected on the fast photodiode PD_{trans}[24] with a bandwidth up to $400\ \text{MHz}$. The corresponding time traces of these resonances from the cavity were recorded on an oscilloscope[25]; and saved on a computer.

To determine the linewidth $\delta\nu$ of the cavity resonance, the sideband frequency was used to calibrate the time axis of the oscilloscope traces. By fitting a curve to the time traces consisting of the sum of three Lorentzian functions (see the right inset in Figure 3.11) the distances

[20] Toptica DL-pro

[21] Thorlabs NanoMax NanoPositioning Flexure Stage

[22] Thorlabs DRV3 $8\ \text{mm}$ High Precision Differential Micrometer

[23] Thorlabs DRV001 8 mm Travel Modular NanoMax Stepper Motor Drive

[24] Thorlabs APD430A/M Si Variable-Gain Avalanche Detector, Temperature Compensated, 400–$1000\ \text{nm}$, DC $400\ \text{MHz}$, M4 Taps

[25] Keysight MSOX3104A

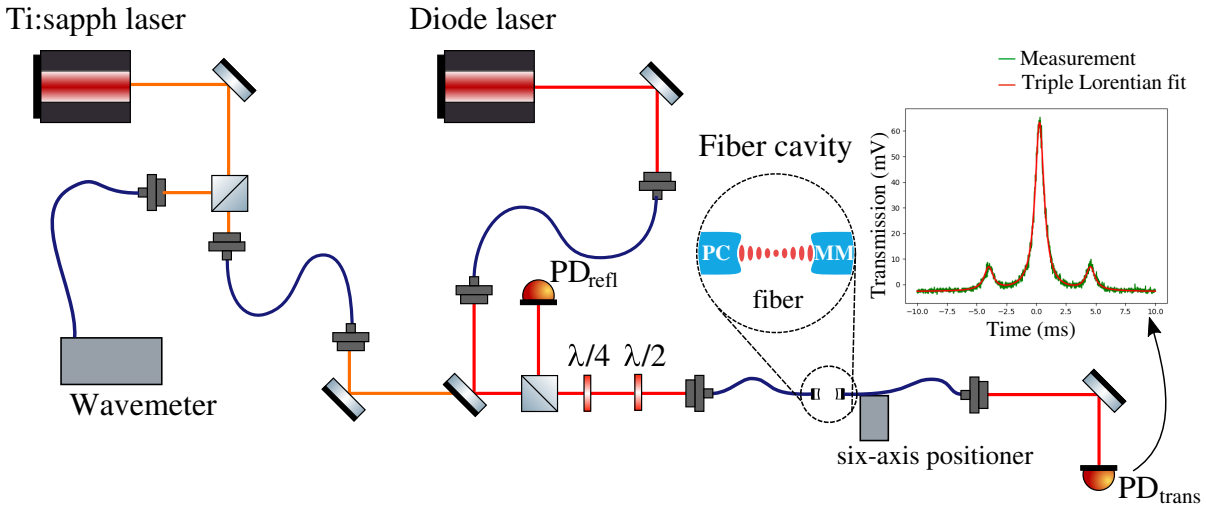

Figure 3.11: A Ti:sapph laser and a diode laser are coupled into the PC fiber. The absolute frequency of the Ti:sapph laser is measured by a wavemeter. A $\lambda/4$-plate and a $\lambda/2$-plate are used to align the laser polarization to one of the birefringent axes of the cavity. To align the cavity, the MM fiber is mounted on a six-axis stage. Behind the MM fiber, a photodiode detects the fiber cavity transmission, an example of which is shown in the inset.

between the sidebands and the carriers as well as the common linewidth of all three Lorentzian curves were extracted in terms of time. With the known frequency conversion, these values were translated into frequencies, yielding linewidth $\delta\nu$. The same measurement could be carried out with the reflected signal on the photodiode $\mathrm{PD_{refl}}$. Here, the reflected signal could be asymmetric depending on the cavity alignment, and the formula for the reflected signal needed to be fitted as presented in [148].

In a birefringent cavity, the two polarization eigenmodes are not degenerate, that is, shifted in frequency. It is known that elliptically shaped fiber mirrors lead to these non-degenerate polarization modes in fiber cavities [140]. Depending on the polarization of the in-coupled light, either one of both modes is excited. If the frequency difference between these polarization eigenmodes is on the order of the cavity linewidth, the excitation of both modes simultaneously could lead to an effective broadening of the measured linewidth. To avoid this, a $\lambda/4$-plate and a $\lambda/2$-plate were placed in front of the PC fiber to adjust the polarization of the in-coupled light so that it was aligned to one of the two eigenmode axes. In most cases, no change of the measured linewidth was observed rotating the polarization. This behavior confirmed the low ellipticity of our fiber mirrors, which was also obtained from fiber profiles; see Section 3.2.2. The calculated frequency splitting was below a tenth of the fraction of the cavity linewidth.

Additionally, a Titanium sapphire (Ti:sapph) laser[26] provided us with the possibility to tune the frequency over several free spectral ranges. The entire wavelength range of this Ti:sapph laser of 700–1000 nm allowed us to operate in two different wavelength regions: 800–820 nm was used for the PC fiber LMA-20 and 900–920 nm was necessary for the PC fiber LMA-25, so that the laser light is transmitted; see [134]. Then, both the diode laser beam and the Ti:sapph laser beam were coupled simultaneously into the cavity via a bichromatic mirror suitable for

[26] M Squared SolsTiS narrow linewidth Ti:sapph laser

the wavelength region of the Ti:sapph laser. We tuned the frequency of the Ti:sapph so that its fundamental mode overlaps with the fundamental mode of the diode laser, as seen on the oscilloscope. The absolute frequency of the Ti:sapph laser was then measured using the wavemeter[27] with an uncertainty of around $100\,\mathrm{MHz}$. We continued to tune the Ti:sapph frequency until its fundamental mode aligns once again with the fundamental mode of the diode laser, and again, we record its frequency. This step was repeated multiple times. The difference between these measured absolute frequencies directly gave us the free spectral range, and with Equation (3.2), the cavity length was calculated.

This experimental setup was developed step-by-step during my PhD work. On the one hand, a web-based software for controlling the setup and acquiring data with an automated analysis was developed continuously. On the other hand, several hardware improvements like the stepper motor and the second laser were added year by year to minimize the uncertainties of the measured parameters $\delta\nu$ and ν_{FSR}. Depending on the circumstances of the experimental situation, sometimes specific features of the setup needed to be adapted. For example, if we want to use this method to characterize a fiber cavity after it has been installed inside a vacuum chamber, we need to take into account that the fibers are mounted inside the vacuum chamber on different translation stages than the six-axis positioner. The translation stages in vacuum have no possibility to change the angle, and there is no feedback for the position so that no precise length measurement is available by the stages; more in Subsection 4.5.1. Nevertheless, we were able to use the method above to characterize the fiber cavity, with minor variations, despite all modifications of the experimental setup.

3.3.2 Hybrid fiber-substrate cavity measurements

In 2017, Florian Kranzl investigated single fiber mirrors within the scope of his master's thesis [149], which was supervised by Prof. Tracy Northup, Prof. Rainer Blatt and me. The purpose of his research was to test the theoretical model of transverse-mode coupling in tunable Fabry-Pérot microcavities, as published by Benedikter *et al.* [150], with our fiber mirrors. In particular, we wanted to learn whether this theory could be extended and used to describe our fiber cavities. To minimize the number of unknown parameters, he replaced the out-coupling fiber with a well-characterized highly reflective mirror on a super-polished substrate, as was also done in [150].

In his thesis, the comparison between the measured finesse of the fundamental transversal electro-magnetic (TEM) modes and theory was qualitatively consistent. The comparison of higher-order TEM-modes with theory showed larger discrepancies, especially for certain orientations of the higher modes. Unfortunately, further investigations of this mismatch were not possible within scope of his thesis. One possible explanation was the randomly chosen orientation of TEM modes of the cavity in the simulations. Another potential problem was concerned with the calculation of the theory values. Before the losses are calculated, the geometry of the cavity needs to be known. As the cavity is fully defined by the waist, fit routines are used to find the position, size and orientation of the waist; such a calculation method was provided from [150]. To determine these properties of the waist, the measured profile was fitted multiple times by using a set of initial values. When these initial value were chosen with a too large step size,

[27] High Finesse Wavelength Meter WS-7

artifacts occurred, which were observed as jumps in the calculated losses and therefore in the finesse.

Exactly this step of determining the cavity mode by its waist is even more complicated for a fiber cavity with two fiber mirrors. For the hybrid cavity, the waist is assumed to be at the substrate mirror, and its size and further location is determined only by the position of the fiber mirror. However, this simplification does not hold for a fiber cavity. The position and the orientation of the waist need to be optimized along three axes and two angles so that they fit best to both fiber mirrors. Consequently, the extension of the model of transverse-mode coupling to fiber cavities would need more investigation. Therefore, in this PhD thesis (see Section 7.2), a numerical simulation of a light field between two fiber mirrors was used, which was developed and tested by our collaborators in Paris [115].

The second part of Florian Kranzl's thesis is about birefringence. Again, for the fundamental TEM modes, a prior theoretical model [140] was confirmed. For higher TEM modes, we found that the birefringence follows inverse proportional functions with respect to the cavity length, as in [140], but with exponents about 15–20% higher than that of the fundamental TEM mode. As the theoretical derivation was carried out only for the fundamental mode (see Appendix of [140] which follows the approach of Cullen [151]), it is reasonable to find other formulas for higher TEM modes, which could agree with our measurements. Again, further investigations to carry out the theoretical derivation for higher TEM modes were not possible in the scope of his thesis. Nevertheless, his measurements confirmed not only the theory of Uphoff *et al.*, but also the birefringence observed in measurement of fiber cavities with two fiber mirrors.

During these birefringence measurements, we solved a problem, which was found to occur when the two polarization modes of the cavity were separated at the cavity output by a polarizing beam splitter. Here, Florian observed interferences, as a result of which the linewidth measurements of the cavity resonances in the two polarization channels were disturbed. It was found that a $\lambda/2$-plate between the cavity and the polarizing beam splitter needed to be precisely adjusted to avoid any interferences[149]. In future experiments, a polarization analysis at the output of the birefringent cavity can now be considered correctly.

3.3.3 Fiber cavity with a tilted fiber

In order to understand how we can integrate the fiber cavity with an ion trap, it is crucial to understand the sensitivity of the fiber cavity's alignment. The essential question is whether a translation adjustment in vacuum is enough to align a fiber cavity with a length up to $500\ \mu\mathrm{m}$ or an angle adjustment is necessary, too.

A PC fiber with radius of curvature $R_1 = 295(10)\ \mu\mathrm{m}$ and a MM fiber with $R_2 = 355(5)\ \mu\mathrm{m}$ were chosen to build up a test cavity with a length $L = 540(15)\ \mu\mathrm{m}$. The finesse and the amplitude of the cavity transmission were measured as a function of the tilt angle θ of the MM fiber, while the translation stages were used to optimize for maximal transmission at each measured tilt. The absolute tilt between the fibers was determined by measuring the rotation of the MM fiber in microscope photographs taken for each value of θ.

The finesse was measured to be $54\,000(8\,000)$ for a tilt from $\theta = -2.0°$ to $0.3°$. In Figure 3.12, the finesse and the transmission through the fiber cavity are drawn as a function of the tilt angle. For $\theta > 0.3$, the finesse decreases, as the light mode is pushed to the edge of the mirror with a larger tilt of the fiber. In this case, it is not possible to describe this decreased

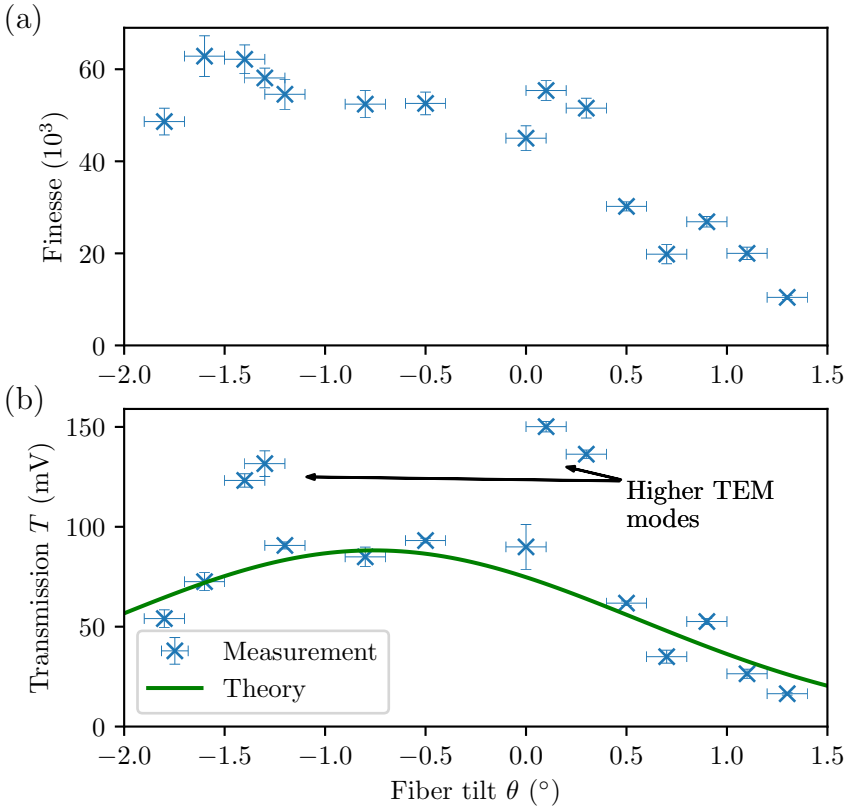

Figure 3.12: (a) Measured finesse as a function of the tilt angle θ between PC and MM fibers. A theory curve was omitted as too many unknown parameters were involved. (b) Measured transmission values as a function of the tilt angle θ, shown as blue crosses. Due to significant discrepancies in finesse and amplitude, we assume that higher TEM modes were measured for $\theta = (-1.4°, -1.3°, 0.1°, 0.3°)$ and exclude these value from the fit to Equation (3.20) (green line).

finesse by analytical formulas because it depends on the effective useful diameter which was not determined for these fibers. For the amplitude T of the transmitted light, unusually high values between 130 and 150 mV were found at tilt angles $\theta = (-1.4°, -1.3°, 0.1°, 0.3°)$. We attribute these four data points to the accidental excitation of higher-order TEM modes. Note that, for cavities with the length $L > R_1, R_2$, the transmission of higher TEM modes can exceed the maximal transmission of the fundamental mode, in particular when the ablated mirror is misaligned with respect to the fiber core.

The coupling between two aligned Gaussian modes is described by Equation (3.9). For a displacement d and an angle θ between the two Gaussian modes, the coupling can be calculated by formulas given in [120]. As the displacement d is optimized for a maximal transmission at each angle θ in our measurements, the measured transmission depends only on the angle θ. Thus, the relative transmission of the cavity can be calculated with

$$T(\theta) = T_{\max} e^{-\left(\frac{\theta-\theta_0}{\theta_e}\right)^2}. \tag{3.20}$$

This theoretical expectation is fitted to the measured data with the maximal amplitude $T_{\max} = 88.2\ \mathrm{mV}$ and the offset $\theta_0 = -0.76°$ as free parameters. In contrast, the width $\theta_e = 1.87°$ was calculated by the formulas given in [120] for the known geometry parameters R_1, R_2 and L which define the Gaussian mode of the fiber cavity. With the four points at $\theta = (-1.4°, -1.3°, 0.1°, 0.3°)$ are excluded, the data along the entire range of the stage, $\theta = -2.0\ °$ to $1.5\ °$, agrees well with the theoretical expectation; see Figure 3.12. $T_{\max}$ was not independently calibrated and therefore is here an arbitrary unit. The shift of the tilt angle θ_0 can be explained by an imperfectly centered mirror with respect to the core of the fiber. Deviations up to $2\ \mu\mathrm{m}$ between the fiber core and ablation minimum have been observed at the CO_2-laser ablation process.

In conclusion, we find that a precision of $\pm 1°$ for the angular alignment of the fibers with respect to each other is necessary to preserve the maximal finesse and transmission. We expect that this precision can be achieved through careful assembly of the fiber cavity and by checking the finesse of the cavity before closing the vacuum chamber. Therefore, we decided to go without including any active angular adjustment in vacuum.

3.3.4 Bend losses of PC fiber

There is a final important property of the fiber mirrors that needs to be considered for the design of the integrated ion trap and vacuum chamber. We have chosen to use the PC fiber, because the mode coupling is enhanced for long fiber cavities. However, PC fibers, with their larger mode field diameters than SM fibers, are more sensitive to losses introduced by bending the fiber. These bend losses are complicated to calculate, as they have an oscillating dependency on the wavelength [152].

Therefore, the transmission of the PC fiber as a function of its bending radius was only measured. An $846\ \mathrm{nm}$ laser was coupled into a PC fiber LMA 20 such that $1\ \mathrm{mW}$ was transmitted through the fiber. Then, the fiber was aligned to circles printed on a piece of paper and fixed with metal posts. The transmitted powers are plotted as a function of the bending radii in Figure 3.13. The critical bending radius is found to be around $50(10)\ \mathrm{mm}$, and no losses were measured for a bending radius $> 65\ \mathrm{mm}$.

Actually, this measurement was carried out after the fabrication of parts for the vacuum chamber, when we recognized that the PC fiber would be too strongly bent in the current design. In a last-minute workaround, we changed the location of the PC fiber within the vacuum chamber: We extended a viewport with a custom-designed T-piece, and we placed the PC fiber in such a way that the fiber was led out via the T-piece with a curvature larger than $65(5)\ \mathrm{mm}$.

Summary

This chapter reported on the fabrication process of fibers including the preparation of the fibers, the CO_2-ablation process, the highly reflective coating of the fibers and the splicing of the PC fibers. The second part of this chapter described methods to characterize the fiber mirrors. Several different properties were analyzed with different measurements of substrate mirrors from the same coating runs, of cavities in different configurations, and of the transmission of PC fibers. The next chapter will now focus on how we integrated our fiber cavity into the

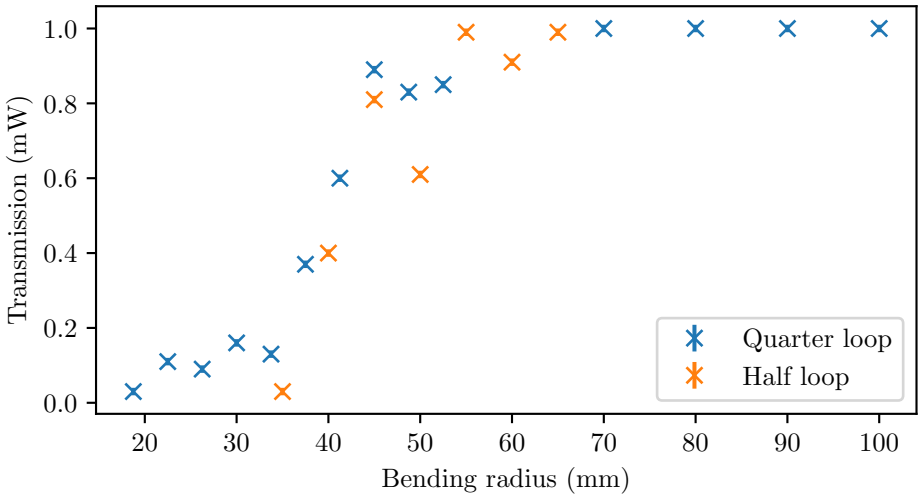

Figure 3.13: Measured transmissions through a LMA 20 PC fiber as a function of the bending radius. The bending radius was aligned for a quarter loop (blue crosses) and for an half loop (orange crosses).

ion-trap system.

Chapter 4

Linear ion trap with a perpendicular fiber cavity

In 2007, Yves Colombe and his colleagues in Jakob Reichel's research group realized strong atom-photon coupling mediated by a fiber cavity [106]. Inspired by this work, in 2009, our research group started a collaboration Prof. Jakob Reichel's research group with the goal of coupling a single ion to a fiber cavity. In the framework of the collaboration, Innsbruck PhD student Birgit Brandstätter, with the help and support of Reichel's group, laser-machined a first batch of optical fiber cavities in Paris, which afterwards were sputtered with an ultra-low-loss commercial mirror coating. Birgit finished her PhD thesis with an operating linear ion trap and a fiber cavity in vacuum space [83]. Unfortunately, it was not possible to couple an ion to the cavity field, so further development of the cavity-trap system was necessary.

This chapter describes our experimental setup of an ion trap with an integrated fiber cavity. First, we discuss how and why we modified Birgit's prior design. In Section 4.2, the simulations of the ion trap's potential is analyzed. Then, the ion trap is characterized without the influence of the fibers. The second main characterization of the experiment, the fiber cavity, is measured and analyzed in vacuum (Section 4.5). Last, we describe how we were able to manipulate charges on the fibers in vacuum.

4.1 Design of the cavity-trap system

In 2013, two independent experiments in the research groups of Profs. Köhl and Keller succeeded in coupling an ion to a fiber cavity [108] [153]. However, in both experiments, the ion was stored in a point-like ion trap. These ion-trap configurations mean that quantum information processing with multiple ions in the same trap via a phononic link [27] is restricted by the micromotion as only one ion can be stored in such a trap without micromotion. In contrast to these experiments, starting with Birgit Brandstätter's PhD project, we have aimed to integrate a fiber cavity into a linear ion trap, an established trap design for quantum information processing with multiple ions.

4.1.1 Idea and motivation

Since 2001, linear ion traps have been used to perform quantum gate operations on multiple ions in Innsbruck [154]. The initial ion trap design with four RF electrodes and two ring endcaps was then further developed into a trap consisting of four RF blades and two endcaps [155]. This later trap configuration is nowadays known as the "Innsbruck-style" ion trap and has been adopted for quantum sensing [156], computing [155], simulation [157], and communication [81]. As the experimental apparatus with substrate mirrors integrated into a linear ion trap has successfully been used to carry out several proof-of-principle quantum communication experiments [82, 158], we wanted to adopt such an approved design with the fiber cavity axis perpendicular to the axis of the linear ion trap. The alternative approach, to align the cavity axis parallel to the trap axis, seemed incompatible with a fiber cavity, as the endcaps are separated by several millimeters, which exceeds the target length of our fiber cavity by one order of magnitude.

Furthermore, the design of a cavity perpendicular to the trap axis allows ions to be shuttled into and out of the cavity light field. In micro-fabricated ion traps, such shuttling could be the basis for a specialized networking zone in quantum charged-coupled devices [33].

4.1.2 Previous design

The setup from 2009-2014 was designed and built by Birgit Brandstätter to integrate a fiber cavity with limited length up to $350\ \mu\mathrm{m}$ [124]. With this limitation on the cavity length, not only was the "Innsbruck-style" ion trap miniaturized but also the angles between the blades were changed to an asymmetric configuration of $60°/120°$. In Figure 4.1(a), a photograph of the former experiment shows the ion trap with its axis horizontally aligned and the fiber cavity mounted on two nanopositioners from top and bottom. The larger angles opened up the possibility to integrate a fiber cavity with shorter length while the ion-blade distance of $170\ \mu\mathrm{m}$ was kept the same compared to the symmetric case. However, it turned out that this blade configuration has the following three drawbacks.

As simulated by Birgit, the compensation electrodes between the blades with the $60°$ angle had a reduced influence on the ion compared to the $90°$ case. In the experiment, this reduced influence of the compensation electrode needed to be circumvented by using one ground blade as the compensation electrode.

Another drawback was that the asymmetric blade design lifted the degeneracy of the radial confinement along the horizontal axis which lies in the plane of the main optical axis. In order to cool all trap axes of the ion, additional strategies would be needed such as cooling beams from two directions or additional, radial, electric DC fields.

In contrast to the other two drawbacks, we were not able to avoid the following third consequence of the asymmetric blade configuration. As we increased the axial confinement, the radial confinement was reduced as expected by Equation (2.6). Due to the asymmetric shape of the trap, the radial confinement was non degenerated, and was reduced asymmetrically such that the radial axis perpendicular to the fiber cavity axis was weakened significantly more than the other radial axis; see Figure 4.1(b). If we want to achieve an axial confinement of $\omega_{\mathrm{ax}} = 2\pi \cdot 1.25\ \mathrm{MHz}$ with a radial confinement with secular trap frequency $\omega_{\mathrm{rad}} = 2\pi \cdot 4.26\ \mathrm{MHz}$, we need to apply $3\ \mathrm{kV}$ on the endcaps. However, the ion's potential would result in a double-well confinement along the radial axis perpendicular to the cavity axis; see Figure 4.1(c). A stronger radial

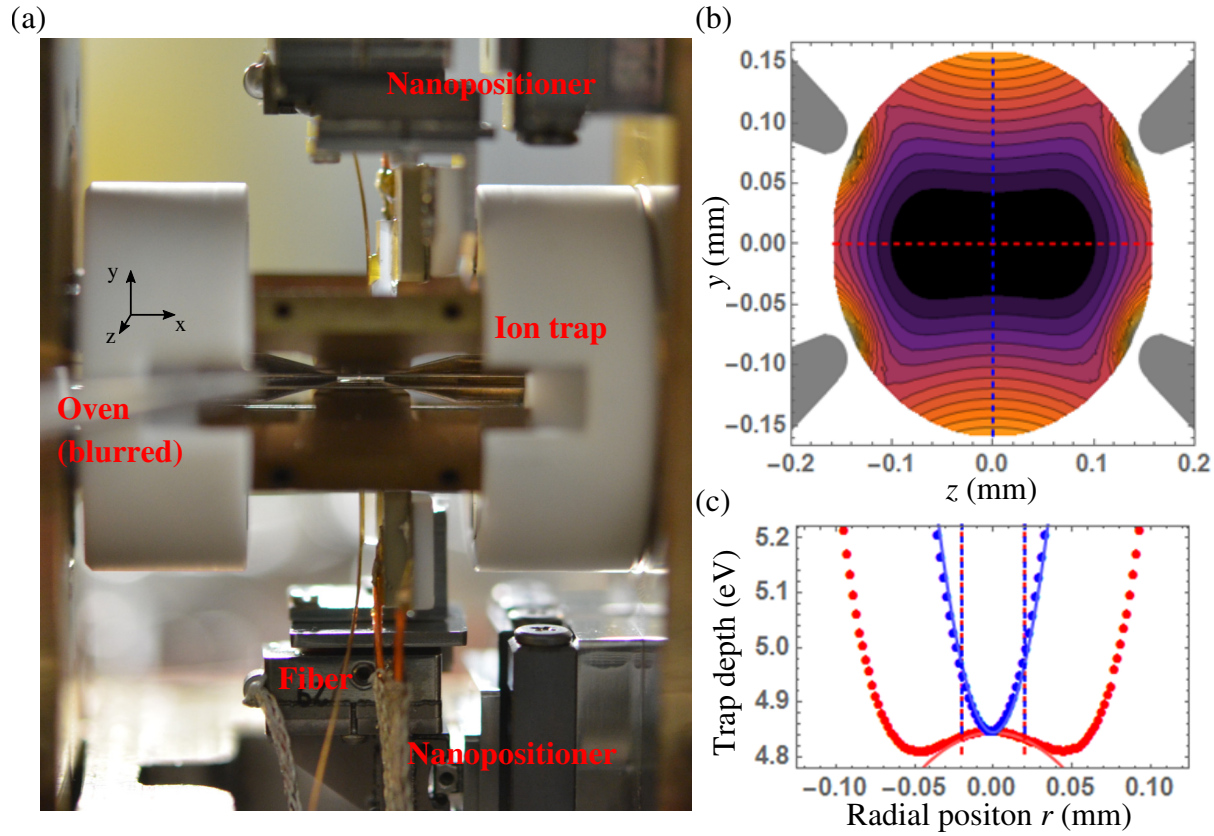

Figure 4.1: (a) Photograph of previous ion-trap fiber-cavity setup from a view perpendicular to the trap axis and optical axis of the fiber cavity. (b) Simulated radial trap potential drawn as black for the minimum to light red for the maximum. The blades (gray parts) are arranged around the center of the trap at $y = z = 0\,\mathrm{mm}$ with an enlarged distance along z-axis. (c) Two cuts through of the trap potential are plotted as a function of the radial positions r. The blue points (marked as a dashed blue line in (b)) follow the harmonic potential (blue solid line) forming a confinement of the ion along the y-axis. The red points (dashed red line in (b)) show a double well potential. The solid red line is a harmonic fit to points close to the center which illustrates the anti confinement at the center.

confinement could overcome this double-well potential, but for $\omega_{\mathrm{rad}} = 2\pi \cdot 4.26\ \mathrm{MHz}$, the q-parameter is already $q = 0.4$ which should be kept low around $q = 0.3$; see Section 2.1.

With this limited axial confinement, we were not able to store the ions at the trap center, while the fibers are close to the ions. The fibers were mostly positively charged, and therefore, they pushed the ions out of the cavity. To overcome this limitation, Prof. Tracy Northup, our postdoc Florian Ong, and I planned a new miniaturized but symmetric "Innsbruck-style" ion trap in 2013. In contrast to 2009, we thought fiber cavities with a length up to $500\ \mu\mathrm{m}$ are possible with the new CO_2-laser setup in Paris. This assumption was later confirmed, as introduced in Chapter 3 and measured later in this chapter.

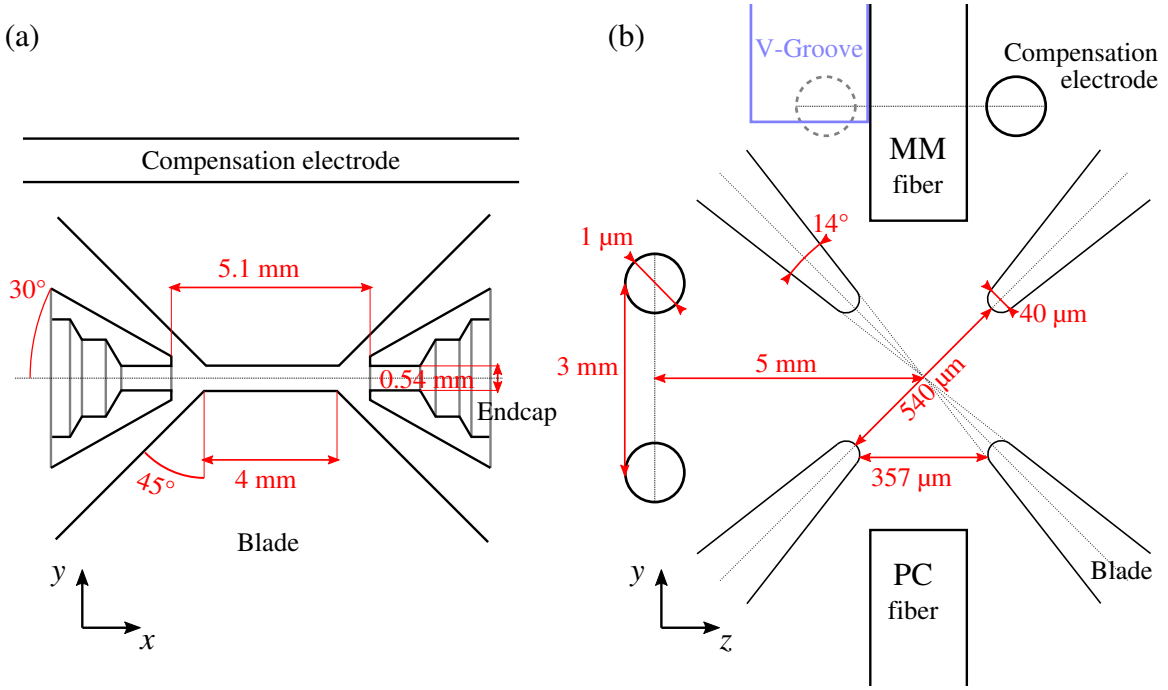

Figure 4.2: (a) Schematics of the ion-trap design in a plane including the trap axis with cuts through the endcaps. Only the vertical compensation electrode is drawn. (b) Schematics of the radial ion-trap geometry. The compensation electrodes are not to scale.

4.1.3 Blueprints of the cavity-trap system

We took the most recent "Innsbruck-style" linear ion trap [156] and reduced the size of the radial-electrode-to-ion distance from $555\ \mu\mathrm{m}$ to $270\ \mu\mathrm{m}$. The radius of curvature at the end of the blades was adjusted from $135\ \mu\mathrm{m}$ to $20\ \mu\mathrm{m}$. Furthermore, the length of the blades along the trap axis x needed to be shortened from $4.5\ \mathrm{mm}$ to $4\ \mathrm{mm}$, such that the blades were still stable enough for machining. These blades led us to an endcap-to-endcap distance of $5.1\ \mathrm{mm}$; see Figure 4.2. The endcaps were adopted from the original design in [156] without any changes, meaning that they have the same holes with a diameter of $540\ \mu\mathrm{m}$ for optical access along the trap axis. The y-axis and the z-axis are in the radial plane, whereby the y-axis is oriented vertically, and the z-axis is in the horizontal plane; see Figure 4.2. The trap center is the origin of this coordinate system with $x = y = z = 0$. The compensation electrodes were also adopted from [156]. In the horizontal direction, the compensation electrode consists of two rods each at a diameter of $1\,\mathrm{mm}$ and with a distance of $3\,\mathrm{mm}$ from each other. The midpoint between these two rods has a distance of $5\,\mathrm{mm}$ from the trap center; see Figure 4.2 (b). In the vertical direction, only one rod acts as the compensation electrode as the second rod was left out to give space for the MM fiber mounted on a V-Groove.

Each fiber mirror of the cavity is movable by an individual nanopositioner with slip-stick piezos for all three directions[1]. The fibers are mounted on the nanopositioners via a stack of a Pyrex V-groove, a shear-mode piezoelectric actuator (shear piezo) and a MACOR spacer, as it

[1] Assemblies of SmarAct SL-0610-UHVT stages for the x-axis and z-axis and a SLC-1720-UHVT stage for the y-axis

was done by Birgit in [83]. The shear piezos are necessary for the cavity length stabilization because the nanopositioners are too slow. Along the y-axis, a PC fiber mirror is inserted by moving the nanopositioner upwards; see Figure 4.2(b). Translating a MM fiber mirror from the top, a fiber cavity with our target cavity length of 400–500 µm (Section 3.1) can be aligned.

4.1.4 Expected challenges

At the beginning of designing the new cavity-trap system in 2013, the first challenge was to fabricate new fiber mirrors with possible cavity lengths up to 500 µm, see Section 3.1. Later, with the improved CO_2-laser setup, we fabricated (Section 3.2) new fiber mirrors in 2014 and 2015. After the first measurements (Subsection 4.5.1), we confirmed our expectations, and fulfilled the requirements for a fiber cavity with the ion trap we designed.

A less predictable challenge was the influence on the ion-trap potential of charges on fibers. In the previous experimental apparatus of Birgit, charges on the fibers kept us from trapping ions inside the fiber cavity, as discussed in Subsection 4.1.2. Four points let us think charge related issues could be resolved in the new setup.

First, the symmetric blade configuration of the new setup avoided the most important drawback of the previous setup (Subsection 4.1.2): the double-well potential in the radial direction for stronger axial confinements. A stronger axial confinement should then allow us to keep the ions at the trap center even for charged fibers.

Second, the fibers were now inserted between blades with an angle of $90°$ instead of $120°$ as in the previous setup. As we had seen that the influence of the compensation electrodes depends on the angle of the blades, we concluded that the rectangular design will shield trapped ions from charges on the fibers better than the previous design.

Third, the size of the cavity-trap system was almost doubled. Not only was the ion-electron distance almost doubled from 170 µm to 270 µm, but also each fiber would be 250 µm apart from the ion.

Fourth, we thought we were using the experience of another project of our research group. Our colleague Ben Ames tried to approach a tapered fiber with a 500-nm waist (nanofiber) to a trapped ion. In the scope of this PhD work, he developed a method to discharge the nanofiber inside the vacuum chamber at this time. Later, he trapped an ion at a distance of only 25 µm from the fiber, that is, a factor of ten times smaller than needed in our design [159].

4.2 Trap simulations with fibers

Before the trap was fabricated, simulations of our design were carried out to predict the characteristics of the trap with the fibers inserted. Not only charges on the fiber surfaces (Subsection 4.1.4), but also the dielectric material of the fibers and their mirror coating will alter the potential seen by the ion. After the methods of these simulation are explained in Subsection 4.2.1, the consequences for the trap depth and secular trap frequencies are studied in Subsection 4.2.2,

4.2.1 Simulation method

The simulations are carried out in two steps: First the total potential is calculated from the geometry of our trap and fibers. In a second step, characteristics of the ion trap are deduced from the total potential.

The total potential is the sum of the RF pseudopotential [59] and the static potentials generated by the endcap and compensation electrodes. The performance of the compensation electrodes were investigated in separate simulations. These simulations showed a shift of $14\ \mathrm{nm/V}$ and $38\ \mathrm{nm/V}$ of the ion for the two compensation electrodes along the z-axis and for the one compensation electrode along the y-axis respectively. No significant crosstalk ($< 1\ \mathrm{nm/V}$) was found for both compensation directions. For the following analysis, the compensation electrodes were grounded for all simulations.

We use finite element analysis software[2] to simulate the relevant electrostatic potentials. The simulations take into account the modification of the RF potential by the fibers by treating the fibers as dielectrics. The simulated fibers are assigned a dielectric coefficient at RF equal to that of silica, and with a length of $6\ \mathrm{mm}$.

We first simulate the static electric potential $U_{\mathrm{RF}}(\vec{r})$ generated by the voltage $V_0 = 1\,\mathrm{V}$ applied to a pair of radial RF electrodes while all other electrodes are grounded. The RF pseudopotential is then given by

$$\Phi_{\mathrm{RF}}(\vec{r}) \;=\; \frac{Q^2}{4M\Omega^2}\left(\frac{V_{\mathrm{RF}}}{V_0}\right)^2 \vec{\nabla}^2 U_{\mathrm{RF}}(\vec{r}),$$

where M is the mass of a $^{40}\mathrm{Ca}^+$ ion, Q is the elementary charge e, and Ω and V_{RF} are the angular frequency and amplitude of the voltage applied to the RF electrodes. Next, the potential energy due to the right or left endcap electrode $i \in \{R, L\}$, when biased by a DC voltage $V_{\mathrm{ec},i}$, is given by

$$\Phi_{\mathrm{ec},i}(\vec{r}) \;=\; Q\left(\frac{V_{\mathrm{ec},i}}{V_0}\right) U_{\mathrm{ec},i}(\vec{r}),$$

where $U_{\mathrm{ec},i}(\vec{r})$ is the simulated electric potential generated when the voltage $V_0 = 1\ \mathrm{V}$ is applied to the endcap i and all other electrodes are grounded. Finally, the total potential energy $\Phi_{\mathrm{sim}}(\vec{r})$ is given by

$$\Phi_{\mathrm{sim}}(\vec{r}) = \Phi_{\mathrm{RF}}(\vec{r}) + \sum_{i=\mathrm{R,L}} \Phi_{\mathrm{ec},i}(\vec{r}) \tag{4.1}$$

[2] COMSOL Multiphysics, AC/DC Module

For each experimental configuration of fiber cavity length $L = d_{\mathrm{M}} + d_{\mathrm{P}}$, we successively simulate $U_{\mathrm{RF}}(\vec{r})$ and $U_{\mathrm{ec},i}(\vec{r})$, and we export a two-dimensional map of the corresponding electrical potentials in the radial plane at the center of the trap. In separate post-processing software, we build the total potential $\Phi_{\mathrm{sim}}(y, z)$ by summing the different contributions scaled by the voltages applied to the trap.

From this total potential, the post-processing software determines the potential's minimum, which is also the position of a trapped ion. At this minimum, one-dimensional cuts of the potential in different directions are fitted by harmonic potentials

$$\Phi_{\mathrm{harm}}(r) = \frac{1}{2} M\omega^2 r^2, \tag{4.2}$$

from which the ion's secular frequency ω in the trap is extracted.

4.2.2 Study of radial potentials with fibers

The total potential corresponding our trap design with fibers was calculated for an RF amplitude $V_{\mathrm{RF}} = 200\ \mathrm{V_{pp}}$ and an angular frequency of $\Omega = 2\pi \cdot 30\ \mathrm{MHz}$. Two-dimensional potential landscapes for bare fibers and fibers with a metal-coated side are plotted for a cavity length of $0.5\ \mathrm{mm}$ in Figures 4.3(a) and (b), respectively. From these simulated potentials, the expected secular frequencies of the ion were determined along the z-axis (red dashed line) and the y-axis (blue dashed line).

As the fibers are mounted on translation stages, the simulations were carried out for different fiber positions forming fiber cavities with lengths L ranging from 0.1 to $1\ \mathrm{mm}$, symmetric around the trap center. The simulated trap depths and radial secular frequencies along the y- and z-axes are shown for these different cavity lengths in Figures 4.3(c) and (d), respectively.

For the bare fibers, the trap depth along the z-axis is constant at $1\ \mathrm{eV}$. Along the y-axis, which is parallel to the fibers, the trap depth decreases for cavities smaller than $0.6\ \mathrm{mm}$. For our planned fiber cavity geometry with $L = 500\ \mu\mathrm{m}$, it is still around $0.8\ \mathrm{eV}$. However, for cavities with $L < 0.3\ \mathrm{mm}$, the trap depth is only around $0.3\ \mathrm{eV}$, which is still possible to work with but is already as low as for surface ion traps [160]. Secular trap frequencies along both axes are around $4\ \mathrm{MHz}$ when the fibers are retracted. When the fibers form a short cavity of $0.1\ \mathrm{mm}$, both trap frequencies are lowered to around $3\ \mathrm{MHz}$. All these parameters indicated possible stable trapping with the desired characteristics of a linear ion trap [155].

For fibers with a metal coating on their sides, the trap depth is again constant at $\sim 1\ \mathrm{eV}$ along the z-axis with an increase up to $1.06\ \mathrm{eV}$ for short cavities. For the y-axis, we first find an increased depth up to $1.1\ \mathrm{eV}$ at $0.5\ \mathrm{mm}$. However, approaching shorter cavities, the trap depth drops to only $50\ \mathrm{meV}$. Again, the secular trap frequencies are in the range of 3–4 MHz, whereby the y-axis shows a peak of $6\ \mathrm{MHz}$ at $0.2\ \mathrm{mm}$. From these simulations, we might think that metal-coated fibers could be an alternative to the uncoated fibers.

Later thoughts led to the conclusion that the ion trap would not have a linear axis if metal-coated fibers are inserted. The metal coating would correspond to additional electrodes in the ion-trap geometry with an axial distance of $d_{\mathrm{ax}} < 150\,\mu\mathrm{m}$. Consequently, the residual RF-field along the trap axis could not be neglected, as the assumption of the ion position $|x| \ll d_{\mathrm{ax}}$ is not fulfilled for multiple ions with positions $|x| > 5\ \mu\mathrm{m}$; see Subsection 2.1.1. The characteristics of a linear ion trap would not be preserved with metal coated fibers between the

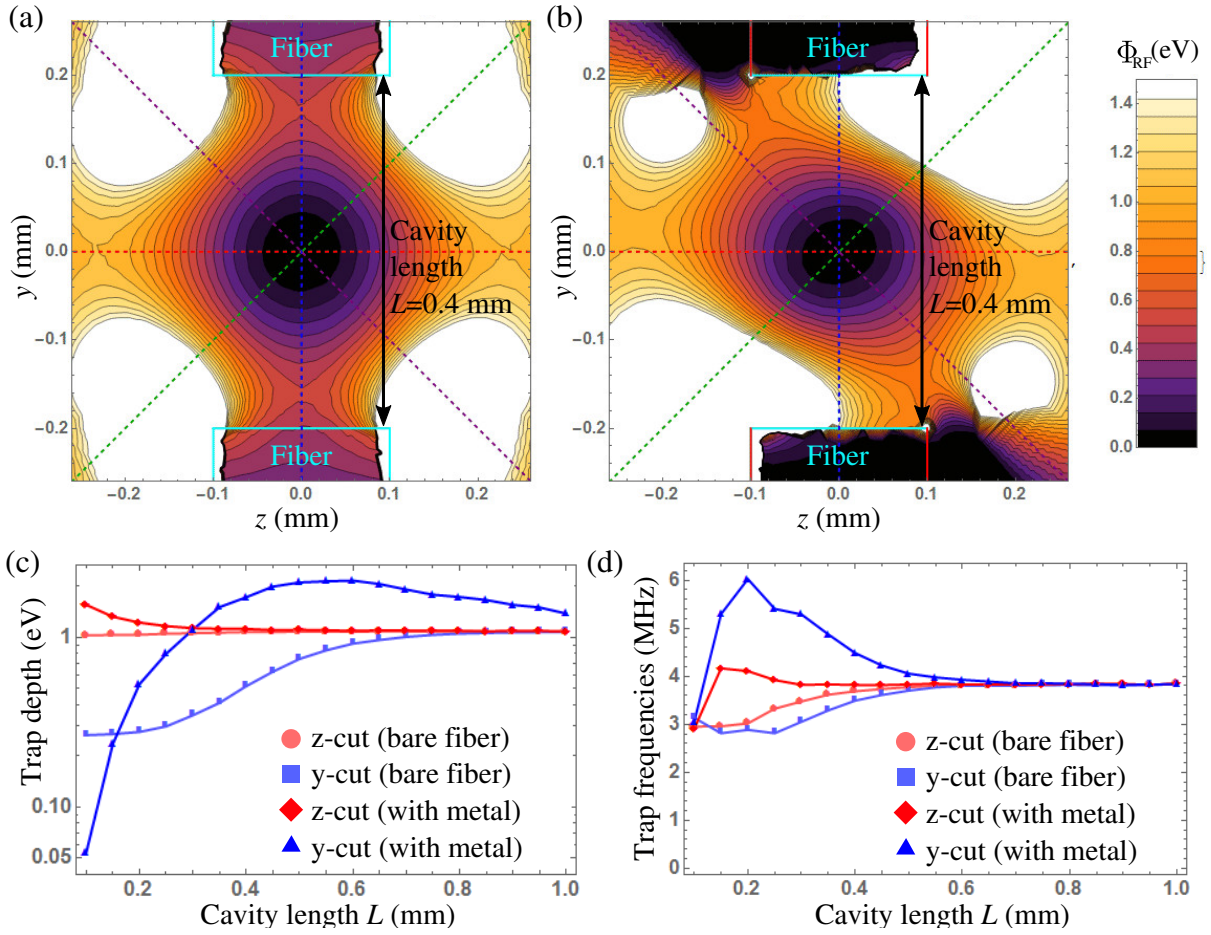

Figure 4.3: (a) Simulated radial potential of the ion trap for a fiber cavity with 400 µm length. (b) Same as (a) but with metal coatings on fiber sides. (c) Trap depth and (d) radial secular frequencies as a function of the cavity length L.

blades. Furthermore, the cavity field cannot be aligned with respect to the ion by moving the cavity mirrors, as a movement of the metal-coated fiber corresponds to a change of the trap geometry such that the ion's position is also altered. Researchers in Sussex faced exactly this problem, and they needed a couple of additional RF electrodes to align the RF-field for a single ion [111].

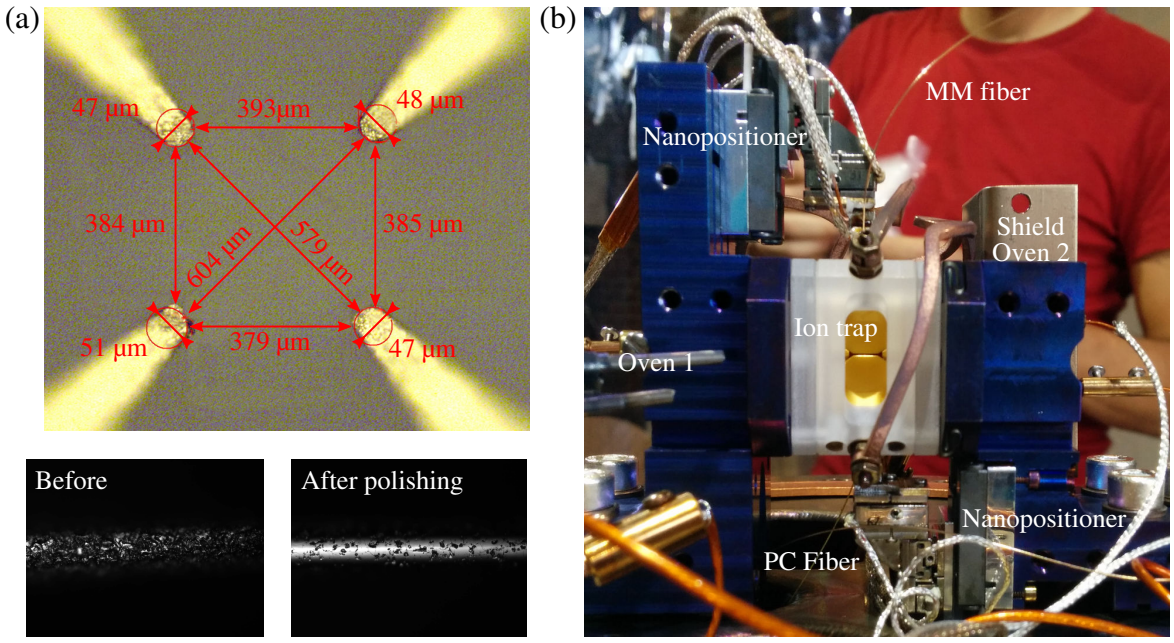

Figure 4.4: (a) Photo of the radial ion-trap alignment, with measured blade-to-blade distances indicated. Microscope photos with a magnification of 50 from before and after polishing are shown in the lower part. (b) Photo of the ion-trap assembly with fiber mirrors mounted on the nanopositioners.

4.3 Assembly of the system

After the simulation confirmed the function of our design of the ion trap, the titanium trap electrodes were machined by Stefan Haslwanter[3], and gold-plated by Kirill Lakhmanskiy[4] in our laboratories. Before the gold plating, Kirill and I polished the end of the blades to reduce the surface roughness closest to the ions; see lower part of Figure 4.4 (a). A test assembly consisting of the gold-plated titanium blades mounted into a sapphire holder was measured by a length-calibrated microscope; see upper part of Figure 4.4(a). We found a mean lateral distance between the blades of 385(5) µm, whereas the length in our design was 357 µm. The diagonal distances were determined to have a mean value of 590(15) µm, and the diameter of the curvature at the end of the blades was found to be 48(2) µm. These measurements showed that the fabrication tolerances of the wire-cut electrical discharging machining were about 10–20 µm[5]. These tolerances result in relative deviations of 5% for the blade alignment and 20% of the radius of curvature at the end of the blades. The distance between the endcaps was later measured with a camera used for the ion detection. We found a distance of 5.3(1) mm, which again differs only by about 5%.

In summer 2015, the entire system was assembled and the fiber cavity was merged with the ion trap inside the vacuum chamber — the wedding of the cavity with the trap. We recycled

[3]Mechanical workshop at the Institute for Quantum Optics and Quantum Information in Innsbruck
[4]PhD student in our research group
[5]Thanks to Stefan Haslwanter for this precise work.

the experimental setup of Birgit [83]. This means that we exchanged the top flange on which the trap was mounted with all electrical connections. The construction of the new setup was similar to Birgit's previous version; compare Figure 4.4 (b) with Figure 4.1 (a). The same two nanopositioning stages as in Birgit's setup were mounted below and above the ion trap. We installed a home-made calcium oven identically to Birgit's setup, and a second commercial calcium[6] oven was installed $20\,\mathrm{cm}$ apart on a flange; see [161], but without a movable bellows flange. To reduce the calcium deposits on the trap form the commercial oven, a metal shield with a small aperture was mounted in front of the ion trap. The fibers were glued onto the V-Grooves and into the home-made fiber feedthrough [83] with an ultra-violet light curable glue[7].

Afterwards the vacuum chamber was baked out for twelve days at $130°\mathrm{C}$. An unexplained vacuum pressure rise from $10^{-9}\ \mathrm{mbar}$ to $10^{-7}\ \mathrm{mbar}$ for four hours was the reason to stop the bake-out. After the vacuum chamber was cooled down while it was still connected to the turbo pump, the pressure in the vacuum chamber was $5.7 \cdot 10^{-9}\ \mathrm{mbar}$. As the pressure already settled for three days at this value, we haven't continue the bake-out. One hypothesis for the sudden pressure rise is that the glue at the fiber feedthrough maybe have become leaky at $130\,°\mathrm{C}$, and closed itself at the cooldown.

After activating the ion pump and titanium sublimation pump, and disconnecting the chamber from the turbo pump, the pressure was up to $1.5 \cdot 10^{-9}$ in summer and down to $4 \cdot 10^{-10}\ \mathrm{mbar}$ in winter, depending on the temperature in the lab. To find the reason for the high pressure, we tried several leak tests without any success. Mass spectrometer measurements also indicated that there was something outgassing inside the vacuum. We suspected a residual acrylate coating below the polyimide coating of the fiber, but a vacuum test with such a coating configuration showed ultra-high vacuum below $4.5 \cdot 10^{-11}\ \mathrm{mbar}$.

We believe that our vacuum pressure explains why we were never able to trap ions for longer than tens of minutes, as the ions were kicked out of the trap or formed molecules which occur as dark ions by collisions with the residual background gas. We thought about photodissociation to split the hydrogen, oxygen, or water molecules form the calcium ions [162–165]. However, we continued without any further attempts to lower the pressure in the chamber as a lot of experiments were still possible with ion lifetimes of several minutes.

[6] Alvatec
[7] Dymax OP-67-LS

4.4 Ion trap characterization

After the assembly and bake-out, the vacuum chamber was transferred to our optical table, and all electronics and optics were installed, similar to the previous setup of Birgit [83],

4.4.1 Micromotion compensation

After trapping ions for the first time with the fibers maximally retracted (distance > 1 mm, we started with a rough method to compensate for the micromotion of the ion [166]. A rough method for micromotion compensation is to vary the RF amplitude. For a high RF amplitude, the ion follows the RF potential, but for low RF amplitude, the ion is shifted by any DC stray fields. By using the CCD camera field as a reference frame, the ion position at low RF amplitude can be overlapped with the position at high amplitude by means of the compensation electrodes. A similar but less precise technique can be implemented for micromotion compensation along the camera direction by overlapping the foci at which the ion is imaged for different RF amplitudes.

We considered different possible methods [167, 168] and we decided to compensate for the ion's micromotion by measuring the amplitude of scattered fluorescence, which is correlated with the phase of the RF drive field in the event of micromotion [166]. With a time-tagger and a time-to-digital converter counter box[8]we detected the ion's fluorescence triggered by the phase of the RF field. A histogram with 370 time bins of 162 ps was filled by averaging over a couple of seconds. With the minimum $R_{\min}$, the maximum $R_{\max}$ and the difference $\Delta R = R_{\max} - R_{\min}$, the modulation of this histogram $\Delta R/R_{\max}$ is plotted in Figure 4.5 as a function of the voltages applied to the compensation electrodes. In the measurements corresponding to the data shown in Figure 4.5 (a), the ion was shifted by a voltage applied to the horizontal compensation electrode and the ion was illuminated by the 397 nm beam along $\hat{x} + \hat{z}$; see Figure 4.2. For the measurement in the vertical direction (Figure 4.5(b)) another 397 nm beam in the x-y plane with a $30°$ angle to the vertical y-axis was used.

By fitting hyperbolic curves to the data in Figure 4.5, the minimal modulation was found to be at $V_{\mathrm{h}} = 52$ V and $V_{\mathrm{v}} = 147$ V. The residual modulation can be explained by an AC field along the trap axis, as the ion's micromotion was not optimized along x-axis. Furthermore, perturbations due to phase shifts from the trap drive or stray fields on nearby electrodes are possible. Nevertheless, these results confirmed the function of the two compensation electrodes in both directions with only a factor of two difference, as predicted by our simulations, but in contrast to Birgit's simulations (Subsection 4.1.2). More precise micromotion compensation techniques such as resolved sideband measurements with 729 nm [169] were skipped at this time, as we expected that the translation of the fibers would change the stray fields again.

4.4.2 Secular frequency measurements

To determine the secular trap frequencies, an extra AC "tickling" voltage is applied to the trap electrodes. For the radial direction, this voltage is applied to the vertical compensation electrode, and for the axial direction, to the left endcap in a bias tee configuration, so that simultaneously a DC voltage on the endcaps can build up an axial confinement. For frequencies of this

[8]QuTAU from QuTools,

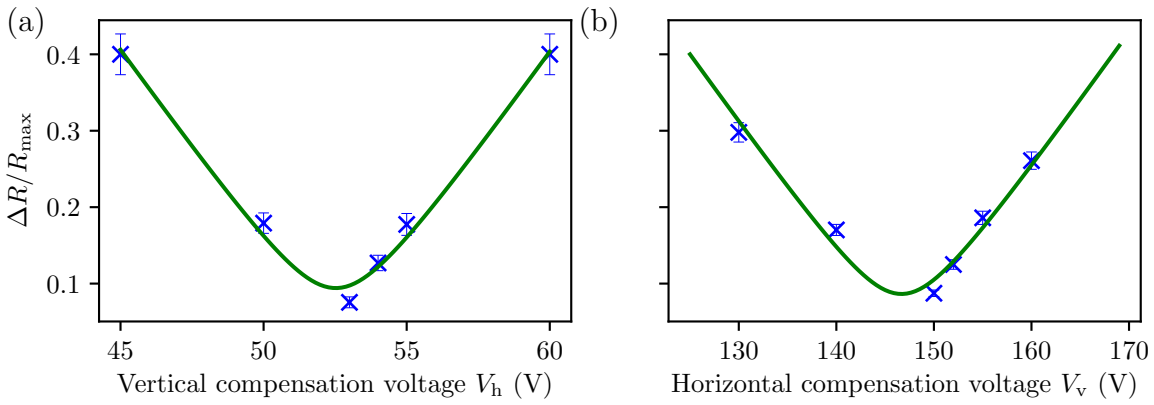

Figure 4.5: The modulation $\Delta R/R_{\max}$ of the ion's fluorescence when it is correlated with the trap drive plotted against (a) the radial horizontal compensation voltage V_{h}, and (b) the radial vertical compensation voltage V_{v}. Each data set is fitted with a hyperbolic curve to determine the voltage with the minimal micromotion.

tickling voltage near the secular resonances, the ion's motion is excited, and a blurred image of the ion is detected on the camera [170].

The secular trap frequency in the axial direction ω_{ax} was measured for different mean endcap voltages $V_{\mathrm{ec,m}} = (V_{\mathrm{ec,L}}+V_{\mathrm{ec,R}})/2 = V_{\mathrm{ec,R}} = V_{\mathrm{ec,L}}$, where $V_{\mathrm{ec,L}}$ and $V_{\mathrm{ec,R}}$ are the voltages applied to the left and right endcaps, which in this case were equal to one another; see the blue points in Figure 4.6(a). This data can be fitted by the formula

$$w_{\mathrm{ax}} = \sqrt{\alpha V_{\mathrm{ec,m}} + w_0^2}. \tag{4.3}$$

From this fit, the factor α, which accounts for the geometry of the trap, was determined. The geometric factor determined from the measurements is given by $\alpha_{\mathrm{exp}} = 2.3(1)\,\mathrm{kHz}^2/\mathrm{mV}$. However, a significantly different factor $\alpha_{\mathrm{sim}} = 1.6(1)\,\mathrm{kHz}^2/\mathrm{mV}$ was extracted from a simulation of the axial trapping potential, as shown with red crosses in Figure 4.6(b). We attempted to explain this discrepancy as being due to the imprecise knowledge of our axial geometry. However, the weaker confinement in the simulations could not be explained by the axial geometry, as the length of the blades and the distance between the endcaps were confirmed by measurements with the CCD camera.

Only uncertainties in the radial positions of the blades can generate an axial confinement in the simulation consistent with that observed in the measurements. Therefore, we carried out further simulations (see red triangles in Figure 4.6(b)) in which the radial ion-electrode distance was increased by 13 µm (a 5% increase with respect to the design value) and 26 µm (a 10% increase). Here, the fits yield geometric factors of $\alpha_{\mathrm{sim},5} = 2.0(1)\,\mathrm{kHz}^2/\mathrm{mV}$ and $\alpha_{\mathrm{sim},10} = 2.6(1)\,\mathrm{kHz}^2/\mathrm{mV}$, respectively. We see that increasing the blade separation by around 7% ($\approx$ 20 µm blade displacement) reproduces the measured data. Such displacements were observed in the test assembly in Figure 4.2(c). As we cannot determine the radial positions of the blades with uncertainties less than 20 µm in the assembled ion trap, we scale the voltages applied to the endcaps in our simulations to achieve the measured secular trap frequencies.

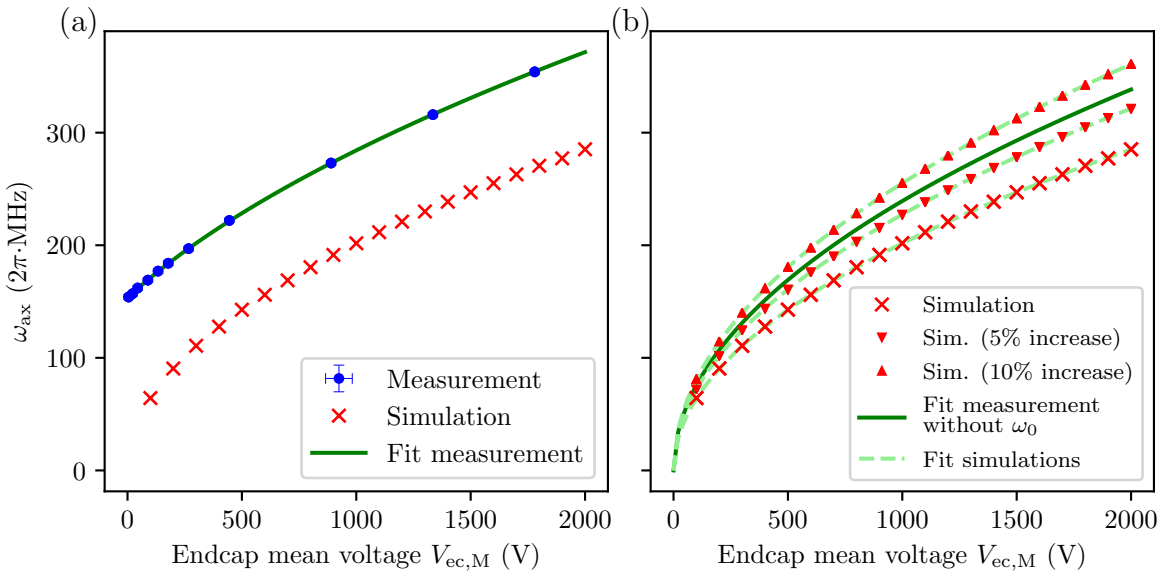

Figure 4.6: (a) Axial trap frequency as a function of the mean endcap voltage. Measured data (blue points) and simulated data (red crosses) are significantly different. The error bars of the measurement are smaller than the symbols. The green line is the fit of Equation (4.3) to the measured data. The different offset can be explained by a patch potential; more details are given in Section 6.4. (b) Again, the simulated data is plotted as red crosses. To compare it with the measurement, the fit of the measurement is plotted as a green solid line without the offset ω_0. Additionally, the red triangles are simulations for trap geometries with a radial enlargement of 5% and 10%, which can explain the difference in the geometric factors α extracted from measured data and simulations. Green dashed lines are fits to the simulations.

The theory of our linear trap design does not include the additional confinement ω_0 in the expression above for ω_{ax} [56]. However, in order to achieve agreement with our measurements, it was necessary to include a positive value for w_0^2. The corresponding confinement was found to be independent of the applied RF voltage in our experiment. Such a residual static potential is common in ion traps [112]; in our case, it is likely due to deposits of atomic calcium that have built up on radial electrodes after repeated loading of ions [171]. If there are calcium patches, then they deform the trapping potential and may additionally oxidize and subsequently trap charges, thus contributing to the total electric potential [172, 173]. In our case, the precise origins, locations, and shapes of these patches are unknown. We heated the radial trap electrodes locally with strong laser light [155] with powers up to 15 W. After this treatment, we observed a different confinement ω_0. We inferred that we are able to manipulate these patches, but this method does not allow us to control the patches precisely or to eliminate them.

In the radial plane, the secular frequency was measured along the y-axis while the power of the trap drive was tuned. At the same time, a calibrated pick-off was used to measure the amplitude of the applied RF field. The secular radial trap frequency was thus determined in relation to the RF amplitude; see the blue points in Figure 4.7. The relationship of the trap to the RF amplitude was also simulated as described in Section 4.2.1 and is plotted as red crosses in Figure 4.7. As shown in Subsection 2.1.1, we expect the radial trap frequency to be described by the Equation (2.6). With the trap frequency $\Omega_{RF} = 2\pi \cdot 30.27$ MHz, the fits of the measured

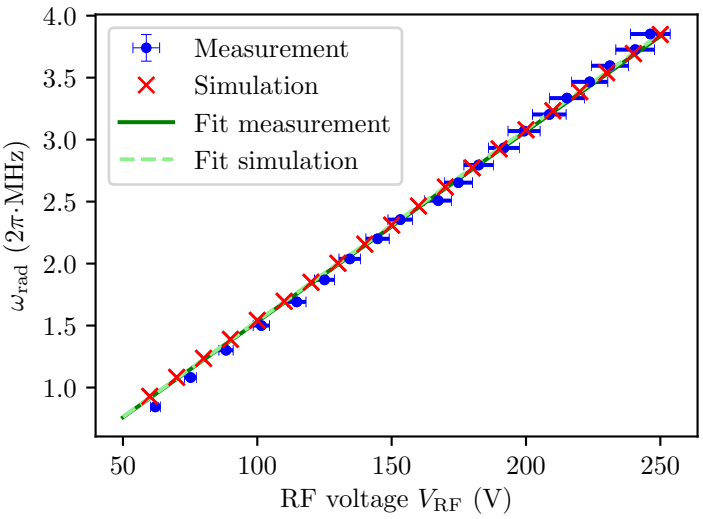

Figure 4.7: Radial trap frequency as a function of the RF voltage. Measured data (blue points) and simulated data (red crosses) are in agreement, which can be seen from the overlap of their fits (green lines).

and simulated data yield a radial trap geometry factor of $\eta' = 0.02$. Both fits lie within the error bars of the measurement, so that we can confirm the agreement between simulation and measurement.

4.4.3 Further ion-trap characterization

So far, only classical properties of our ion trap were characterized. Usually, for our research group, the quantum properties of the ion trap are of greater interest [174]. The two most important parameters are the coherences of the qubit itself of and the ion's motion.

As introduced in Section 2.1.2, via sideband cooling, the ion can be cooled down to it's motional ground state. The first characteristics to be determined is the heating rate by measuring the blue and red sidebands after a varying waiting times. For coherent manipulation of the qubit, the heating rate needs to be sufficiently small (in the order of a few tens of phonons per second). Then, using Ramsey spectroscopy, the ion's coherence and motional coherence can be measured.

All this techniques are based on the coherent manipulation of our ion. In our research group, this manipulation is done with the 729 nm qubit laser. As it would be time consuming to set up this laser beam and to install all these techniques, we first wanted to focus on our main goal of coupling the ion to the light field of the cavity. For that, we characterized our fiber cavity in vacuum (next section), and continued afterwards with the ion-photon coupling in Chapter 5.

4.5 Characterization of the fiber cavity in vacuum

After the first ions were trapped and some of their properties were characterized, measurements of the fiber cavity were carried out under ultra-high vacuum. First, measurements of the cavity transmission confirmed the target characteristics of the fiber cavity, as calculated in Section 3.1. Next, the stability of the fiber cavity was characterized and improved to bring it into resonance with the ion's transition. Here we observed a relative drift of two stabilized lasers in the fiber cavity's transmission. This drift is investigated in the last subsection.

4.5.1 Measurements of the fiber cavity integrated with the ion setup

For the characterization of the fiber cavity in our vacuum chamber, one important property is the dependence of the finesse on the cavity length. In our ion-trap design (Section 4.1), the cavity length is should be 400–500 μm, to couple an ion with the fiber cavity with sufficient optical access. Therefore, it is important to achieve a high finesse in this regime, which we were able to confirm with the following measurements.

Before the vacuum setup was assembled, the fiber cavity was measured in air to check that the cavity fulfilled the target cavity parameters. Following the method presented in Section 3.3, the cavity length and linewidth were measured for several cavity lengths. At this point, the experimental setup for the measurement of these parameters was not yet equipped as shown in Figure 3.11. For measurements in air, the absence of both the stepper motor and the second laser led to errors in the length measurements up to 20 μm.

For measurements in vacuum, the nanopositioners (see Section 4.1.3) were used to align the cavity and change its length. As these slip-stick piezos stages have no independent calibration of their position, the CCD camera for ion detection was used to measure the cavity length. In the view of the camera, the pixel to metric-distance conversion was calibrated using two independently known quantities, the fibers' diameters and the separation of the radial electrodes, yielding a conversion factor of 0.83(4) μm/px. When the fibers were not visible on the camera because they were obscured by the blades for cavity lengths $L > 400$ μm, we rely on the reproducibility of the step-by-step actuator displacements, which we calibrate by displacing the fibers in the field of view of the CCD camera.

Single steps increasing or decreasing the cavity length with the MM fiber correspond to displacements of 1.7(1) μm and 2.2(1) μm, respectively, while single steps moving down or up the PC fiber correspond to respective displacements of 2.0(1) μm and 1.8(1) μm. We then assume that the distance traveled per step remains constant when the fibers are retracted out of the field of view. To test this assumption, we start with a fiber at a reference position within the field of view. We retract it by a given number of steps, then reverse the direction by the number of steps that according to our calibration should cover the equivalent distance. For the MM fiber, we recover the reference position within ± 25 μm for any displacement up to 2.0 mm; we thus estimate 25 μm to correspond to a 2σ deviation and use a value of 13 μm for the uncertainty in the position of the MM fiber. The PC fiber has a reproducible behavior with the same uncertainty up to a retraction of 0.75 mm from the trap center. For larger displacements of fiber P up to 1.6 mm, the load on the piezo actuator is modified, most likely due to contact between the fiber and the vacuum chamber, resulting in a less reliable calibration. In this regime, we estimate the 2σ deviation of d_{P} to be 60 μm and the uncertainty to be 30 μm.

Light transmitted by the cavity was detected using a home-built photodiode from our electronics workshop. With a limited power of the laser light, the transmission of long cavities was below $10\ \mathrm{mV}$ at the oscilloscope so that the measurement with uncertainties of $4\ \mathrm{mV}$ was impractical. In this case, the reflected signal was used to determine the linewidth as this signal is stronger due to the higher transmission of the PC fiber (see Subsection 3.2.3).

The PC fiber with a radius of curvature $R_{\mathrm{PC}} = 300(10)\ \mu\mathrm{m}$ and the MM fiber with $R_{\mathrm{MM}} = 360(10)\ \mu\mathrm{m}$ were selected for the cavity that was built into our vacuum chamber. In Figure 4.8(a), the cavity finesse is plotted as a function of the cavity length. As expected from Equation (3.8), no stable Gaussian modes were found for any alignments with a cavity length between the R_{PC} and R_{MM}. For measurements in air, a maximal finesse of $66\,000(5\,000)$ was found at $L = 182(3)\ \mu\mathrm{m}$. Subtracting the transmission of the mirrors, the losses of each mirror are around $39(5)$ ppm. These losses are significantly higher than the 12 ppm expected from the maximal scatter and absorption losses for the fiber mirrors; see Table 3.1. Indeed, we measured finesse values up to $100\,000$ for length $L > 200\ \mu\mathrm{m}$ for other fiber cavities; more details can be found in Section 7.1. Unfortunately, in the preparation stage, other fiber mirrors corresponding to cavities with such a finesse broke in the process of assembly, and in the end, this pair of fibers was built into the vacuum chamber. However, one advantage of this fiber cavity is that the finesse at $L = 500(15)\ \mu\mathrm{m}$, $\mathcal{F} = 50\,000(6\,000)$, is only slightly less than the value found at $182(3)\ \mu\mathrm{m}$. A similar moderate decrease in finesse was observed in vacuum after the bake-out. For cavities with $L > 200\ \mu\mathrm{m}$, the finesse was decreased down to $40\,000(8\,000)$ showing additional 40 ppm of losses. We attribute these additional losses to a sub-optimal alignment of the fibers. As expected from our measurement of Subsection 3.3.3, an angular alignment better than $\pm 1^\circ$ would be necessary for an optimal alignment, and this alignment should be checked at the time of assembly. However, measurement at the time of assembly was not sensitive enough to detect this misalignment. Additional angular displacement could have happen at the vacuum bake out. Later, a photograph taken with the ion CCD camera under vacuum was analyzed and we found an angle of $1.5(2)^\circ$ between the fibers.

The reduction in the finesse by around 20% from air to vacuum, or by a factor of two compared to the best measurements of fiber mirrors from the same coating run, has two major consequences. First, the cavity decay rate is increased by the same factor; see Figure 4.8(b). Comparing this cavity decay rate $\kappa \approx 2\pi \cdot 4\ \mathrm{MHz}$ with the expected ion-photon coupling strength $g_0 \approx 2\pi \cdot 20\ \mathrm{MHz}$ and with the atomic decay rate of $2\pi \cdot 11.4\ \mathrm{MHz}$, we still find a high cooperativity $C \approx 4$ for our calcium ions coupled to the fiber cavity. Even the strong coupling is still feasible, with $g_0 > \kappa, \gamma$.

The second consequence is a reduction in the probability that a photon leaves the cavity. This probability depends on the mode coupling between the cavity and output fiber mode, and can be calculated with Equation (3.9); see solid line in Figure 4.8(c). To compare the calculations with the measurements, the amplitude of both transmission measurements, before and after the vacuum assembly, are normalized to their maxima. For cavity lengths $L < 300\ \mu\mathrm{m}$, no structure of the measurement is observed. However, for the target cavity lengths $400 < L < 500\ \mu\mathrm{m}$ and up to $600\ \mu\mathrm{m}$, the measurements and calculations have a comparable relative decrease for longer cavities. The reduction of the absolute values of the measured mode couplings can be explained by an angle in the cavity alignment and the reduced finesse for this cavity length. In other words, the probability for a photon to leave the cavity is given by the ratio of the transmission of the output mirror to the total losses of the cavity determined by the finesse. Thus, with a

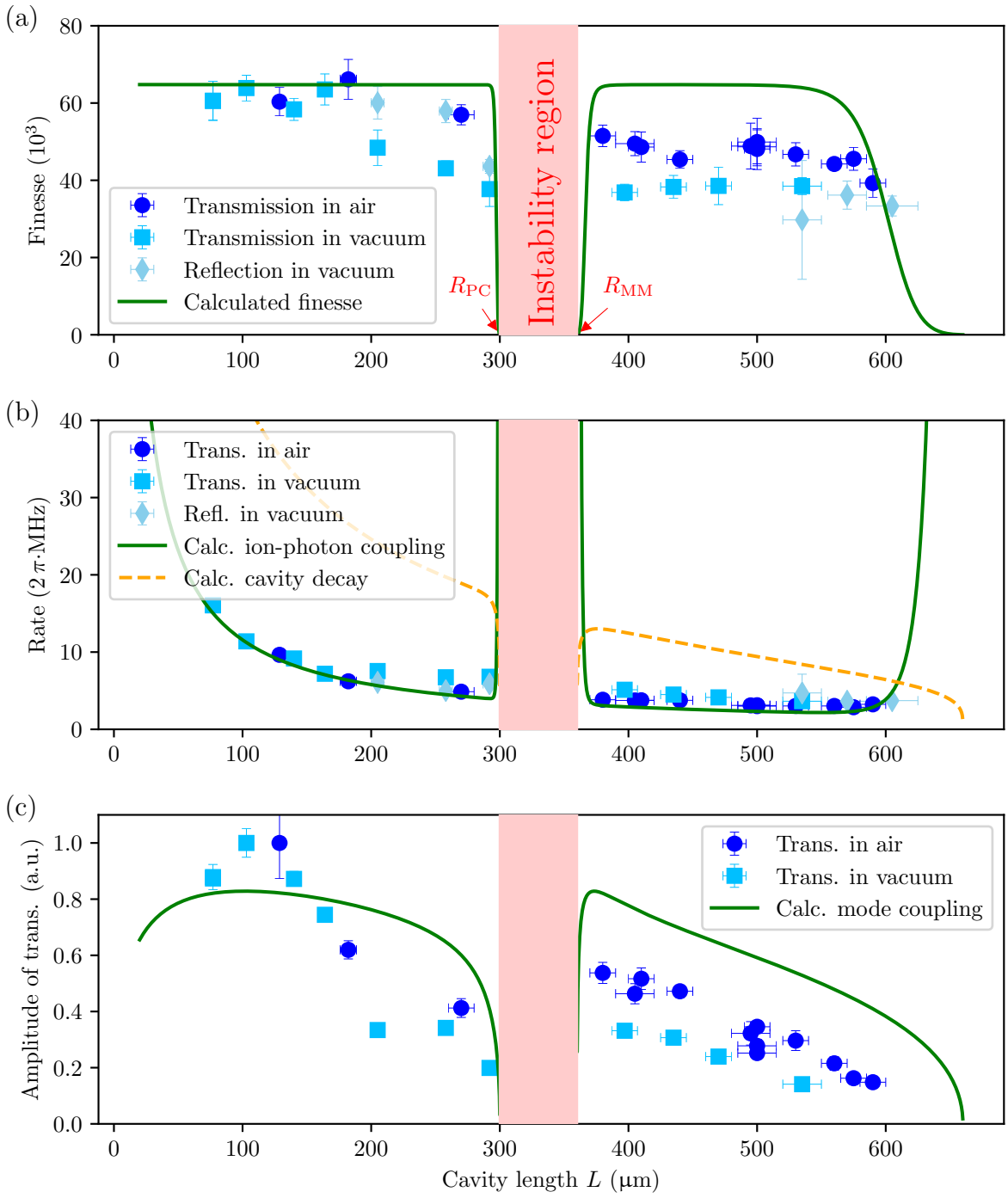

Figure 4.8: Measurements of our fiber cavity in air before the vacuum system assembly and afterwards under vacuum, as a function of cavity length L. (a) The cavity finesse determined by linewidth measurements of the transmitted and reflected cavity signal. The calculated finesse Equation (3.11) includes the transmission of the mirrors, losses of 40 ppm for each mirror and clipping losses (Equation (3.13), where the effective useful diameter is $D = 80$ µm. (b) The half-line width is plotted for measurements before and after vacuum assembly and calculations as in (a). Additionally, the expected ion-photon coupling strength g_0 is calculated as in Equation (4.1). (c) The amplitude of the transmission signal is normalized to the maximum of each measurement. The mode coupling (green solid line) is calculated following Equation (3.9).

decreased finesse, that means increased total losses, the probability to detect a photon leaving the cavity is reduced. For proof-of-principle experiments, where photons form the cavity are measured, this drawback can be compensated by an increased measurement time so that such experiments would be still possible.

4.5.2 Locking the fiber cavity

As introduced in Section 2.2, the cavity has to be near-resonant with an atomic transition or with a Raman transition frequency, if it is to be coupled to an ion. To keep the cavity resonant, it is necessary to stabilize the cavity frequency to at least within its linewidth 2κ. With Equations 3.2 and 3.12, this requirement can be translated that the fiber cavity length needs to be stable with $\Delta L \leq \lambda/(2\mathcal{F}) \approx 10\ \mathrm{pm}$.

In Cavity-QED experiments, the two mirrors of a cavity are typically mounted as stably as possible with respect to each other. For example, in our group's experimental setup with substrate mirrors, the mirrors are glued onto a U-shaped metal frame [81]. The only movable elements are shear-mode piezos, which are built in to tune the cavity length. A diode laser with a wavelength at $783\ \mu\mathrm{m}$ stabilized to a reference cavity is used with a Pound-Drever-Hall-scheme (PDH) [175, 176] to stabilize the experiment cavity [84]. This transfer-lock technique was sufficient to stabilize the cavity frequency within its linewidth.

In contrast, our fibers are mounted on individual nanopositioners (see Subsection 4.1.3) to align the cavity in vacuum and to trap ions while the fibers are retracted. Measurements of the error signal in a free-running PDH-configuration, (see Appendix A.2) showed resonances of these piezo stacks at frequencies from 500 to $900\ \mathrm{Hz}$; see blue curve in Figure 4.9(a). Such low frequencies have the following two major disadvantages. First, the lower the frequency, the higher is the amplitude of the piezo stack's movement for noise with the same energy. Second, for active stabilization, the feedback needs to be limited such that the resonances are not excited. As a consequence of both these properties, noise excites the low-frequency resonances of the nanopositioners with high amplitude, but the shear-mode piezos cannot be used to compensate for those fluctuations because the feedback would excite the resonances further.

Despite these low-frequency resonances, the required stability of the fiber cavity can be achieved by decoupling the system from noise sources, as is done for scanning probe microscopes [177]. In our vacuum system assembly, we added Viton O-rings between the piezo stacks and the vacuum chamber to reduce the vibration. Without any external vibration isolation outside the vacuum chamber, the jitter of the transmitted cavity resonance was estimated to be around $1\ \mathrm{nm}$. This jitter means that the PC fiber mirror moved with respect to the MM fiber mirror by around $1\ \mathrm{nm}$. An upgrade of the vibration isolation in vacuum would require a fundamental redesign and rebuild of our experimental setup, so that we decided to isolate the entire vacuum chamber in air.

Mechanical vibrations were isolated by inserting two layers of damping material into the mount of the setup, as sketch in Figure 4.9(a). First, eight vibration-absorbing feet[9] were inserted between the breadboard and the feet mounted on the optical table. Second, the vacuum chamber was placed on four pads[10] separating it from the breadboard on which it sits. With this

[9] Thorlabs AV6 Sorbothane feet

[10] Toroidal 1 inch-thick Thorlabs Sorbothane sheets, cut to an inner diameter of $38\ \mathrm{mm}$ and an outer diameter of $51\ \mathrm{mm}$

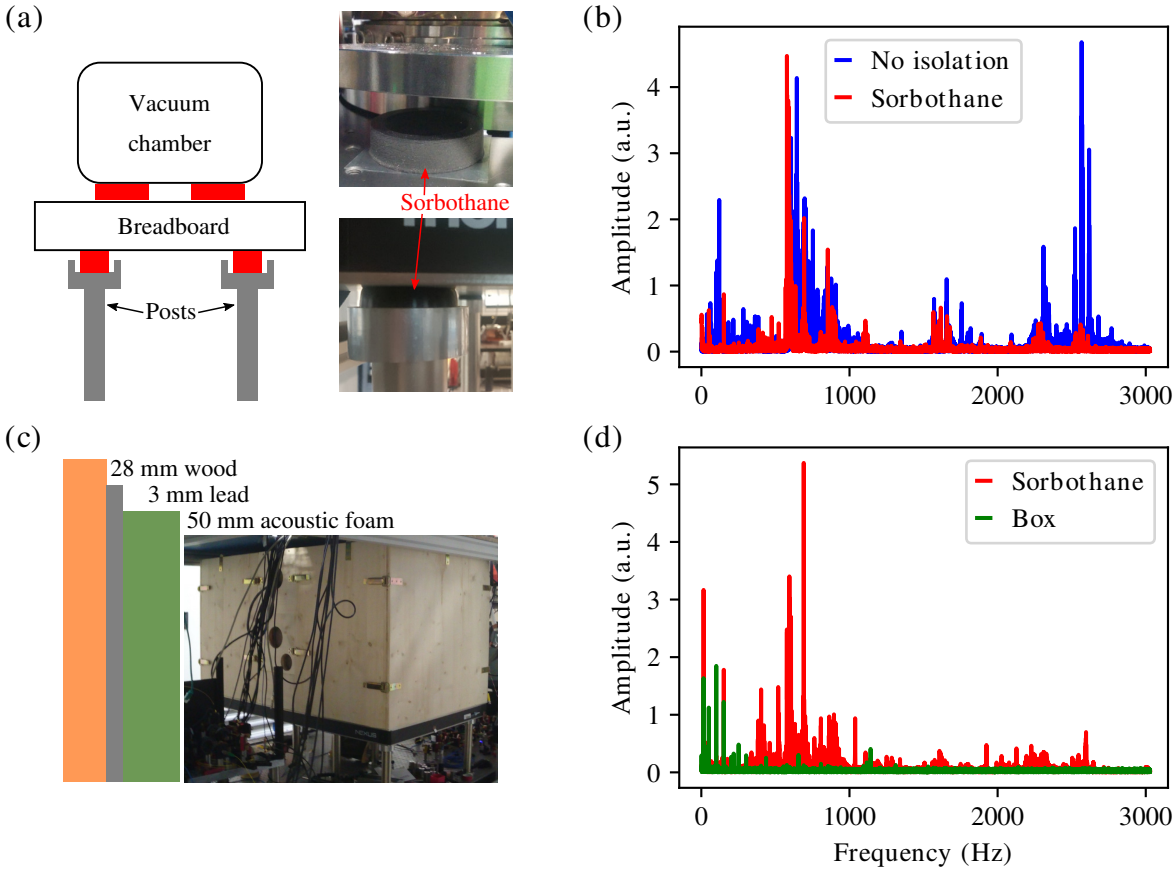

Figure 4.9: Schematics and photographs of the vibration isolation in (a) and (c). First, we installed two levels of Sorbothane pads (a). Second, a box was installed above the vacuum chamber to shield the acoustic noise (c). Frequency analysis of cavity error signal in (b) and (d).

vibrational isolation, the jitter was reduced to approximately 400 pm. Florian Ong calculated and optimized the sizes, shapes and positions of these Sorbothane pads for our experimental setup following the Sorbothane's designer and products guide [178, 179]. The vibrations were significantly reduced especially for higher frequencies above 2 kHz (see red curve in Figure 4.9(b)), but the length of the locked cavity still varied by fluctuations in the frequency domain which were larger than the linewidth of the cavity.

To further reduce the acoustic noise, a home-made box surrounding the vacuum chamber was installed, similar to the acoustic isolation of reference cavities or lasers in our lab [180]. A 28 mm thick wooden cube, open at the bottom, was lined with a 3 mm-thick layer of lead. Another layer of 50 mm-thick acoustic foam on top of the lead is intended to prevent standing waves inside the box; see Figure 4.9(c). The box was put onto the breadboard over the vacuum chamber. When a speaker excited the closed box with white noise, a microphone in the box measured a reduction of 20–40 dB for frequencies higher than 100 Hz compared to the microphone placed below the box. After this box was installed, the jitter of the free-running cavity was reduced by another factor of two to roughly 200 pm, and frequencies higher than 100 Hz were damped to the noise level of the error signal at the spectrum; compare red and green curve

in Figure 4.9(d).

We tested the lock of the fiber cavity with a tunable laser[11]. With wavelengths ranging from $750\ \mathrm{nm}$ to $810\ \mathrm{nm}$, we could adjust the linewidth of the fiber cavity (see transmission in Figure 3.8) to optimize the cavity PDH error signal for the lock. Afterwards, we decided on a diode laser with a wavelength of $808\ \mathrm{nm}$ for the transfer lock from a reference cavity[12] to the fiber cavity. With this transfer lock, the amplitude of the transmission of an $866\ \mathrm{nm}$ laser which was brought into resonance with the cavity by detuning the stabilized $808\ \mathrm{nm}$ laser with a fiber-based electro-optic modulator (fiber-EOM – see Appendix A.2) was stable above 90%. Such a transmission characteristic means the residual jitter of the locked cavity was less than half the linewidth from peak to peak. A further improvement, using an FPGA-based finite-impulse-response filter [181], was only tested in the fiber cavity setup without isolation. As it did not lead to any improvement of the lock, it was replaced by a fourth-order low-pass filter with a cut-off frequency of $4\ \mathrm{kHz}$. After the installation of the isolation box, the FPGA-based filter was not tested again because the lock performed sufficiently. In a future setup, the FPGA-based filter could improve the cavity lock further by filtering with multiple, adjustable notch-filters [84] or by canceling the individual resonances [181].

4.5.3 Drift of "double resonance"

While locking the fiber cavity to the reference cavity and monitoring the transmission for several minutes, we observed a drift depending on the temperature in the lab. In Figure 4.10, the temperature of our lab is plotted as orange crosses recorded by a temperature sensor attached to the vacuum chamber. The orange line in this plot is a smoothed interpolation of the measured temperature. The observed frequency difference between the lock laser ($808\ \mathrm{nm}$) and the repumping laser ($866\ \mathrm{nm}$) is shown as green points. It was measured by recording the frequency which was applied to the fiber EOM to tune the lock laser to the double resonance. The measured frequency difference was fitted to the interpolation of the measured temperature where a time delay of $3.1\ \mathrm{h}$, a scaling of $198\ \mathrm{MHz/K}$, and an offset of $27.15°\mathrm{C}$ are free parameters to fit. The delay of about three hours required for an overlap between the two datasets can be explained by the fact that the fibers are inside the vacuum chamber which delays thermalization.

Both lasers were locked to the same temperature-stabilized reference cavity with a free spectral range of $1.5\,\mathrm{GHz}$ compared to the $300\,\mathrm{GHz}$ of the fiber cavity. Consequently, we assume that this drift of the "double resonance" must originate from some process inside the fiber cavity. One possible explanation is the length change of the $\lambda/4$-stack of the highly reflective coating [182]. A wavelength-dependent change of the thickness of the coating layers would shift the resonance frequency of the mirror. For an estimate of this effect, I calculated the phase of the reflected mirror as a function of the temperature [144]. Hereby, the thermal expansion coefficients provided by ATFilms were used. With the repumping laser in the center of the coating curve of Figure 3.8 and the locking laser at the slope, the different phase shifts at these different wavelengths results in a relative frequency shift of about 10–$20\ \mathrm{MHz/K}$. Compared to the measured relative frequency shift of $198\ \mathrm{MHz/K}$, this effect cannot fully explain the drift. More precise measurements and studies are necessary to investigate whether the smaller radii of curvature have an influence. Certainly, fibers as substrates and smaller radii of curvature could

[11] M Squared SolsTiS narrow linewidth Ti:sapph laser

[12] Stable Laser Systems ATF-6010-4 cavity in a vacuum housing VH6010-4

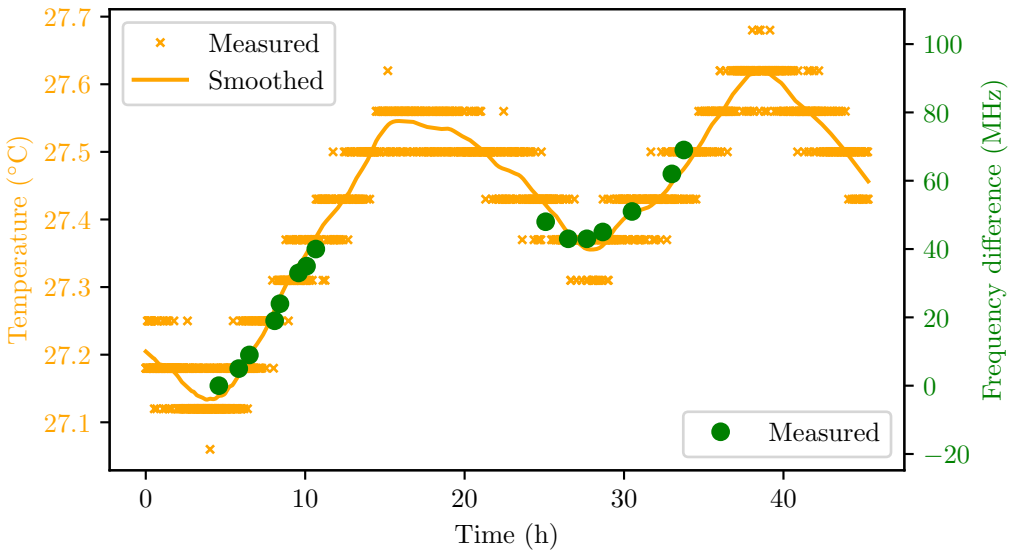

Figure 4.10: Drift of the "double resonance", that is, the difference between the frequencies for which an 808 nm laser and an 866 nm laser are resonant with the cavity: The orange crosses show the temperature outside the vacuum chamber for a measurement of 48 h. The orange solid line is the smoothed temperature measurement. In green the frequency difference between the resonant frequency of the 808 nm lock laser and the resonant frequency of the 866 nm repumping laser is plotted. The green data is shifted by 3.1 h to the past to overlap the frequency difference with the temperature change.

induce more stress which is known to distort the film packing [182]. In the end, this effect could be compensated by adjusting the frequency of the lock laser. As this way of compensation did not limit our experiments, we did not further investigate this drift, and we left this question open for later studies.

4.6 Charge manipulation

After both the fiber cavity and the ion trap were characterized individually, we tried to build the interface between the ion and the cavity. As experienced in the previous setup, charges on the fibers were present. Unfortunately, these charges prevented us from forming a cavity around the ion, as the ion was pushed out of the center of the trap along the trap axis. First Florian Ong and I, later with the help of Pierre Jobez, tried to minimize the charges on the fibers, as described in the following subsections. In the end, we were able to couple the fiber cavity to the ion, as presented in chapter 5.

Besides our work with charged dielectrics next to an ion trap, our colleague Ben Ames and master's student Johannes Ghetta were working on a similar project at around the same time as previously mentioned. In their case, they were trying to bring a trapped ion in a linear trap close to a nanofiber, which was fabricated in a collaboration with Prof. Rauschenbeutel's research group in Vienna [183]. Their goal was a distance of less than $10\ \mu\mathrm{m}$ between ion and nanofiber to show a couple the ion to the evanescent field surrounding the fiber. Hereby, they were tackling the same problem, that charges on the fiber repel the ion, so we adopted some of their techniques and methods.

4.6.1 Charging method

The method we used to manipulate charges on dielectrics in an ion trap is based on creating photoelectrons and guiding them onto the dielectric surfaces. Photoelectrons can be created by shining UV light onto a metal surface. In the scope of his master's thesis, Johannes Ghetta investigated this source of electrons and the electron trajectories through the trap with respect to the nanofiber. Ben Ames then studied the process of attaching and detaching electrons on this nanofiber. Slow electrons simply get stuck on the dielectric surface. In contrast, fast electrons are scattered from the dielectric and expel other electrons depending on the kinetic energy of the fast electrons. This effect is known as secondary electron emission (SEE), and it can be controlled by externally applied electric fields [184].

4.6.2 Experimental implementation

Taking advantage of the SEE effect, we are able to manipulate the charge state of our fibers in vacuum. Around $30\ \mathrm{mW}$ of power from a $393\ \mathrm{nm}$ laser[13] were focused onto a blade electrode. The work function of the gold-plated blade, with $4.8\ \mathrm{eV}$, is higher than the energy provided by laser photons, $3.2\ \mathrm{eV}$, and therefore, we would not expect any electrons to be emitted from the surface. However, our observations are consistent with photoelectron emission, which we attribute to impurities like calcium from our oven which has a work function of only $2.9\ \mathrm{eV}$, or to sharp edges with concentrated electric fields. During the $393\ \mathrm{nm}$ laser illumination, the RF trap drive was switched off, and a DC voltage was applied to the illuminated electrode to change the kinetic energy of the electrons hitting the fibers. By means of this DC voltage, the SEE could be tuned such that both positive charging and negative charging of the fibers were possible.

[13] M Squared SolsTiS narrow linewidth Ti:sapph laser with external cavity doubler ECD-X

4.6.3 Observations after charging

In the beginning of our efforts to manipulate fiber charges, we tried to minimize the charges on each fiber individually. One fiber was placed via the nanopositioning stages next to the trap center, whereas the other fiber was fully retracted by $\sim 2\ \mathrm{mm}$ from the trap center. In that configuration, the charge manipulation, as described in the previous subsection, was mainly applied to the fiber close to the blades. After charge manipulation, when we wanted to load an ion into the trap the charge-manipulated fiber was retracted. After loading, in order to investigate the effects of the charge manipulation, this fiber was moved back to the trap center, while a trapped ion was used as a sensor. A positively charged fiber repelled the ion, whereby with a neutral fiber, the ion remained in the trap center, and with some negative charge, the ion was attracted. This method was iterated with different voltages applied to the trap blade during the 393 nm illumination as long as the fiber could not be placed next to the ion. We were able to neutralize the charges on a given fiber using this method. However, it turned out that this neutralization did not enable us to conduct ion-cavity experiments because the charge state of the fiber drifted after loading. Consequently by the time, we could adjust the fiber cavity around an ion, the fibers were already charged again. These drifts are discussed in more detail in Section 6.6.

We were only able to load an ion inside the fiber cavity after we changed the configuration of the charge manipulation. Instead of individually charging or discharging each fiber and moving the fibers afterwards into a cavity configuration, both fibers were kept at the cavity position near the trap center while the charge manipulation was applied. Again, we applied different voltages to the illuminated blade, and we found that the fibers became charged in different ways. Once the charge state of both fibers was sufficiently neutral, an ion was loaded directly in the vicinity of the fibers. Without any movement of the fibers, the charges remained sufficiently stable for a couple of hours that it was possible to determine a coupling between the fiber cavity and an ion, as reported in the following chapter.

Chapter 5

Coupling an ion to the fiber cavity

To build a quantum interface with strong coupling between an ion and our cavity, we knew it would be necessary to place the ion at the maximum of the fiber cavity's standing wave. The cavity can be aligned with respect to a trapped ion by maximizing the fluorescence observed when the ion is repumped by the standing-wave field of the cavity [49]. After minimizing the fibers' charges (Chapter 4), we were able to carry out such an experiment at our fiber cavity setup, which is presented in this chapter. The main part of the successful coupling between an ion and the fiber cavity was achieved by Florian Ong, with help from Pierre Jobez and myself.

5.1 Experimental configuration

An ion was stored in our trap with the dimensions presented in Subsection 4.1.3 and the following parameters: The RF blades were driven with a frequency of $\Omega = 2\pi \cdot 30.186\ \mathrm{MHz}$ and an amplitude of $V_{\mathrm{RF}} \approx 110\ \mathrm{V}$, resulting in a radial confinement with $\omega_{\mathrm{rad}} \approx 2\pi \cdot 1.6\ \mathrm{MHz}$. The compensation electrodes were grounded, so no micromotion compensation was applied, as such a procedure would have been too time consuming to repeat for all ion positions. Along the axial direction, the ion was stored by applying a mean endcap voltage $V_{\mathrm{ec,M}} = 1\ \mathrm{kV}$, resulting in an axial confinement of $\omega_{\mathrm{ax}} \approx 2\pi \cdot 200$–$350\ \mathrm{kHz}$ depending on the exact charge state of the fibers and position of the ion; see Chapter 6. To measure the cavity beam radius, the ion was displaced along the trap axis by an endcap difference $V_{\mathrm{ec,D}} = V_{\mathrm{ec,R}} - V_{\mathrm{ec,L}} \in [-250, 250]\ \mathrm{V}$. The corresponding position of the ion for each value of $V_{\mathrm{ec,D}}$ was measured by the CCD camera with a precision of ± 1 pixel and conversion factor of 0.83(4) µm/px, as explained in Subsection 4.5.1

For each ion position, ion fluorescence was detected with the following sequence, illustrated in Figure 5.1. First, the ion was Doppler-cooled for $5\ \mathrm{ms}$ (see Subsection 2.1.3) with the $397\ \mathrm{nm}$ and the $866\ \mathrm{nm}$ beams, both coupled through the holes of the endcaps. Then, the same two beams with optimized frequency and amplitude for detection were used to measure fluorescence of the ion for $10\ \mathrm{ms}$ by means of a photomultiplier[1] tube with a bandpass filter for $397(3)\ \mathrm{nm}$. As this free-space detection collected both the ion's fluorescence and the background scatter from the blades and fibers, an additional detection of the background was carried out. For $10\ \mathrm{ms}$, only the $397\ \mathrm{nm}$ laser was active, so that the ion was optically pumped to the $D_{3/2}$ state in absence of the repump light, and the ion remained dark. Subtracting this background signal

[1] Hamamatsu, Head-on PMT, Photon Counting Head H7360 Series

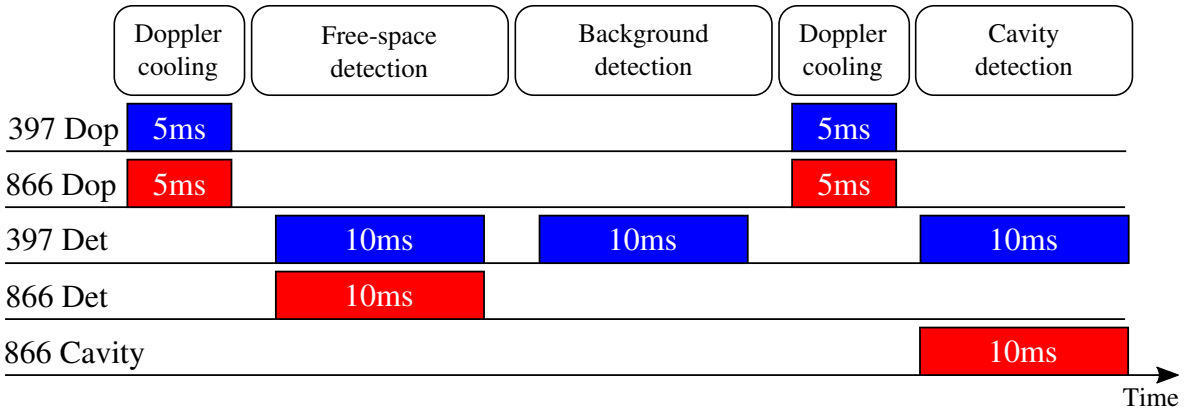

Figure 5.1: Experimental timing sequence for the demonstration of the coupling between a trapped ion and the fiber cavity. First, the ion was Doppler-cooled (Dop) for 5 ms. Then, the ion's fluorescence rate was detected (Det), and the background scattering rate was measured. Another Doppler-cooling step ensured that the ion was properly cooled again after the fluorescence measurement. Last, the ion's fluorescence was detected while it was repumped by the cavity field.

from the signal acquired in the presence of a repump yielded the bare fluorescence rate of the ion, as independently calibrated with free-space laser beams. This background-subtracted free-space detection through the endcaps was also carried out to monitor the beam alignment over the different ion positions.

After detection with the free-space beams, the ion was again Doppler-cooled for $5\,\mathrm{ms}$. For detection using the cavity repump field, the ion was illuminated by the $397\,\mathrm{nm}$ beam through the endcaps. At this step, a $866\,\mathrm{nm}$ repump field[2] red-detuned by $\Delta = 100\,\mathrm{GHz}$ from the atomic transition between the $3^2\mathrm{D}_{3/2}$ and $4^2\mathrm{P}_{1/2}$ states was coupled into the fiber cavity. A necessary step for this coupling was that the fiber cavity was locked to an $808\,\mathrm{nm}$ diode laser[3] to stabilize the cavity length at $L = 420(20)\,\mu\mathrm{m}$, in resonance with the far-detuned $866\,\mathrm{nm}$ laser light. As this free-running $808\,\mathrm{nm}$ laser or the double resonance (see Subsection 4.5.3) was drifting a few megahertz per minute, its frequency was adjusted continuously by hand to keep it in resonance with the far-detuned $866\,\mathrm{nm}$ laser. At this time, no single-photon counting module (SPCM) was set up and the transmission of the fiber cavity was detected only by photodiodes. Around $180\,\mu\mathrm{W}$ of $866\,\mathrm{nm}$ light was coupled into the fiber cavity to achieve a sufficient transmission at the cavity output which was monitored for the manual stabilization of the cavity length.

As the light field is enhanced by the cavity, a high power up to $1.5 \cdot 10^7 \mathrm{W/cm^2}$ can build up inside the cavity. Such a power saturates the ion so that the transition is broadened up to hundreds of gigahertz. To avoid any vacuum-induced cavity effects while Doppler cooling, the cavity should be off-resonant with the ion transition. A blue detuned repump light would heat the ion, so that we red-detuned the cavity and repump laser.

[2] M Squared SolsTiS narrow-linewidth Ti:sapph laser stabilized to a Stable Laser Systems ATF-6010-4 cavity in a vacuum housing VH6010-4

[3] Toptica DL-Pro

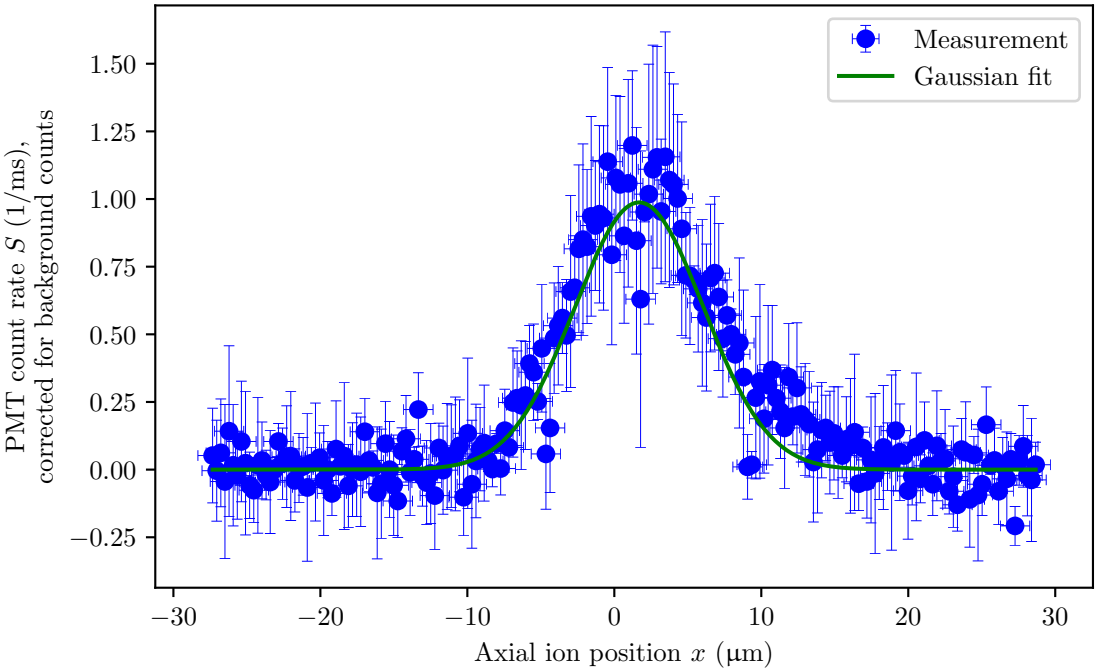

Figure 5.2: Background-corrected measurement of the ion's fluorescence S as a function of the axial ion position x. The ion was repumped by the fiber-cavity field. A Gaussian curve was fitted to the data to determine the beam waist ($1/e$ radius) $w = 4.4(2)\,\mu\text{m}$ of the fiber cavity mode.

5.2 Results

While the ion was repumped with the $866\,\text{nm}$ light coupled through the fiber cavity according to the sequence shown in Figure 5.1, the ion's fluorescence was measured on the PMT, with 50 repetitions for each of 201 different voltages $V_{\text{ec,D}}$. The applied voltage is converted to the axial ion position x by the calibration explained in Section 5.1, with $x = 0\,\mu\text{m}$ for $V_{\text{ec,D}} = 0\,\text{V}$. The background-corrected fluorescence S is plotted in Figure 5.2 and follows the Gaussian shape expected for the transverse cavity mode. The maximum count rate $S_{\text{max}} \approx 1.2\,/\text{ms}$ of the measured cavity fluorescence is small when compared to the maximum observed fluorescence rate with a free-space repump, of 30–35 $/\text{ms}$. This reduced fluorescence rate is expected by the detuning $\Delta = -100\,\text{GHz}$ of the $866\,\text{nm}$ repump laser in the cavity with respect to the D–P transition. Given this small count rate, the signal-to-noise ratio of the background-corrected fluorescence is only around two.

A function for the radial intensity of a Gaussian beam

$$S(x) = S_0 e^{-2\left(\frac{x}{w}\right)^2} \tag{5.1}$$

with w the beam radius ($1/e$) of the cavity mode is fitted to the measured fluorescence. We expect that this is the correct function because the cavity is perpendicular to the linear ion trap, and we are translating the ion along the trap axis. An amplitude of $S_0 = 1.0(1)\,/\text{ms}$ and a beam radius of $w = 4.4(2)\,\mu\text{m}$ were determined from the fit. In comparison, with a length

of $420(20)\,\mu\mathrm{m}$ and mirror radii of curvature $R_{\mathrm{PC}} = 300(10)\,\mu\mathrm{m}$ and $R_{\mathrm{MM}} = 360(10)\,\mu\mathrm{m}$, as presented in Subsection 4.5.1, a beam waist ($1/e$ radius) of $3.4(1)\,\mu\mathrm{m}$ is calculated with Equation (3.3). The measured beam radius and calculated beam waist of the cavity field differ by more than three sigmas of uncertainty. This large difference indicates that our presented measurement was subject to further neglected effects which are discussed in the following.

5.2.1 Limited count rate

With the ion repumped by the cavity light field, the ion's fluorescence was detected with a maximum count rate of $1.2\,/\mathrm{ms}$, whereas with a free-space repump laser beam, detection rates up to $35\,/\mathrm{ms}$ were achieved. This low count rate is due to the fact that the $866\,\mathrm{nm}$ cavity field was detuned by $\Delta = -100\,\mathrm{GHz}$ from the D–P transition. This detuning was necessary in our experiments due to the following three reasons:

Strong repump light

A far detuned repump light was used to avoid the saturation of the ion by the repumping field of the cavity, while the transmission of the cavity light field was still strong enough to be detected by the photodiodes. Later, we installed a single-photon counting module[4] (SPCM) to detect the transmitted $866\,\mathrm{nm}$ light, and the higher sensitivity of this module would have enabled us to reduce the light inside the cavity. Unfortunately, after the implementation of the SPCM, we were no longer able to trap an ion between the fibers. The charges on the fibers had changed, and any further efforts to minimize the charges failed. The problem of charges is further discussed in the last subsection.

AC-Stark shift from locking laser

The diode laser that was used to stabilize the length of the fiber cavity induced an AC-Stark shift on the ion. Compared with the transfer-lock setup used in our group's cavity experiments with substrate mirrors [82, 84], two circumstances in our experimental setup cause AC-Stark shifts which cannot be neglected.

First, as explained in Section 4.5.2, it was necessary to perform the transfer lock with an $808\,\mathrm{nm}$ laser. The frequency shift Δ_{ll} between the lock frequency and atomic transition at $866\,\mathrm{nm}$ is smaller than the shift of the $786\,\mathrm{nm}$ lock laser used in our experiments with substrate mirrors. Consequently, our wavelength at $808\,\mathrm{nm}$ increases the AC-Stark shift $\Delta E \propto 1/\Delta_{\mathrm{ll}}$.

Second, the other CQED experimental setup in our group is locked to the TEM 01 cavity mode to reduce the light intensity at the ion[82], as the antinode of the TEM 00 mode is at the transversal node of the TEM 01 (see Figure 7.2(e)). For our fiber cavity, the mode coupling from the fiber into the cavity is determined by the relative alignment of the mirror on the fiber tip and the alignment of the cavity. While the coupling of repump light into the TEM 00 mode is optimized, a simultaneous coupling of lock light into the TEM 01 is reduced. Since our priority is to maximize the coupling of the repump light, the fiber cavity length was stabilized by the TEM 00 mode of lock light.

[4] LaserComponents, COUNT-10C-FC

As this AC-Stark shift is also position dependent, it would be complicated to keep the resonance between the cavity frequency and ion frequency. Consequently, the repump laser and the cavity were detuned by $\Delta = -100\,\mathrm{GHz}$ from the atomic transition.

Expected strong ion-photon coupling

Our fiber cavity, if it is well aligned, is expected to have a strong ion-photon coupling rate $g_0 = 2\pi \cdot 20\,\mathrm{MHz}$ to the calcium transition between the $P_{1/2}$ and $D_{3/2}$ states. Note, the bare atomic half-width decay from the $P_{1/2}$ state to the $D_{3/2}$ state is $\gamma_{\text{P-D}} = 2\pi \cdot 0.85\,\mathrm{MHz}$, see Figure 2.2. Furthermore, the expected strong ion-photon coupling rate of the cavity exceeds the half-width decay rate $\gamma = 2\pi \cdot 11.4\,\mathrm{MHz}$ from $P_{1/2}$ to $S_{1/2}$. Consequently, the fluorescence of an ion would be suppressed for our well-aligned fiber cavity, as the fiber cavity enhances the dark transition from $S_{1/2}$ to $D_{3/2}$. Further, not only would the detected ion fluorescence be changed by the varying ion-photon coupling during alignment, but also the effectiveness of Doppler cooling would depend on the alignment of the resonant cavity. For a strongly-coupled cavity in resonance with the ion's transition, the alignment would thus have to be optimized by a more complex technique involving additional transitions of the ion. For example, the Raman transition from $S_{1/2}$ via $P_{3/2}$ to $D_{5/2}$ could be measured, as it leaves the Doppler cooling transitions undisturbed. Another option would be to study the change of the photon emission during the cavity alignment process, as reported in [185].

5.2.2 Ion-cavity localization

For maximal ion-photon coupling, the ion needs to be localized to within tens of nanometers at the antinode of the cavity's standing wave. In our experimental setup, there are the following three reasons why we are unable to achieve such a precise alignment between ion and cavity.

Ion cooling

Using the cooling beams that were aligned through the holes of the endcaps, we were only able to implement Doppler cooling along the trap axis. Optical access for cooling in the radial directions is available in the radial plane, but it would need to be readjusted for each measured ion position or a cylindrical beam. Neither the realigning of the cooling beams nor a cylindrical beam were implemented. With radial trap frequencies $\omega_{\mathrm{rad}} = 2\pi \cdot 1.6\,\mathrm{MHz}$ similar to those of the experiment in [84], a Doppler-cooled ion wave packet in our fiber cavity would have a radial extent of $\Delta x_{\mathrm{rad}} \approx 46\,\mathrm{nm}$, similar to that of [84] (see Equation (2.14)). However, our axial trap frequency $\omega_{\mathrm{ax}} \approx 2\pi \cdot 200\text{–}350\,\mathrm{kHz}$ does not permit sufficient Doppler cooling. Consequently, the estimated axial wave packet size is $\Delta x_{\mathrm{ax}} \approx 1\,\mu\mathrm{m}$. Actually, this axial wave packet extent can explain the larger measured beam radius of the fiber cavity as compared to the calculated value. For future experiments, additional cooling techniques like electromagnetically-induced transparency [186] or polarization-gradient cooling [187] could enable cooling close to the ion's motional ground state even with low axial confinement. Sideband cooling, however, would not be applicable after Doppler cooling with such low axial confinement.

Micromotion

As mentioned in Section 5.1, no voltages were applied to the compensation electrodes for the data plotted in Figure 5.2, so that additional motion of the ion enlarged the wave packet. For the measurement presented, compensating micromotion at each ion position would have been too time consuming, but for the final ion position at the antinode of the fiber cavity, a micromotion compensation as presented in Subsection 4.4.1 would be feasible, or more precise methods could be applied [167, 168]. Note that because of the dielectric fibers, micromotion is also present along the trap axis.

Other radial ion position

The alignment of the fiber cavity along the camera view (z-axis) should be adjusted. For the alignment along the z-axis, both fibers have to be moved with the nanopositioners. As these positioners are slip-stick piezo stages without any absolute reference, the step sizes corresponding to a given applied voltage are different for each stage and even along the range of the motion of each stage. Thus, a cavity realignment would be necessary for each new fiber position. Each cavity realignment at a new position takes several minutes, so that an entire scan along the z-axis would take several hours. In the measurement presented here, we were not able to adjusted this axis because the charges on the fibers change faster than the alignment procedure, as explained in the following.

5.2.3 Charges on the fibers

Running experiments reproducibly over several hours, which would be necessary to optimize the coupling between the fiber cavity and the ion, is limited by the stability of the charges on the fibers. Fibers, whose charging state is almost neutral, are found to be charged positively again as described in Section 4.6. In particular, our PC fiber showed such behavior. To minimize the charges ending up with charges on the fibers, which allow a coupling between the ion and the cavity, some iterations of charge manipulation (cf. Subsection 4.6.2) needed to be carried out. For each charge manipulation step, the ion trap's RF drive was switched off. After the charging process, a new ion needed to be loaded. In total, one iteration of charge manipulation took 20–30 minutes. In fact, discharging of the fibers never worked reproducibly, so that up to tens of iterations were necessary to find both fibers charged in a state that the ion could be trapped between the fibers. Actually, after we tried to reproduce the measurements presented in Figure 5.2 for weeks without success, we decided instead to characterize the charges on our fibers in more detail. Therefore, a method to determine the charge densities on our fibers' surfaces was developed, which is described in the following chapter.

Chapter 6

Characterization of charges

As a consequence of the fact that we were not able to reproducibly couple an ion to our fiber cavity due to charging effects, we decided to investigate the charges on our fibers more precisely. This chapter describes a method to determine the surface charge densities of optical fibers, which we developed to determine a quantitative charge distribution. The following sections are also part of a manuscript published in [188].

6.1 Experimental setup

We apply a $30\,\mathrm{MHz}$ radio frequency (RF) signal on two opposing radial electrodes while grounding the remaining two radial electrodes. Single $^{40}Ca^{+}$ ions are trapped at radial and axial secular frequencies of $1.6\,\mathrm{MHz}$ and $200\,\mathrm{kHz}$, respectively (see Section 4.4). As presented in Section 4.1, the two fibers integrated with the ion trap can be independently translated relative to the ion-trap center along three axes using in-vacuum nanopositioners. Figure 6.1(a) shows a cutaway diagram of the ion trap in which most of the sapphire holder, one endcap, and one fiber have been removed.

We define the origin of the coordinate system to lie at the trap center. The trap axis x lies in the horizontal plane, and the fibers are mounted vertically, along the y-axis. Although the fibers can be moved over a few mm along the x- and z-axes, in the following measurements they are kept at positions with $x, z \in [-10, 10]\,\mu\mathrm{m}$. We use the two different types of fibers, as described in Section 4.5: fiber M is a multi-mode fiber[1] and fiber P is a photonic-crystal fiber[2] (see Table 3.2 for more details). The protective copper and polyimide layers of fibers M and P, respectively, were removed over more than $10\,\mathrm{mm}$ behind the tips, so that the cladding surfaces in the vicinity of the ion trap consist of silicon dioxide. The facets and the sides of the fibers thus constitute dielectric surfaces prone to trapping charges, which may be positive or negative. In this work, we will assume that these trapped charges can be described by homogeneous surface charge densities, called $\sigma_{\mathrm{M,f}}$, $\sigma_{\mathrm{M,s}}$, $\sigma_{\mathrm{P,f}}$ and $\sigma_{\mathrm{P,s}}$. The labels M and P identify the fiber, and f and s stand for “facet" and “side".

Figure 6.1(b) presents a sketch (not to scale) of a view along the trap axis depicting the fibers' positions relative to the ion trap. The facets of fibers M and P are held at distances d_{M}

[1] IVG Fiber Cu200/220

[2] NKT Photonics LMA-20

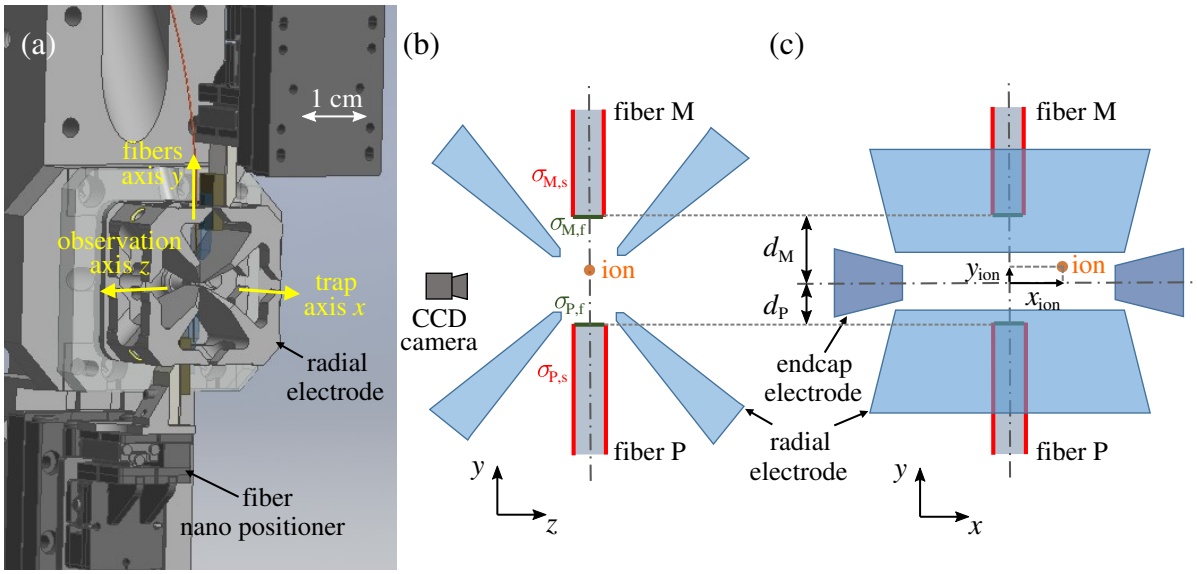

Figure 6.1: Experimental setup, more details in Section 4.1. (a) Cutaway drawing of the ion trap assembly. The linear Paul trap (center) is mounted on a sapphire base. The rest of the sapphire holder and one endcap electrode are not shown. Nanopositioner assemblies for the fibers are visible at the upper right and lower left. The upper fiber is shown, while the lower fiber has been omitted for simplicity. (b) Sketch, not to scale, of a view along the trap axis, indicating fibers M and P, surface charge densities $\sigma_{\mathrm{M,f}}$, $\sigma_{\mathrm{M,s}}$, $\sigma_{\mathrm{P,f}}$ and $\sigma_{\mathrm{P,s}}$, and the CCD camera position. (c) Sketch, not to scale, of the view from the camera, indicating the ion coordinates x_{ion} and y_{ion} and the ion–fiber distances d_{M} and d_{P}.

and d_{P}, respectively, from the trap center. In the absence of the fibers, the ion is trapped at the trap center. A charged fiber produces a static electric field that, when the fiber is brought near the ion, attracts or repels the ion. Using a CCD camera, we measure the corresponding horizontal shift x_{ion} and vertical shift y_{ion} of the ion in the x-y plane; see Figure 6.1(c). The static electric field produced by a charged fiber also modifies the secular frequencies of the ion's motion in the trap, which we also measure, as we now describe.

6.2 Measurement of ion position and trap frequencies

Figure 6.2(a) shows a CCD image of an ion displaced from the trap center in response to the presence of fiber M, which in this example is positively charged. The ion continuously fluoresces under illumination by a 397 nm Doppler-cooling laser and an 866 nm repumping laser [27]. Both fluorescence from the ion and scattered light from the trap electrodes and inserted fibers pass through an objective and band-pass interferometric filters, after which they are detected by the camera.

To infer the ion position x_{ion} along the trap axis we determine the center of the ion image from the CCD camera with a precision of ± 1 pixel. The camera's pixel conversion was found to be 0.83(4) µm/px; see Subsection 4.5.1. The distances d_{M} and d_{P} between the fiber facets and the trap center are not directly measurable. Indeed, for $d_{\mathrm{M}}, d_{\mathrm{P}} > 180$ µm, which is the case for all data presented in Section 6.5, the fibers are shielded by the radial electrodes and thus not

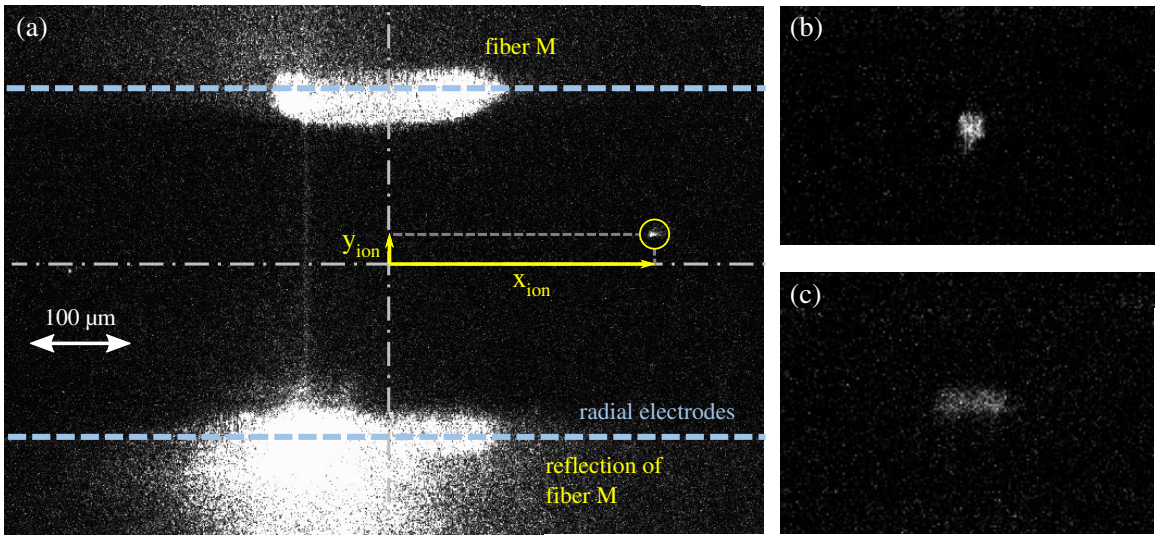

Figure 6.2: CCD camera images. (a) Full field of view, in which an ion (yellow circle) is displaced from the trap center in response to fiber M. The fiber tip is visible below the upper radial electrode. The lower electrode reflects scattered light from fiber M. (b) Close-up view of an unperturbed ion during a measurement of the axial secular trap frequency. (c) Close-up view of an ion that is resonantly driven at the axial secular trap frequency.

visible to the CCD camera. Therefore, we used the calibration and uncertainties described in Subsection 4.5.1.

We furthermore measure the axial secular trap frequency ω_{ax}. We excite the axial mode of the ion's motion by applying a voltage of variable frequency ω_{exc} to one of the endcap electrodes [170]. Scanning ω_{exc}, we are able to distinguish between an unperturbed ion, as in Figure 6.2(b), and an excited ion, as in Figure 6.2(c), and to determine $\omega_{\mathrm{ax}}/2\pi$ within ± 2 kHz.

We note that the same techniques could be applied to measure the ion position along the y-axis and the secular frequencies along both radial axes. However, we do not present such measurements because we are not able to compare them with their simulated counterparts, as will be explained in Section 6.4.

6.3 Simulations of ion position and secular frequencies

Simulations of the total potential energy landscape are performed to estimate the ion's equilibrium position and secular frequencies for arbitrary trap biasing voltages and for any charge state of the fibers according to the homogeneous surface-charge model described in Section 6.1. The total potential is the sum of the RF pseudopotential [59] and the static potentials generated by the endcap electrodes and by the charge densities on the fibers' surfaces. As described in Section 4.2.1, we use finite element analysis software to simulate the relevant electrostatic potentials. In the following simulation, the compensation electrodes are grounded in all cases.

Additionally to the RF potential Φ_{RF} and endcaps $\Phi_{\mathrm{ec,L/R}}$ potentials from Section 4.2.1, we calculate the potential energy $\Phi_{\sigma_{j,k}}$ due to a single fiber region with a surface charge density $\sigma_{j,k}$, $j \in \{\mathrm{M},\mathrm{P}\}, k \in \{\mathrm{f},\mathrm{s}\}$. This potential energy is given by

$$\Phi_{\sigma_{j,k}}(\vec{r}) \;=\; Q\left(\frac{\sigma_{j,k}}{\sigma_0}\right) U_{\sigma_{j,k}}(\vec{r}), \tag{6.1}$$

where $U_{\sigma_{j,k}}(\vec{r})$ is the static electric potential simulated for $\sigma_{j,k} = \sigma_0 = 1\ e/\mu\mathrm{m}^2$, while all electrodes are grounded and all other surface charges densities are set to zero. Finally, the total potential energy $\Phi_{\mathrm{sim}}(\vec{r})$ is given by

$$\Phi_{\mathrm{sim}}(\vec{r}) = \Phi_{\mathrm{RF}}(\vec{r}) + \sum_{i=\mathrm{R,L}} \Phi_{\mathrm{ec},i}(\vec{r}) + \sum_{j=\mathrm{M,P};k=\mathrm{f,s}} \Phi_{\sigma_{j,k}}(\vec{r}). \tag{6.2}$$

For each experimental configuration of the fiber distances d_{M} and d_{P} from the trap center, we successively simulate $U_{\mathrm{RF}}(\vec{r})$, $U_{\mathrm{ec},i}(\vec{r})$, and $U_{\sigma_{j,k}}(\vec{r})$, and we export a two-dimensional map of the corresponding electrical potentials in the x-y plane at $z = 0$. In separate post-processing software, we build the total potential $\Phi_{\mathrm{sim}}(x, y)$ by summing the different contributions scaled by the voltages applied to the trap and for a given set of surface charge densities.

In Figure 6.3, we consider our setup (cf. Section 6.1) to show examples of simulated total potentials for neutral, negative, and positive charge states of fiber M, where $d_{\mathrm{M}} = 0.5\,\mathrm{mm}$ and fiber P is held neutral. When fiber M is negative, the ion is attracted by the fiber (Figure 6.3(b), and its axial potential is stiffened, that is, the curvature is steeper at the potential minimum. On the other hand, when fiber M is positive, the ion is repelled. In the example of Figure 6.3(c), the repulsive force is so large that it splits the axial potential generated by the endcaps into a double-well, as also observed in [189].

For comparison with measured quantities, we determine the axial equilibrium position and the axial secular frequency of the ion for each simulation. As a starting point, we take the mean position of all points for which the potential lies in the (lowest) first percentile. For a circular area with a radius of $50\ \mu\mathrm{m}$ around this minimum, the potential is fitted with a two-dimensional parabolic curve. Translations along x and y, curvatures of the two semi-axes, and a rotation of these semi-axes are used as free parameters for this two-dimensional fit. The ion position is given by the value for the translation along x, and its axial secular frequency is extracted from the fitted curvature of the minor semi-axis.

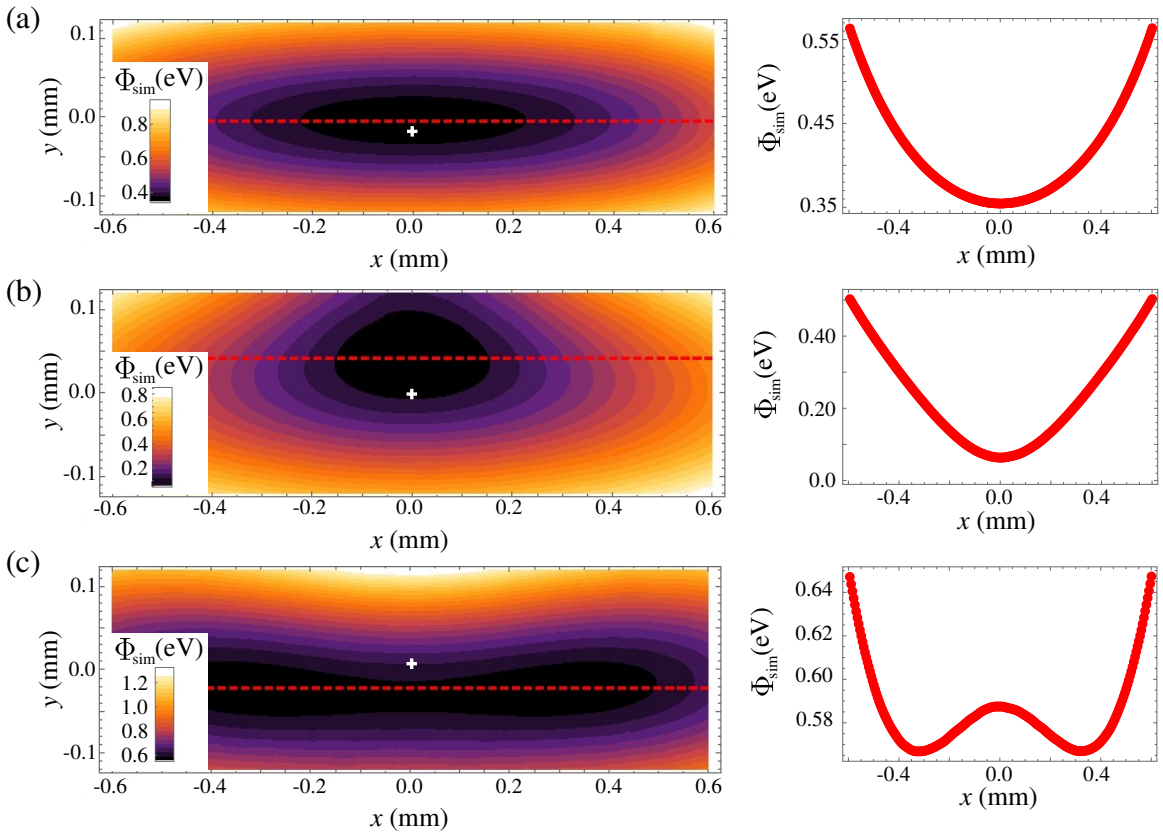

Figure 6.3: Comparison of simulated potential maps in the x-y plane for different surface charges on fiber M while fiber P is held neutral. (a) $\sigma_{\mathrm{M,f}} = \sigma_{\mathrm{M,s}} = 0$, (b) $\sigma_{\mathrm{M,f}} = \sigma_{\mathrm{M,s}} = -4\sigma_0$, (c) $\sigma_{\mathrm{M,f}} = \sigma_{\mathrm{M,s}} = +4\sigma_0$, where $\sigma_0 = 1\ e/\mu\mathrm{m}^2$. Line cuts are taken through the potential maps along dashed lines which intersect the potential minima and are plotted in the right column. Fiber M is located above the upper edge of these maps at a distance of $d_{\mathrm{M}} = 0.5\,\mathrm{mm}$ from the trap center, while fiber P is $d_{\mathrm{P}} = 1.6\,\mathrm{mm}$ below the trap center depicted as a white cross.

6.4 Patch potential

By simulating each experimental fiber configuration using the methods of previous section, one should be able to find a set of surface charge densities $\{\sigma_{\mathrm{P,f}}, \sigma_{\mathrm{P,s}}, \sigma_{\mathrm{M,f}}, \sigma_{\mathrm{M,s}}\}$ that reproduces the results of the measurements discussed in Section 6.2.

First, however, the simulations should be validated independently of the fibers' influence. To this end, the fibers were maximally retracted to minimize their influence on the ion. With the left and right endcap voltages set to be equal, $V_{\mathrm{ec,L}} = V_{\mathrm{ec,R}}$, the mean voltage $V_{\mathrm{ec,M}} = (V_{\mathrm{ec,L}} + V_{\mathrm{ec,R}})/2$ of the endcaps was tuned to compare measurements of the axial secular trap frequency ω_{ax} with the simulations. As presented in Section 4.4.2, we needed to include a value for w_0^2 in Equation (4.3) for our simulations to find an agreement with the steeper confinement in the measurements. We assumed that this discrepancy is due to charged patches on the radial electrodes.

These patches significantly affect the equilibrium position of the ion and its secular frequency. Since we aim to determine the charges on the fibers by precise measurement of these values, we need to understand quantitatively the role of this so-called patch potential. As the ion is displaced along the trap axis during our measurements, we need to consider the perturbation along the trap axis by estimating the patch potential $U_{\mathrm{patch}}(x)$. We then add this estimation to the simulated potential, such that the total potential including the patch effect along x is given by $\Phi(x, y) = \Phi_{\mathrm{sim}}(x, y) + U_{\mathrm{patch}}(x)$.

To reconstruct $U_{\mathrm{patch}}(x)$, we measure the ion position $x_{\mathrm{exp}}(V_{\mathrm{ec,D}})$ as a function of the endcap voltage difference $V_{\mathrm{ec,D}} = V_{\mathrm{ec,L}} - V_{\mathrm{ec,R}}$. Here, we maintain a constant mean endcap voltage $V_{\mathrm{ec,M}} = 1\,\mathrm{kV}$. The voltage difference $V_{\mathrm{ec,D}}$ is scanned such that the ion moves over the full width of the CCD field of view ($0.8\ \mathrm{mm}$). We then simulate the ion position x_{sim} in the absence of any patch potential. For each voltage configuration $V_{\mathrm{ec,D}}$, we assume that the measured total potential along the x-axis, $\Phi(x)$, composed of the simulated potential $\Phi_{\mathrm{sim}}(x)$ and the patch potential, can be approximated close to the ion by a harmonic potential:

$$\Phi(x) = \Phi_{\mathrm{sim}}(x) + U_{\mathrm{patch}}(x) = \frac{1}{2} M \omega_{\mathrm{exp}}^2 (x - x_{\mathrm{exp}})^2, \tag{6.3}$$

with the simulated harmonic potential around x_{sim}

$$\Phi_{\mathrm{sim}}(x) = \frac{1}{2} M \omega_{\mathrm{sim}}^2 (x - x_{\mathrm{sim}})^2. \tag{6.4}$$

At the measured equilibrium position x_{exp}, the derivative of the total potential, $\Phi'(x_{\mathrm{exp}})$, vanishes:

$$\Phi'(x_{\mathrm{exp}}) = \Phi'_{\mathrm{sim}}(x_{\mathrm{exp}}) + U'_{\mathrm{patch}}(x_{\mathrm{exp}}) = 0 \tag{6.5}$$

$$U'_{\mathrm{patch}}(x_{\mathrm{exp}}) = -M \omega_{\mathrm{sim}}^2 (x_{\mathrm{exp}} - x_{\mathrm{sim}}) \tag{6.6}$$

The position discrepancies between experiment and simulation for each measured voltage configuration $V_{\mathrm{ec,D}}$, $\Delta x(V_{\mathrm{ec,D}}) = x_{\mathrm{exp}}(V_{\mathrm{ec,D}}) - x_{\mathrm{sim}}(V_{\mathrm{ec,D}})$, are then used to recover $U_{\mathrm{patch}}(x)$ modulo a constant by numerically integrating over the measured position $x_{\mathrm{exp}}(V_{\mathrm{ec,D}})$:

$$U_{\mathrm{patch}}(x) = -M \omega_{\mathrm{sim}}^2 \int_0^x \Delta x(V_{\mathrm{ec,D}}(x_{\mathrm{exp}})) dx_{\mathrm{exp}}. \tag{6.7}$$

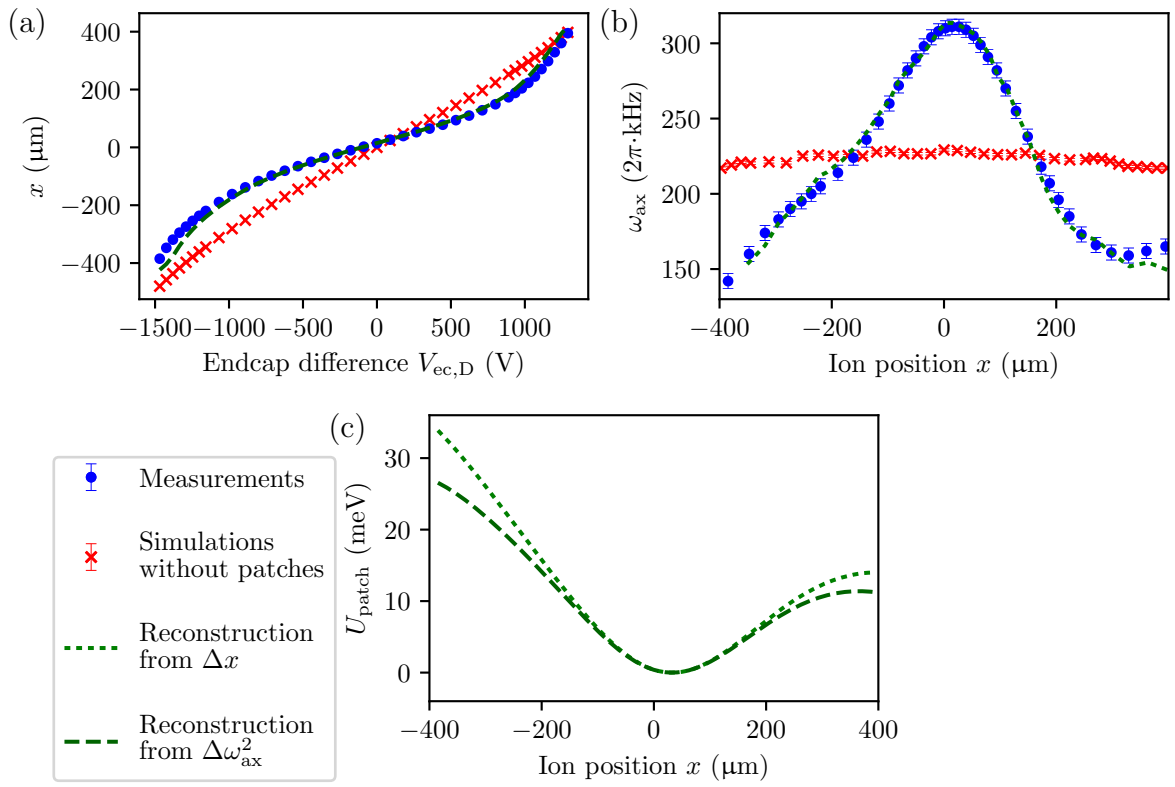

Figure 6.4: Reconstruction of the patch potential $U_{\mathrm{patch}}(x)$. (a) Measured and simulated ion positions x (blue points and red crosses, respectively) as a function of endcap voltage difference $V_{\mathrm{ec,D}}$. (b) Measured and simulated axial frequencies (blue points and red crosses, respectively) as a function of ion position x. (c) Reconstructed patch potential from the discrepancies of the ion positions (green dotted line; see (a)) and of the axial secular trap frequencies (green dashed line; see (b)). For the patch potential reconstruction based on trap frequencies, the corresponding ion positions have been simulated and plotted in (a) for comparison with the measured data, while for the patch potential reconstruction based on ion positions, the trap frequencies have been simulated and plotted in (b).

Alternatively, after differentiating equation Equation (6.3) twice,

$$\Phi''(x) = \Phi''_{\mathrm{sim}}(x) + U''_{\mathrm{patch}}(x) \tag{6.8}$$

$$M\omega^2_{\mathrm{exp}} = M\omega^2_{\mathrm{sim}} + U''_{\mathrm{patch}}(x), \tag{6.9}$$

we can use the discrepancy between the squared secular trap frequencies

$$\Delta\omega^2(V_{\mathrm{ec,D}}) = \omega^2_{\mathrm{exp}}(V_{\mathrm{ec,D}}) - \omega^2_{\mathrm{sim}}(V_{\mathrm{ec,D}}) \tag{6.10}$$

to determine the curvature of the patch potential U''_{patch} at $x_{\mathrm{exp}}(V_{\mathrm{ec,D}})$. After one integration over the position, the integration constant is chosen such that the simulated equilibrium position without any endcap voltages ($V_{\mathrm{ec,M}} = 0$) matches the one observed experimentally. Following a second integration, we again end up with the reconstructed patch potential.

The two reconstruction methods produce patch potentials with nearly identical structure, as shown in Figure 6.4. For both methods, the starting point for integration is the point at which the simulated and measured ion positions are equal, at $x = 30$ µm. Integration then proceeds outwards stepwise, such that any errors will accumulate, as can be seen in Figure 6.4(c), where the discrepancy between the two reconstruction methods is greatest at $x = \pm 400$ µm. To understand whether these deviations are significant, we extracted the axial positions and secular trap frequencies from the total simulated potentials $\Phi(x, y) = \Phi_{\mathrm{sim}}(x, y) + U_{\mathrm{patch}}(x)$ for both reconstructions. For the reconstruction based on the secular trap frequency, the corresponding axial position is plotted together with the measured and simulated ion position values in Figure 6.4(a). For the reconstruction based on ion position, the corresponding secular trap frequency is plotted together with the measured and simulated values in Figure 6.4(b). Mean discrepancies of both positions and frequencies and of both reconstruction methods are on the order of measurement errors (0.8 µm and 2 kHz) and simulation errors (0.5 µm and 2 kHz), indicating that variations in the reconstructed patch potentials seen in Figure 6.4(c) are not significant. In the following, reconstructions are based on the mean of the two reconstructed patch potentials, with which we observe a mean discrepancy of 4.8 kHz compared to the measured secular trap frequencies. For the reconstructed ion position, the error depends strongly on the actual position. In the center the deviations are only about 1 µm, but for larger displacements from the trap center, the discrepancies between reconstruction and measurement are up to 15 µm due to errors accumulated by the integration for the reconstruction. This characteristic is taken into account in further reconstructions by a position-dependent error.

We note that the reconstruction method described above depends on tuning the endcap voltages and is thus only valid along the trap axis. We are unable to use the same approach to evaluate data on ion position and secular frequency measured along the radial axis y. It is in principle possible to extend the reconstruction method to the radial direction, since we can displace the ion along the y-axis using another set of static electrodes. However, a systematic mapping of $U_{\mathrm{patch}}(x, y)$ in the x-y plane is challenging because when the ion is displaced from the trap axis, it is affected by micromotion and often fails to remain stable or trapped. Therefore, we limit ourselves to a one-dimensional reconstruction of the patch potential along the trap axis. Moreover, for our trap geometry, the axial secular frequency is the weakest and thus the most sensitive to the fiber position, independent of the sign of the fibers' surface charges. As a result, information in the radial direction is not essential for estimating the charge state of the fibers, although knowledge about $U_{\mathrm{patch}}(x, y)$ in two dimensions would help to refine this estimation.

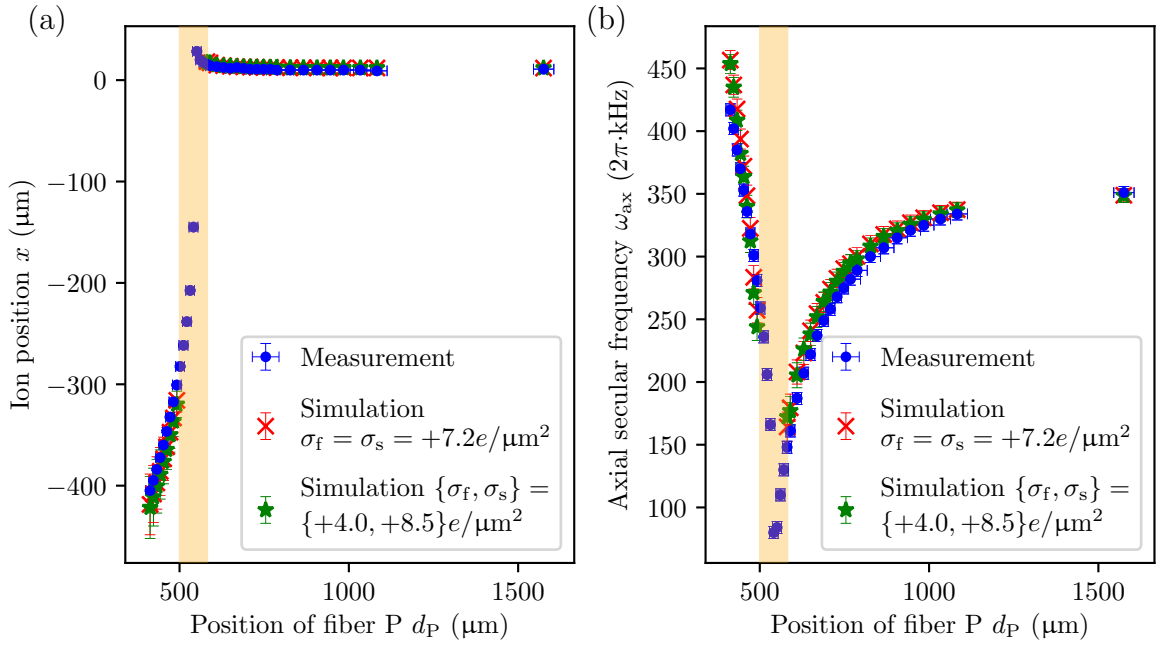

Figure 6.5: (a) Ion position x_{ion} and (b) axial frequency ω_{ax} as a function of d_{P}, the position of fiber P, both measured (blue points) and simulated for $\sigma_{\text{P,f}} = \sigma_{\text{P,s}} = +7.2\ e/\mu\text{m}^2$ (red crosses) and for $\{\sigma_{\text{P,f}}, \sigma_{\text{P,f}}\} = \{+4.0, +8.5\}\ e/\mu\text{m}^2$ (green stars). The orange shaded area indicates the transition between a single-well and a double-well axial potential. The simulations were omitted in this region due to the anharmonic potential (see main text). Measurement error bars represent one standard deviation. Simulation error bars represent the uncertainties of the fit to the reconstructed potential and the errors found for the reconstruction in Section 6.4.

6.5 Determining surface charge distribution of our fibers

Finally, we turn to the determination of surface charge densities on the fibers. We will present two cases, both from our experimental setup, that are particularly relevant for cavity-QED experiments in which an ion is trapped inside a fiber-based cavity. First, we examine the situation of a fiber that was found to be positively charged after the system was first assembled, evacuated, and used to trap ions. Second, we discuss the case of an almost neutral fiber, which offers favorable conditions for building short fiber cavities that result in minimal disturbance of the ion's position.

6.5.1 Positively charged fiber

Figure 6.5 shows the measured axial position and secular frequencies of the ion as a function of fiber P's position. Here, fiber M remains retracted at $d_{\text{M}} \approx 2.0$ mm and has no influence on the ion. We verify this claim by translating fiber M to $d_{\text{M}} \approx 1.6$ mm, which yields no measurable shifts in either the ion position or its axial frequency. We conclude that fiber M's charges do not affect this measurement and set $\sigma_{\text{M,f}}$ and $\sigma_{\text{M,s}}$ to zero in the simulations.

As fiber P is brought towards the ion from a fully retracted position ($d_{\text{P}} \approx 1.6$ mm), the axial frequency is first observed to decrease, while the ion remains close to the trap center

but is slightly shifted away from the fiber. At $d_{\mathrm{P}} \approx 0.55$ mm, the axial frequency reaches a minimum, and as the fiber is moved closer to the trap center, the axial frequency increases, while the ion is now significantly displaced from the trap center. This scenario corresponds to a positively charged fiber. The static potential of the approaching positive fiber first relaxes the axial potential that is provided by the endcaps, and as the fiber is not exactly centered with respect to the ion, the fiber displaces the ion along the x-axis. As the positively charged fiber is brought even closer to the trap center, the repulsive force splits the axial potential into a double-well potential. The transition between the single- and double-well cases happens at $d_{\mathrm{P}} \approx 0.55$ mm. For the double-well case, either local minimum can be stably occupied in experiments. In practice, the ion was reliably found on the side with $x < 0$.

To determine the charge state $\{\sigma_{\mathrm{P,f}}, \sigma_{\mathrm{P,s}}\}$ of fiber P, the ion's positions and axial frequencies are simulated for the measured fiber's positions and compared to the measurements. By adjusting the charge distribution of the fiber used in the simulations, the agreement between simulated and measured values can be optimized, that is, the discrepancies between simulation and measurement for ion position and axial frequency can be minimized. For the purpose of this optimization, the position and frequency discrepancies are normalized so that a single value can be derived, which is then minimized, as we now describe.

We simulate the total potential $\Phi(x, y) = \Phi_{\mathrm{sim}}(x, y) + U_{\mathrm{patch}}(x) + \Phi_{\sigma_{\mathrm{P,s}}}(x, y) + \Phi_{\sigma_{\mathrm{P,f}}}(x, y)$ for all measured positions of fiber P, using the trapping voltages of the experiment. In contrast to the applied voltages described in Section 6.4, here we raised the axial confinement by applying a mean endcap voltage of $V_{\mathrm{ec,M}} = 1.5$ kV. For the following simulations, fiber P is positioned at $x = 10\ \mu\mathrm{m}$ which is within the uncertainty with which we can position the fiber at the origin in our experimental setup (c.f. Section 6.1)[3]. From these reconstructed total potentials, we extract the simulated positions and axial frequencies. We omit a reconstruction around the transition region from a single to a double well because a harmonic description is not valid in this regime; see the orange shaded area in Figure 6.5. For the double well, we then selected the minimum in which the ion was observed. For each simulated position and axial frequency, we calculated the discrepancy to the measured value. Each discrepancy was weighted by the sum of the corresponding measurement, simulation, and reconstruction errors, where all errors represent one standard deviation, and where the error of the reconstructed position was considered to be position-dependent, as described in Section 6.4. This weighting serves to normalize the discrepancy, so that a value of one means that the simulation deviates by one standard deviation from the measurement. With this normalization, the squares of positions and axial frequencies at each fiber position can be summed up to a single residual, which is used to find the charge densities $\{\sigma_{\mathrm{P,f}}, \sigma_{\mathrm{P,s}}\}$ via continuous optimization.

As the least-squares optimization code often converged to local minima due to the noisy reconstruction, residuals were calculated over a two-dimensional array of surface charge densities $\{\sigma_{\mathrm{P,f}}, \sigma_{\mathrm{P,s}}\}$. Here, a correlation between the surface charge densities $\sigma_{\mathrm{P,f}}$ and $\sigma_{\mathrm{P,s}}$ was observed, indicating that removing charges on the fiber facet could be compensated for by adding charges to the side, or vice versa. Nevertheless, the global minimum was found over the 2D charge-density array. Using charge densities close to this global minimum as initial parameters, the least-squares optimization code converged reproducibly to $\sigma_{\mathrm{P,f}} = +4.0\ e/\mu\mathrm{m}^2$ and $\sigma_{\mathrm{P,s}} = +8.5\ e/\mu\mathrm{m}^2$. At this minimum, a mean residual of 3.0 for each measured point was

[3]Simulations were carried out for fiber positions at $x = \{0, 5, 10, 15\}\ \mu\mathrm{m}$ and the best agreement between measurements and simulations was chosen.

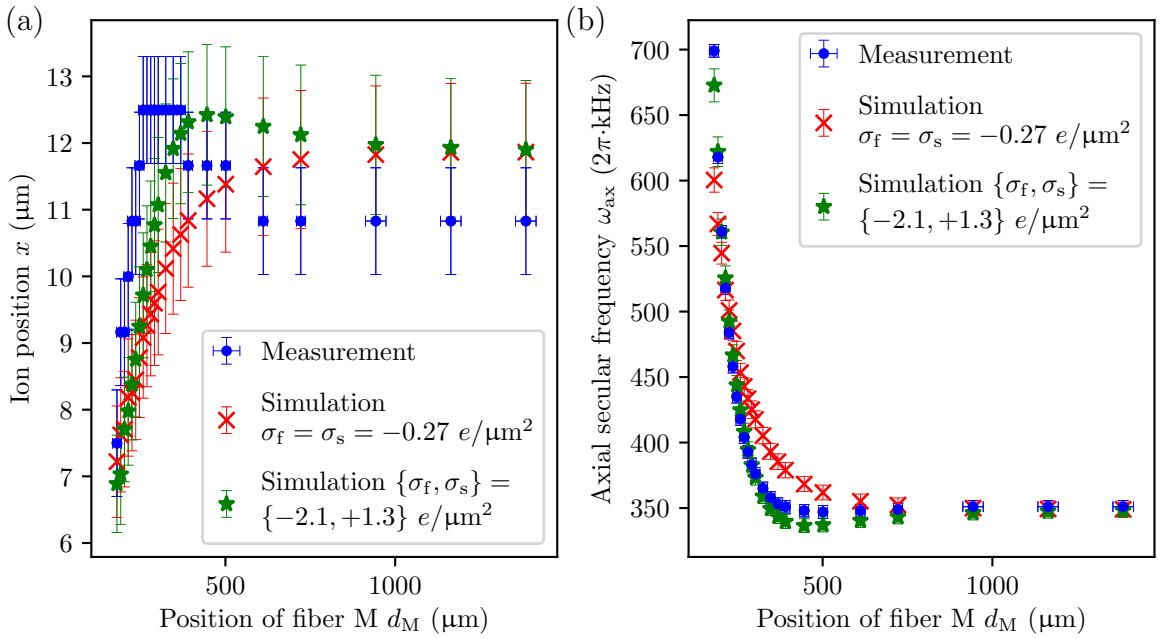

Figure 6.6: (a) Ion position x_{ion} and (b) axial frequency ω_{ax} as a function of d_M, the position of fiber M, both measured (blue points) and simulated for $\sigma_{P,f} = \sigma_{P,s} = -0.27\ e/\mu m^2$ (red crosses) and for $\{\sigma_{M,f}, \sigma_{M,s}\} = \{-2.1, +1.3, +4.0, +8.5\}\ e/\mu m^2$(green stars). Measurement error bars represent one standard deviation. Simulation error bars represent the uncertainties of the fit to the reconstructed potential and the errors found for the reconstruction in Section 6.4.

calculated, meaning that the discrepancies between reconstruction and measurement were three times larger than the errors expected from the measurement, simulation and reconstruction. Positions and frequencies corresponding to these optimized surface-charge values are plotted in Figure 6.5. This analysis was also carried out for a single charge density on the fiber's surface, that is, for the constraint $\sigma_f = \sigma_s$. A value of $\sigma_f = \sigma_s = 7.2\ e/\mu m^2$ was found with a mean residual of 3.05 standard deviations. This result underscores the range of possible surface charge densities which are able to reproduce the measured data with similar agreement.

6.5.2 Almost neutral fiber

In coupling a trapped ion to an optical cavity, one has to take into account the electric field generated by any surface charges on the cavity mirrors, and it is generally desirable to minimize the effect of this field on the trapping potential. In this regard, fiber-based Fabry-Pérot cavities present a particular challenge due to the small distances (typically a few hundred microns) between ion and dielectric mirror surfaces. In the linear ion trap used here, trapped ions were highly sensitive to charges on the fibers due to the low frequency of axial confinement (see Section 6.1). Ideally, one would like to work without charges on the fibers, but in practice this is challenging. A viable alternative consists of obtaining distributions of positive and negative charges that almost cancel each other's effects at the location of the ion.

We were able to modify the charge distribution of fiber M to achieve such a cancellation;

the method will be discussed briefly in Section 6.6. In Figure 6.6, the blue points show the measured axial positions and axial frequencies of the ion as a function of d_{M} while fiber P is kept retracted at $d_{\mathrm{P}} \approx 1.6$ mm. When fiber M is brought towards the trap center, the ion remains close to the trap center but is first shifted slightly away from the fiber, then slightly towards it. Its axial frequency increases, indicating that the ion sees a negative charge distribution overall. Moreover, in contrast to the situation described in Section 6.5.1, fiber M can be brought within 200 µm of the ion while the ion remains within 4 µm of the trap center.

Following the approach described for the positively charged fiber, we optimize the parameters $\{\sigma_{\mathrm{M,f}}, \sigma_{\mathrm{M,s}}\}$ to obtain the best agreement between simulations and data. Here, fiber M's position was set to $x = 5$ µm following simulations over a range of positions within the experimental positioning uncertainty, as explained in Section 6.5.1. In the simulations, for the retracted fiber P, we set $\{\sigma_{\mathrm{P,f}}, \sigma_{\mathrm{P,s}}\} = \{+4.0, +8.5\}\ e/\mu\mathrm{m}^2$, as determined previously. The least-squares optimization code converges to surface charge densities of $\{\sigma_{\mathrm{M,f}}, \sigma_{\mathrm{M,s}}\} = \{-2.1, +1.3\}\ e/\mu\mathrm{m}^2$ for fiber M with a residual mean discrepancy of 1.5. Again, the reconstruction was also optimized for a single surface charge density. Here, a minimum mean residual of 4.9 standard deviations was found for $\sigma_{\mathrm{f}} = \sigma_{\mathrm{s}} = -0.27\ e/\mu\mathrm{m}^2$. The significantly higher discrepancy between simulation and experiment in this case indicates the need for different surface charges densities on the fiber's facet and side to account for the measured data properly.

When fiber M is close to the trap center, the ion is mostly influenced by the negative charges on the fiber facet and reacts accordingly. However, when fiber M is far away, the positive and negative charges roughly compensate for one another, perturbing the ion minimally: Only when d_{M} is less than 0.5 mm does the ion start to respond via its position and axial frequency to a displacement of the fiber. In contrast, small displacements of fiber P can be detected via shifts of the ion's axial frequency even when the fiber is fully retracted ($d_{\mathrm{P}} \approx 1.6$ mm).

6.6 Discussion

We have described a method to model the surface charge densities on optical fibers next to a trapped ion in a way that reproduces experimental results. In this work, we have shown a detailed analysis for one patch potential configuration in Section 6.4 and for two surface charge distributions of fibers in Section 6.5. Furthermore, following these methods, for several additional charge states of the fibers and patch potentials on the radial electrodes, we were able to estimate a set of charge densities ranging from -10 to +50 $e/\mu\mathrm{m}^2$.

Comparing measurements of the ion's position and its axial secular frequency, error bars for the charge densities were determined via least-squares optimization, but the reconstructions for the two fibers had final mean discrepancies of 1.5 and three standard deviations with respect to the measurements. Two main limitations, described below, prevent us from determining the charge densities with better agreement between reconstruction and measurement.

6.6.1 Limits of the method

First, the model we use to describe how the charges are distributed over the fibers does not account for complex structures: We assume that there is a homogeneous distribution of charges across the fiber facet and a second homogeneous distribution along the fiber side. This choice

is dictated by simplicity and symmetry in the absence of better knowledge of the actual charge distribution. An even simpler choice would have been a single homogeneous distribution over the complete fiber surface. This would have worked reasonably well for the positive fiber P, as seen in Figure 6.5, but for fiber M, our two-parameter approach was essential to account for the data, as seen in Figure 6.6. One could think of refining the model by dividing the exposed area into additional zones, each carrying a different homogeneous density, or by parametrizing non-homogeneous distributions. However, without physical justification to guide these choices, one would end up with a wide parameter space to optimize, which would be time- and resource-consuming.

Second, we suffer from imperfect knowledge of the patches described in Section 6.4. Although we were able to gain information that allowed us to account for the effect of the patch along the x-axis, this reconstruction is limited, particularly because we were not able to characterize the patch potential along the radial axis y. Not only could we have used measurements of the same quantities in the radial direction for a reconstruction, but also we could have combined the analyses of measurements and simulations along the two axes to gain more precision of the determined surface charge densities.

6.6.2 Temporal stability of charges

The charge distributions in our setup shift over time, affecting the timescales over which measurements are reproducible. Here, we discuss those timescales and how they are accounted for in our measurements.

Recall that in Section 6.5.2, the charge distribution of fiber M had been modified to achieve a near-neutral state. This modification was the result of a laser-based procedure that we have recently developed and investigated in which photoelectrons are created by the illumination of trap electrodes with around $30\,\mathrm{mW}$ of $393\ \mathrm{nm}$ laser light. During this illumination, these electrons can be influenced by applied voltages on particular electrodes, after which the charge states on both the fibers and patches are observed to shift. The patch potentials on the electrodes are found to evolve on a time scale of a few minutes, stabilizing after about one hour, presumably due to charge rearrangement. The charge state of the fibers initially stabilizes within a few hours, but continues to drift on another, much slower time scale.

This procedure provides us with the flexibility to tune the charge state of the fibers to be either more negative or more positive. However, one shortcoming is that the charges on the fibers continue to drift. Fiber P reaches its final charge state within about one week, whereas fiber M needs about one day. These different time scales may be due to the coatings of the fibers, which are more than $10\ \mathrm{mm}$ behind the fiber facet (Section 6.1): Fiber P has an insulating coating, whereas fiber M has a metallic coating, which could shorten the time scale of charge rearrangement. Moreover, if the fibers are translated via their nanopositioning stages before the final charge state has been reached, the charge on the fibers shifts. Experimentally, we address this by waiting for the charge state of both fibers to stabilize before carrying out measurements such as those presented in Figure 6.5 and Figure 6.6. We have verified that after a sufficient waiting time, translation of the fibers does not affect the measurement results within error bars.

6.6.3 Possible applications

In spite of these limitations, our method provides a reconstruction of the patch potential along the ion-trap axis and an estimation of the surface charge density of dielectrics. Whereas patch potentials and electric fields can be determined by only measuring the ion, the estimation of an in-vacuum element's charge densities relies here on the ability to displace that element relative to the ion. This ability ensures that changes of the ion's potential are attributed only to displacements of the charge densities on the in-vacuum element.

In cavity QED setups involving trapped ions and optical cavities based on dielectrics, building short cavities to maximize the ion-cavity coupling rate is challenging because the mirrors tend to carry charges. The ability to assess the charge densities on the fibers and their evolution will aid in the development of procedures to discharge the fibers. Furthermore, knowledge of the typical charge densities that can be expected under a given set of conditions will enable targeted approaches to improve experimental setups, such as by incorporating elements to reduce the adverse effects of charges on trapped ions. These considerations also apply to cavity QED setups using Rydberg atoms due to their large sensitivity to electric fields [190, 191].

Our method is relevant for the field of trapped ions in general, where systems designed for scalable quantum computing or quantum simulation can benefit from component miniaturization. In a microfabricated trap, ions can be stored a few tens of micrometers away from the trap surfaces, which may generate spurious electric fields [34, 192]. Such fields have been found to be correlated to ion heating [193]. Efforts are also underway to integrate optical elements required to address ions with laser beams [194], to collect ions' fluorescence [195–197], or to build fiber-based cavities [124, 114]. While these elements are fixed with respect to the ion trap, more complex future tasks, such as selective addressing or imaging, may benefit from movable mirrors, lenses, fibers, or waveguides placed close to ions. Understanding the charge state of these elements is desirable in order to minimize detrimental effects of the corresponding parasitic fields, such as trapping instability, excess micromotion or anomalous heating, in view of optimizing the quantum operations for which a given device was designed. More broadly, our method can be valuable for any experiment where charging effects or local electric fields on surfaces need to be understood or mitigated.

Chapter 7

Fiber cavities in the concentric regime

The measurements presented in the previous chapter have shown how challenging it is to bring ions close to dielectrics like fiber mirrors. Charges on the fibers disturb the ion's potential, so that a minimum ion-dielectric distance and therefore a minimum cavity length is necessary, although the exact length will depend on the trap design. As explained in Chapter 2, a concentric fiber cavity would improve the ion-photon coupling strength, just as a concentric design is the basis for the existing cavity experiment in our group. Here, we want to investigate if it possible to enhance the cooperativity, a figure of merit for our quantum interface, by accessing the concentric regime of fiber cavities. The following sections are also in preparation for submission as a journal article [198].

7.1 Finesse measurement

As defined in Equation (3.11), the finesse of a cavity, is determined by linewidth $\delta\nu$ of the cavity resonance and the free spectral range (FSR) $\nu_{\mathrm{FSR}} = c/2L$, with c the speed of light and L the cavity length. In practice, to determine the finesse of our fiber cavity, we thus measure both the linewidth and the corresponding cavity length.

We build a fiber cavity out of a PC fiber and a MM fiber, whereby both radii of curvature are $R = 215(5)$ which were determined by fitting profiles with a 2D elliptical sphere (Section 3.2)). The light of a diode laser was couple into the PC fiber, and the transmission was detected on the fast photodiode $\mathrm{PD}_{\mathrm{trans}}$; an experimental setup as presented in Subsection 3.3.1. For each cavity length, we optimized the MM fiber alignment for the highest transmission peak of the fiber cavity. With the built-in piezo of the six-axis stage, we then scanned the MM fiber position and thus the length of the cavity only over the highest resonance. We expected that this resonance corresponded to the TEM 00 transverse mode. The signal of $\mathrm{PD}_{\mathrm{trans}}$ was recorded by an oscilloscope and saved to our computer. As we knew the frequency of the modulation, that we applied to the laser that probed the cavity (typically tens of megahertz), we could calibrate the time axis of the oscilloscope trace in order to convert it to frequency units. By fitting a triple Lorentzian curve to the trace of a carrier peak with two sidebands (see inset Figure 3.11), we extracted the linewidth of the cavity resonance in terms of frequency. At each cavity length, the transmission peaks were recorded five times in order to determine an statistical error.

For a determination of the cavity length, the diode laser acted as a reference; see Figure 3.11.

The Ti:sapph laser with a wavelength ranging from 900 to $920\,\mathrm{nm}$ was also coupled into the fiber cavity. The frequency of the Ti:sapph laser was then scanned and measured by the wavemeter each time the resonant peaks of the two lasers overlapped in the transmission spectrum of the fiber cavity ("double resonance"). The difference in frequency between two neighboring double resonances corresponds to the FSR of the cavity. From the FSR, the cavity length is calculated. Using this process, the cavity length is determined for eleven cavity lengths distributed over the whole range of measured cavity lengths $50\,\mu\mathrm{m} < L < 420\,\mu\mathrm{m}$. For each finesse measurement, the position of the stepper motor was recorded, too. Fitting the eleven measured cavity lengths to the positions of the stepper motor by a linear function results in a calibration of cavity length with a uncertainty $\Delta L < 1\ \mu\mathrm{m}$ for all positions.

The linewidth was measured for about 70 different cavity lengths up to $415\ \mu\mathrm{m}$. With the calibrated stepper motor positions, we calculated for each of these linewidths the finesse, plotted in Figure 7.1 (blue points). The determined finesses from $L = 120\,\mu\mathrm{m}$ to $L = 380\,\mu\mathrm{m}$ (omitting the decreased finesses discussed in the next paragraph) fall within the range $90\,000 < \mathcal{F} < 110\,000$. For this range, assuming that clipping losses do not play a role, we find absorption and scattering losses of $\mathcal{L}_M = (\frac{2\pi}{F} - \mathcal{T}_{\mathrm{PC}} - \mathcal{T}_{\mathrm{MM}})/2 = 23(3)$ ppm for each mirror; transmission as described in Section 3.2.3.

For cavities ranging from $L = 320\ \mu\mathrm{m}$ to $L = 380\ \mu\mathrm{m}$, we observed spots of decreased finesse, as expected from crossings of different TEM modes [150]. Another decrease of finesse was measured in the confocal regime between $210\ \mu\mathrm{m} < L < 220\ \mu\mathrm{m}$, as indicated by the yellow area in Figure 7.1. This region is exactly where no stable Gaussian modes are expected because the cavity length is in between the two radii of curvature of the two mirrors; see Equation (3.8). Actually, both mirrors were slightly elliptically shaped, and fits of each mirror profile showed main axes ranging from $R = 200$–$225\ \mu\mathrm{m}$ depending on the size of the region of interest, similar as illustrated in Figure 3.7. Therefore due to a random rotation of these main axes that is, the rotation of the fiber mirrors with respect to each other, stable modes could still be formed, but are heavily deformed and with enhanced clipping losses, i.e., low finesse.

Interestingly, eight data points with $L < 100\ \mu\mathrm{m}$ show a finesse of $115\,000 < \mathcal{F} < 130\,000$. Such an increased finesse for short cavities is also found in Figure 7 of [115]. One possible hypothesis that could explain such behavior would be: Photons scattered out of the cavity mode could be recaptured by the mirrors, the diameter of which is much greater than the cavity length. For a cavity length of $L = 50\ \mu\mathrm{m}$ with a finesse $\mathcal{F} \approx 130\,000$ just less than one quarter of the 46 ppm cavity losses would be needed to be recaptured. An interesting fact for the cavity configuration showing this increased finesse is that the Rayleigh length of the Gaussian cavity mode is larger than half the cavity length. Furthermore, the mirror coating was not optimized for a certain radius of curvature, but showed just a few ppm of losses for substrate mirrors of the same coating run; see Section 3.2.3. Using these facts, further measurements of cavities, shorter than the half of the Rayleigh length, with different radii of curvatures, up to hybrid cavities (see Subsection 3.3.2), could give more evidence for the hypotheses presented previously, or show new correlations of the measured finesse. As for our measurements we are interested in the concentric regime, we have not investigated this behavior further.

To compare our measured data, we plotted the expected finesse, calculated with the model of clipping losses introduced in Equation (3.13) of Subsection 3.1.3; see the green filled area in Figure 7.1. The upper and lower limits were calculated with the radii of curvature $R = 210\ \mu\mathrm{m}$ and $R = 220\ \mu\mathrm{m}$, respectively, the mirror losses as just discussed, and the effective

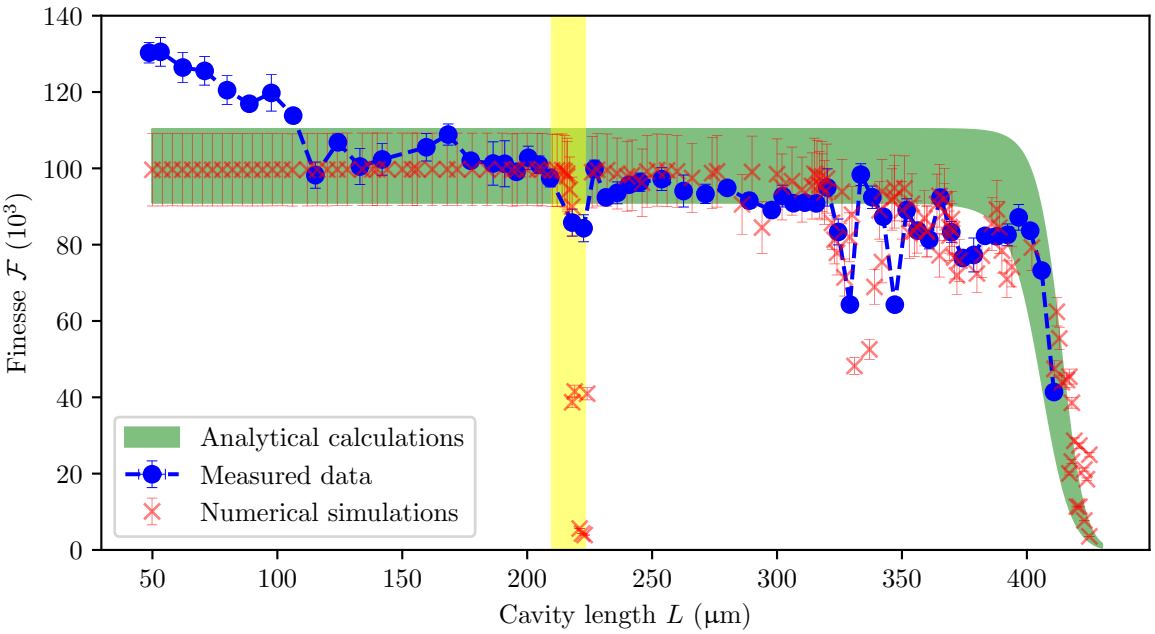

Figure 7.1: Finesse as a function of the cavity length. The blue circles show the measured finesse determined by length and linewidth measurements of a single fiber cavity. For cavities up to $L = 400$ µm, the finesse remains between 90 000 and 110, 000, with only two exceptional regions. The first region, around $L = 215$ µm, can be explained by the instability of the cavity due to the unequal radii of curvature for the two mirrors and the mirror ellipticity. The second region, where a significant reduction of finesse is observed at $L \approx 330, 350, 380$ µm, corresponds to a region of TEM mode frequency crossings as predicted in [150]. The green area is the calculated finesse of a symmetric cavity using the model of Equation (3.13), with mirror losses $\mathcal{L}_M = 23(3)$ ppm per mirror, radius of curvatures $R = 215(5)$ µm, and effective useful diameters $D = 67.5(25)$ µm. This calculated finesse shows good agreement in the near-concentric regime and demonstrates that the steep decrease in finesse of cavities longer than 400 µm can be attributed to clipping losses. The red crosses represent simulations (introduced in Subsection 7.2) based on the fiber surface profiles obtained after CO_2 ablation, as performed in [115]. The simulations additionally confirm both the instability region and the mode-crossing by revealing a reduced finesse in these regions.

useful diameter $D = 67.5(25)$ µm. The effective useful diameter was set by hand for the best agreement with the measured data. With the exception of the high finesse values for short cavities that we have just discussed, this model already shows agreement with the measured finesses within the error bars.

7.2 Optical FFT simulations

For a more detailed theoretical simulation of the measured data, we also carried out a numerical simulation of the cavity light-modes as described in [115]. We used the MATLAB code of [115], which was just slightly modified. The code was based on the MATLAB toolbox OSCAR (Optical Simulation Containing Ansys Results) [199] which uses the fast Fourier transform

(FFT) to simulate the steady state electric fields for cavities with arbitrarily shaped mirrors. During our collaboration with Prof. Jakob Reichel's research group, our fiber-mirror profiles were recorded with the same profilometer as used for the data of [115]. However, instead of averaging over 120 profiles as in [115], we captured only two profiles directly after mirror ablation. To reduce the noise of the profilometer measurement sufficiently so that it could be used as an input to a simulation of a high finesse cavity, the average of the two profiles was further smoothed by a Gaussian function with a smoothing radius of $5\,\mu\mathrm{m}$. This smoothing area was smaller than the structures imprinted by the dot milling process, as individual pulses had a waist of $60\,\mu\mathrm{m}$. In particular, this is a reasonable approach for PC fibers and MM fibers because they do not show small structures around the core as single-mode fibers do [115].

A significant difference with respect to the simulations in [115] was the value of the transmission $\mathcal{T}_{\mathrm{sim}}$ used for the OSCAR simulations. A $\mathcal{T}_{\mathrm{sim}}$ as high as possible was used such that the steady state was found faster. However, to reconstruct our higher finesse in the near-concentric regime with smaller waists compared to the simulations in [115], we needed to decrease $\mathcal{T}_{\mathrm{sim}}$ from 1% to $100\,\mathrm{ppm}$ per mirror. This corresponding high finesse in the simulations slowed down the simulation by a factor of about 1000 with respect to the simulations in [115]. As a result, the computation time was approximately days to weeks instead of hours on a desktop computer, as for the previous work [115]. A second change with respect to the simulations in [115] is in the process to find the correct TEM mode for the simulation. In [115], we used an input electric field which radius of curvature was adjusted to the expected cavity mode. Here, the TEM 00 was more likely found in the concentric regime when the input field was not adjusted that means the input field had an infinite curvature.

In comparison to the calculations based on Equation (3.13), the OSCAR simulated data now shows an additional agreement with the measured data for decreased finesses due to the mode crossings and in the confocal regime. Unfortunately, the high finesse values for short cavities could not be explained by this numerical simulation. Actually, the hypotheses discussed above were not taken into account by these simulations. Alternately, for both the model of Equation (3.13) and the OSCAR simulations, we could assume cavity scatter and absorption losses corresponding to the highest measured finesse, but then we would not be able to explain the drop in cavity finesse above $L = 100\,\mu\mathrm{m}$.

7.3 Expected cooperativity

To understand the expected cooperativity we expect to achieve when the cavity mode is coupled to a Ca^+ atom, we need to investigate the fiber cavity further. Along with the finesse, the waist of the cavity needs to be determined; see equation Equation (2.21). For an asymmetric cavity, the waist can be calculated from the g-parameters $g_i = 1 - L/R_i$ of each mirror $i \in \{1, 2\}$. The radii of curvature R_i of the mirrors were determined from the fits to the mirror surface profiles, and the finesse measurements confirm these values as the confocal regime with unstable modes was determined to be at $210 < L < 220\,\mu\mathrm{m}$. However, as our fiber mirrors are not exactly spherical, it is not clear if the effective radii of curvature are constant for different cavity lengths [200]. In fact, fits of the mirror profiles show that the radius depends on the size of the fitting area (see Figure 3.7), which could explain an increasing radius of curvature for an increasing spot size of the light field on the mirror. Therefore, we want to test whether the effective radius

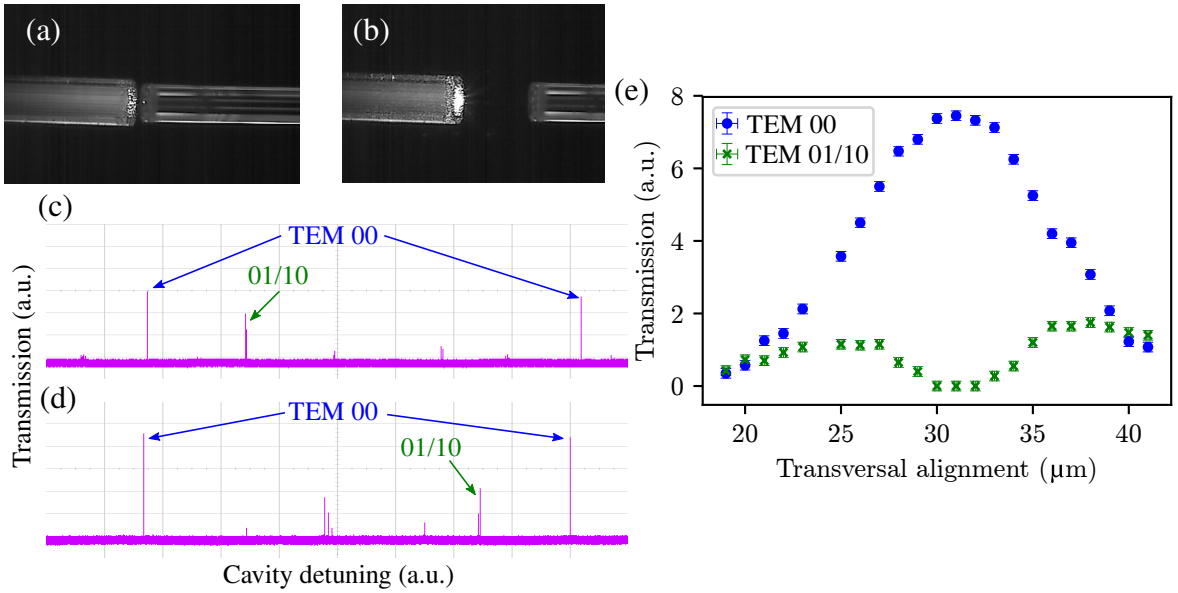

Figure 7.2: (a) Photo of the fiber cavity in the plane-parallel regime and (c) corresponding observed transmission spectra. (b) Photo of the fiber cavity in near-concentric regime and (d) corresponding observed transmission spectra. (e) Transmission of TEM 00 and 01 or 10 modes as a function of the transversal alignment of the MM fiber. As expected, the TEM 00 mode has only one maximum. In contrast, the TEM 01/10 mode has two maxima and vanishes at the maximum of the TEM 00. This behavior is used to distinguish between the TEM modes even in cases when the spectrum height does not allow the proper identification.

of curvature is indeed constant with the cavity length L by carrying out a further measurement of the frequency shift ν_{01} between the TEM 00 and 01 modes [119], which then allows us to check the dependence of the R_1 on L via the formula

$$R_1 = \frac{L}{1 - \cos\left(\frac{2\pi}{c} L \cdot \Delta\nu_{01}\right)}. \tag{7.1}$$

The second effective radius of curvature R_2 is similarly calculated from the frequency shift ν_{10} between TEM 00 and 10.

In most cases it is obvious to distinguish between the TEM modes by checking the height of the peaks in the transmission spectrum; see Figures 7.2 (c) and (d). With a rough knowledge about the regime of the fiber cavity (Figure 7.2 (a) for an example of plane-parallel geometry and (b) for an example of near-concentric geometry), the spectrum is clear to interpret. However, for the fiber cavity aligned in the concentric regime, the TEM 00 and 01/10 modes are almost equally excited because the light mode inside the PC fiber has a similar overlap with both cavity TEM modes. For such a cavity configuration, the modes can be further distinguished by moving one fiber transversally and monitoring the behavior of the transmission peaks. For example, Figure 7.2 (e), measured for a cavity in the plane-parallel regime, shows that for a well aligned TEM 00 mode, the 01 mode vanishes, as expected.

The frequency differences between the TEM 00 and 01/10 modes were measured analogously to the FSR measurement in Section 7.1. With Equation (7.1), we calculated the effective radius of curvature R_i for eleven cavity lengths over the full range of stable cavity modes (blue

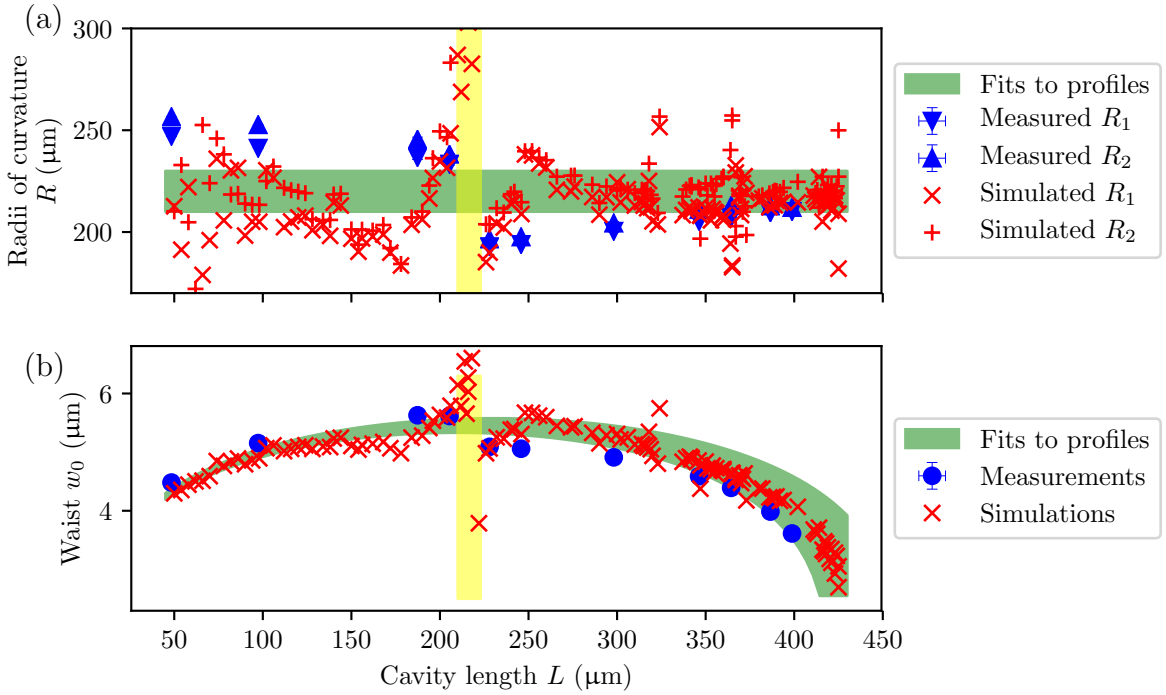

Figure 7.3: (a) Radii of curvature as a function of the cavity length. Values indicated by the green area were calculated with $R = 215(5)$ µm, which was extracted from fits to the two mirror profiles obtained after CO_2-laser ablation. The blue triangles are calculated from the measurements of mode splitting differences $\Delta\nu$ for various cavity lengths. By fitting the reconstructed light field of the optical FFT simulations, value of R for both mirrors can be extracted, shown as red crosses. The yellow area indicates the instability region of the cavity as marked in Figure 6.3. (b) Waist as a function of cavity length. With these values of R the cavity waists are calculated from Equation (3.3) for the measured, analytically calculated and simulated data, illustrated as in (a).

triangles in Figure 7.3 (a)). For cavity lengths shorter than the confocal regime, we measured radii of curvature R larger than the fits to the profiles would predict, but they are decreasing for longer cavities. However, beyond the confocal regime, the measured R are increasing slightly, but the values of R stay lower than the calculated radii of curvatures, which we attribute to the optimized mirror shape by the dot milling process [115]. In contrast to what is expected for Gaussian-shape mirrors [200], and to the fits of the profiles with varying size of the region of interest, the measured R do not increase significantly as a function of the cavity length.

An additional confirmation of the measured radius of curvature R is provided by a comparison with numerical simulations using OSCAR. The OSCAR code directly gives a fitted curvature of the reconstructed light field. Unfortunately, in our experience, these fits seem to fail quite often. Only the fitted spot sizes w_i on each mirror i seem to be trustworthy. Each g-parameter

$$g_i = \frac{1}{w_i^2}\sqrt{\frac{L^2\lambda^2}{\pi^2} - w_1^2 w_2^2} \tag{7.2}$$

can then be calculated from the fitted spot sizes w_i and the known parameters of the cavity

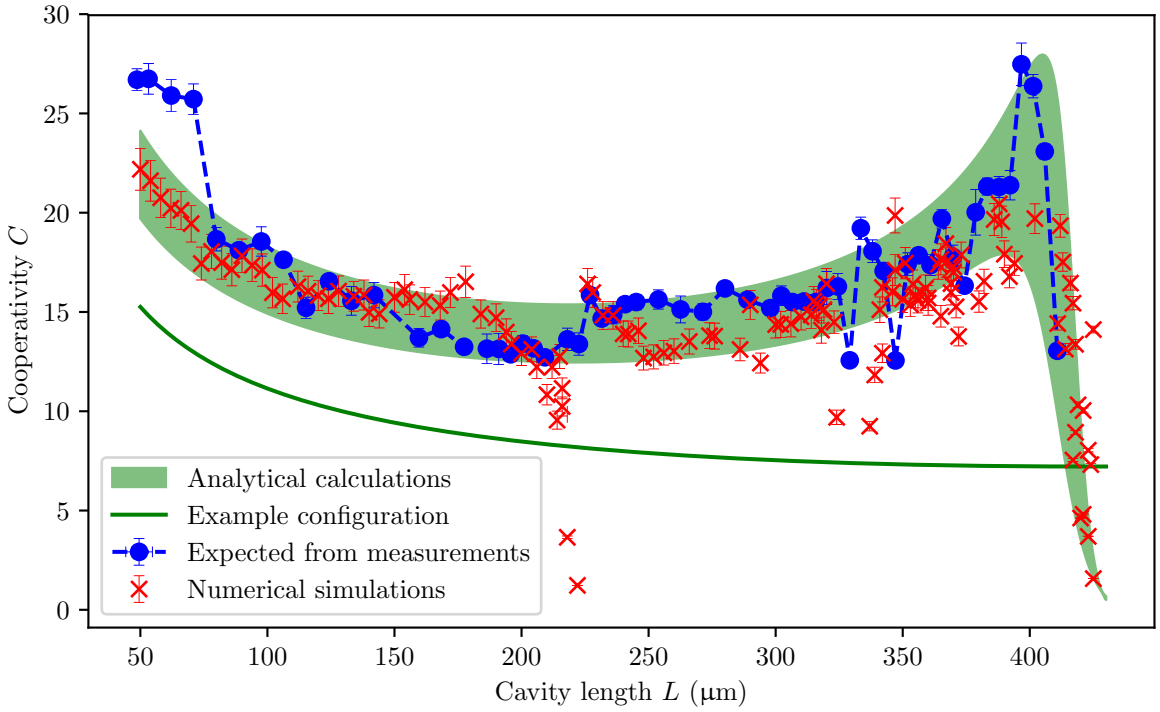

Figure 7.4: Expected cooperativity as a function of the cavity length. With the finesse shown in Figure 7.1 and waists shown in Figure 7.3 (b), we calculate the expected single-ion cooperativity for a calcium ion maximally coupled to the fiber cavity (Equation (2.19)), for the fitted data indicated as a green area, for the measured data plotted as blue points, and for the optical FFT simulation as red crosses. The green solid line shows the calculated cooperativity for a cavity configuration with $R = 420\,\mu\text{m}$ so that the confocal regime is at $L = 420\,\mu\text{m}$.

length L and the wavelength λ. These numerical simulations (red crosses in Figure 7.3 (a)) have a rather large spread up to $\pm 25\,\mu\text{m}$. In the confocal regime, they follow the measured value, as they are increased below the instability region, and decreased above. In the concentric regime, the simulations approach the measured value with a spread decreasing to $\pm 10\,\mu\text{m}$.

Using Equation (3.3), the waist as a function of the cavity length L is calculated from these fitted, measured and simulated radii of curvature R_i and plotted in Figure 7.3 (b). Overall, the expected waist is confirmed by the overlap between the fits to the profiles, the measured data, and the simulated cavity light fields.

Now we combine our detailed investigation of the finesse in Section 7.1 with this characterization of the cavity waist in order to calculate the expected single-ion cooperativity, using Equation (2.19). Once again, we find good agreement within the error bars between measurements, analytical calculations and numerical simulations, as seen in Figure 7.4. Additionally, the cooperativity of a cavity with radii of curvature $R = 420\ \mu\text{m}$ is plotted in Figure 7.4, which presents a confocal regime at a cavity length $L = 420\,\mu\text{m}$. We see that the cooperativity $C(L = 400\,\mu\text{m}) = 27$ corresponding to a concentric alignment, as measured here, improves upon the cooperativity $C'(L = 400\,\mu\text{m}) = 9$ corresponding to a confocal cavity configuration by a factor of about three.

7.4 Limitations in the concentric regime

We have seen that working in the concentric regime offers significant advantages to boost the cooperativities of trapped ion experiments. However, along with the decreasing finesse near the concentric stability boundary due to limited effective useful diameter D, we observed two further limitations in the concentric regime.

First, the transversal alignment is more sensitive for longer cavities. For short cavities, there is a range of tens of micrometers in which the cavity transmission is preserved as one of the mirrors is translated in a plane perpendicular to the cavity axis; see Figure 7.2 (e). However, for longer cavities, this stability range decreases. In the near-concentric regime, $L \approx 400\ \mu\mathrm{m}$, just touching the micrometer screws on the six-axis nanopositioning stage was enough to lose the cavity transmission. Therefore, we used the built-in piezos of the stage to perform a precise transversal alignment down to tens of nanometers. Such behavior is especially adverse when the cavity alignment needs to be fixed before being placed in ultra-high vacuum. Additional active stabilization in the transversal directions would be necessary [105], and glue would not be sufficient.

Second, we observed smaller transmission peaks for longer cavities, corresponding to a reduced probability that photons are able to leave the cavity through the PC fiber, although the PC fiber provides a broad range of high in-coupling [115]. As expected from calculations of the overlap between the fiber mode and the cavity mode, the transmission of the cavity is suppressed down to zero in the concentric regime; see Figure 3.3 (c). One solution would be to use fibers built from integrated mode-matching optics [201], with which this mode overlap could be theoretically increased to one even for near-concentric cavities.

Conclusion

In this section, we have shown that the cooperativity of our fiber cavity is expected to be enhanced by a factor up to three in the concentric regime compared to a confocal configuration. For that, we investigated both the finesse and the waist. Our measurements were confirmed by fits to surface profiles of our fiber mirrors and following analytically calculations. Further approval was shown by numerical simulations of the cavity light field based on mirror surfaces obtained by the fiber production. For our fiber mirrors, we need to choose between an enhanced cooperativity in the near-concentric regime and an optimized mode coupling efficiency for shorter cavities closer to the confocal configuration. With the translation stages in vacuum, the cavity configuration can be optimized for both cases in different experiments.

Chapter 8

Summary and outlook

Summary

This thesis reported on our studies to implement a fiber cavity perpendicular to a linear ion trap with the goal to reach a coupling strength between single trapped ions and single photons inside the cavity larger than the decay rates of both the ion and the cavity.

In Chapter 2, the theoretical description of a quantum interface based on ions coupled to a cavity was discussed. By means of a comparison between different cavity configurations, it was shown that fiber cavities promise to outperform conventional substrate cavities and to enter the strong-coupling regime, which enables highly efficient and high-fidelity quantum communication.

The technical realization was then described in the following two chapters. Whereas Chapter 3 focused on the technology of our self-made fiber mirrors, Chapter 4 focused on the integration of the fiber cavity into the ion trap. Theoretical calculations and simulations were carried out as well as measurements to confirm the expected characteristics. For the target cavity length, the finesse measured in vacuum yielded $\mathcal{F} \sim 40,000$, which was lower than the value of $\mathcal{F} \sim 50,000$ measured before vacuum assembly (Subsection 4.5.1). This drop of the measured finesse can be explained by an insufficiently tunable assembly without an angular adjustment that did not completely fulfill the angular alignment requirements of $\pm 1^\circ$ elicited in Subsection 3.3.3. Nevertheless, the expected coupling strength $g_0 = 2\pi \cdot 20$ MHz exceeds the dissipative decay rates $\kappa = 2\pi \cdot 4$ MHz and $\gamma = 2\pi \cdot 11.4$ MHz with the measured cavity configuration. Furthermore, simulations of the secular trap frequencies of the ion were confirmed by measurements, (Subsection 4.4.2). Here, our measurements agreed with simulations within error bars, but the axial confinement was found to be reduced from the target value of 1 MHz to $\omega_{\mathrm{ax}} \sim 200$ kHz caused by longer radial trap electrodes than we had intended, which was found to be necessary during the fabrication process.

The corresponding weak axial confinement intensified the anticipated challenge of charges on the fibers. However, my fellow graduate student Ben Ames developed a procedure, introduced in Section 4.6, to manipulate charges on dielectrics with an ion trap. With this procedure, we were able to reduce the charges on the fiber mirrors until a ion was trapped inside the fiber cavity. In Chapter 5, the coupling between an ion and the fiber cavity was investigated by repumping the ion with the light of the cavity. The cavity waist was measured and found to be consistent with expectations within the margins of error when the expected ion-cavity localiza-

tion is considered (Section 5.2. Unfortunately, the charges on the fibers were not stable enough for us to carry out such experiments reproducibly. In fact, after we measured the first ion-photon coupling and then lost the charge state of the fibers, we were never able to reduce the charges again to a level which would allow us to trap an ion in the cavity.

Therefore, a method was developed to determine the surface charge densities on dielectric fiber mirrors. The corresponding measurement and reconstruction are presented in Chapter 6. With the optimization of the reconstruction to the measured data, absolute values of surface charge densities of the fibers could be determined, ranging from -10 to $50\ e/\mu\mathrm{m}^2$.

From Chapter 7, we learned the lesson that a certain minimum cavity length is essential to trap ions in a linear trap close to a fiber cavity. Even alternate designs, allowing for better shielding of charges by electrodes are limited in the end by the electric field noise from these metal electrodes [112]. As introduced in Chapter 2, for a given cavity length, fiber cavities can be further improved by approaching the concentric regime with tailored radii of curvature $R \sim L/2$. Here, however, the known restriction of limited effective useful diameters needs to be considered. Taking this restriction into account, the maximal enhancement of operating a fiber cavity in the concentric regime was determined in Chapter 7. Not only could we verify that the finesse was maintained in the concentric regime, but also we determined the radii of curvature of the mirrors by a measurement of TEM mode splittings. Consequently, for near-concentric cavities, we predict an enhancement in the cooperativity up to a factor of three in comparison to a fiber cavity configured in the confocal regime, as in current state-of-the-art experiments.

Outlook

For future quantum communication to be highly efficient, the current experimental realization of ions in a linear trap coupled to a fiber cavity needs to be further improved. In this regard, both components, the ion trap and the fiber cavity, can be further developed.

Fiber cavity

The fiber cavity can be brought further into the concentric regime by improving the fiber mirror quality. Current measurements already show effective useful diameters up to $D > 100\ \mu\mathrm{m}$ [115]. It should be possible to optimize the mode coupling, which describes the efficiency with which a photon couples from the cavity mode into a single-mode fiber, close to unity by integrating mode-matching optics [201]. The second limitation in Section 7.4, the transversal alignment of near-concentric cavities can also be overcome by an active feedback to the alignment [105].

Furthermore, the effective useful diameter of the current fiber mirrors, $D \leq 80\ \mu\mathrm{m}$, is only a fraction of the fiber's cladding diameter (see Table 3.2). This means that a large dielectric area is facing to the ion without any purpose, but with the possibility to be charged. Electrodes could be designed to shield these areas [114], but to incorporate electrodes, the length of the cavity will need to be increased. If the electrode is just a thin layer of metal, this drawback may be negligible. However, optical access will still be reduced due to the electrode. The fiber mirror would be more beneficial if the entire fiber diameter could be used as a mirror. For the CO_2-laser ablation process, this large useless area at the fiber's edge is challenging to avoid unless additional techniques are applied like removing the cladding by polishing. Maybe in the future,

other fabrication procedures like FIBS (Section 3.2) will outperform the CO_2-laser ablation, as they will enable a spherical mirror to be fabricated up to the edge of the fiber.

Another approach is to avoid the use of dielectrics close to the ions entirely. Substrate-transferred crystalline coatings could be used instead of the ion-beam-sputtered coatings. Such crystalline coatings based on gallium arsenide recently showed low scatter and absorption losses down to 3 ppm at a wavelength of $1064\,\mathrm{nm}$ [202]. As these coatings consist of semiconductors, the mirrors could directly act as electrodes. Currently, these conductive highly reflective mirrors are not compatible for our wavelength of $\sim 850\,\mathrm{nm}$. However, research is underway at the company[1] behind this technology to develop suitable coatings for our wavelength. Another option would be use an ion species with a transition frequency compatible with semiconductor mirrors.

Wheel trap – the next-generation ion trap

Charges on dielectrics close to ion traps can now be better taken into account by simulating them as surface charge densities, as presented in Chapter 6. As discussed in Subsection 6.6.3, this method could help in various ion-trap experiments to estimate the surface charge densities of dielectrics. Furthermore, the absolute surface-charge densities determined in our experiment are of special interest for simulations to design new CQED experiments with dielectrics close to trapped ions.

As a next step, we put our acquired experience into practice. In our measurements, we observed mostly positively charged fibers, which were acting like endcaps as the fibers split our axial potential into a double well. This behavior and the radial symmetry of the fibers suggest the idea that the fiber cavity's optical axis should be parallel to the ion-trap axis. However, the maximal cavity length $L < 1\,\mathrm{mm}$, restricted by our target coupling strength, would be too short for a linear "Innsbruck-style" ion trap, because non-negligible micromotion would be present along the trap axis. I recognized that by adopting the design of the Al-clock experiment at NIST[2], called "wheel trap," a fiber cavity could be integrated in a linear ion trap along the trap axis [203]. In this trap design, a diamond gold-plated chip provides a precise radial alignment of the blades. With a chip thickness of just $330\,\mu\mathrm{m}$, the wheel trap is a really short linear ion trap, so that it is possible for the fiber-cavity mirror surrounded by metal tubes to be implemented as endcaps. To avoid micromotion along the trap axis, a +/- RF drive (Subsection 2.1.1) is applied to each pair of opposing blades. Simulations that we have carried out have shown that axial micromotion is expected to be negligible and that charges densities similar in magnitude to those presented in this thesis can be compensated for. Furthermore, my successor Markus Teller has shown by means of simulations that a fiber cavity can be aligned with respect to a trapped ion by simply moving the fibers with their metal tubes, avoiding the correlation of the RF field with the fiber alignment that was observed in [185]. In conclusion, the new design of a linear ion trap based on the successful wheel trap [204] should allow the coupling of an ion to an integrated fiber cavity without the need for non-reproducible charge manipulation. The design, assemble, and testing of such a trap will be the focus of the next generation of fiber-cavity research in Innsbruck.

[1] Crystalline Mirror Solutions GmbH

[2] National Institute of Standards and Technology, U.S. Department of Commerce

Appendix A

Experimental configurations

A.1 Annealing oven

We built a special annealing oven, inspired by our collaborators in Paris, as described in Subsection 3.2.3, to be able to heat only the fiber tip. A photograph of the experimental setup is shown in Figure A.1 (a). This self-made oven consisted of a cut up glass pipette, a heating wire[1], and a temperature-sensitive resistor[2]. The heating wire was wound around the straitened tip of the pipette. The larger end of the pipette was put over the wound heating wire as heat isolation; see Figure A.1 (b) for a zoomed view. This construction was mounted on MACOR ceramics to decouple the heat of the oven from the mount. The temperature-sensitive resistor was placed close to the outer glass pipette to monitor the temperature of the setup, see Figure A.1. As explained in Subsection 3.2.3, the absolute temperature was calibrated by a dummy annealing process with a calibrated K-type negative temperature coefficient resistor connected to a multimeter.

The electronics to operate the oven were divided into two parts which were both connected to a microcontroller board[3]. In Figure A.1 (c), the used circuit diagram is sketched. The first part sets the power of the heater. A pulse-width modulated (PWM) signal from an digital output of the microcontroller was applied via a resistor onto the *gate* of a transistor[4]. The *source* of the transistor was grounded. At the *Drain*, the heat wire was connected to a power supply with $V_H = 11\,\mathrm{V}$. Usually, the desired temperature of $350\ ^\circ\mathrm{C}$ was achieved at $1.4\ \mathrm{A}$.

The second part of the electronics was used to measure the temperature-sensitive resistor so that the temperature could be continuously monitored during the annealing process. With a measurement bridge supplied by a stable voltage reference[5], the resistance of the temperature sensor was converted to a voltage difference. With the aid of an instrumentation-amplifier[6], the voltage difference was transferred into a voltage with variable amplification. The amplified voltage was then digitized via an analog input of the microcontroller.

Both the digital pulse-width modulated output and the analog input were then controlled

[1] ISACHROM 60 - resistor wire with 5.65 Ω/m
[2] Linear Silicon PTC Thermistors Temperature Sensors AM-LPTC600
[3] Arduino UNO
[4] IRFP240
[5] Analog Device REF-01
[6] Texas Instruments INA114AP

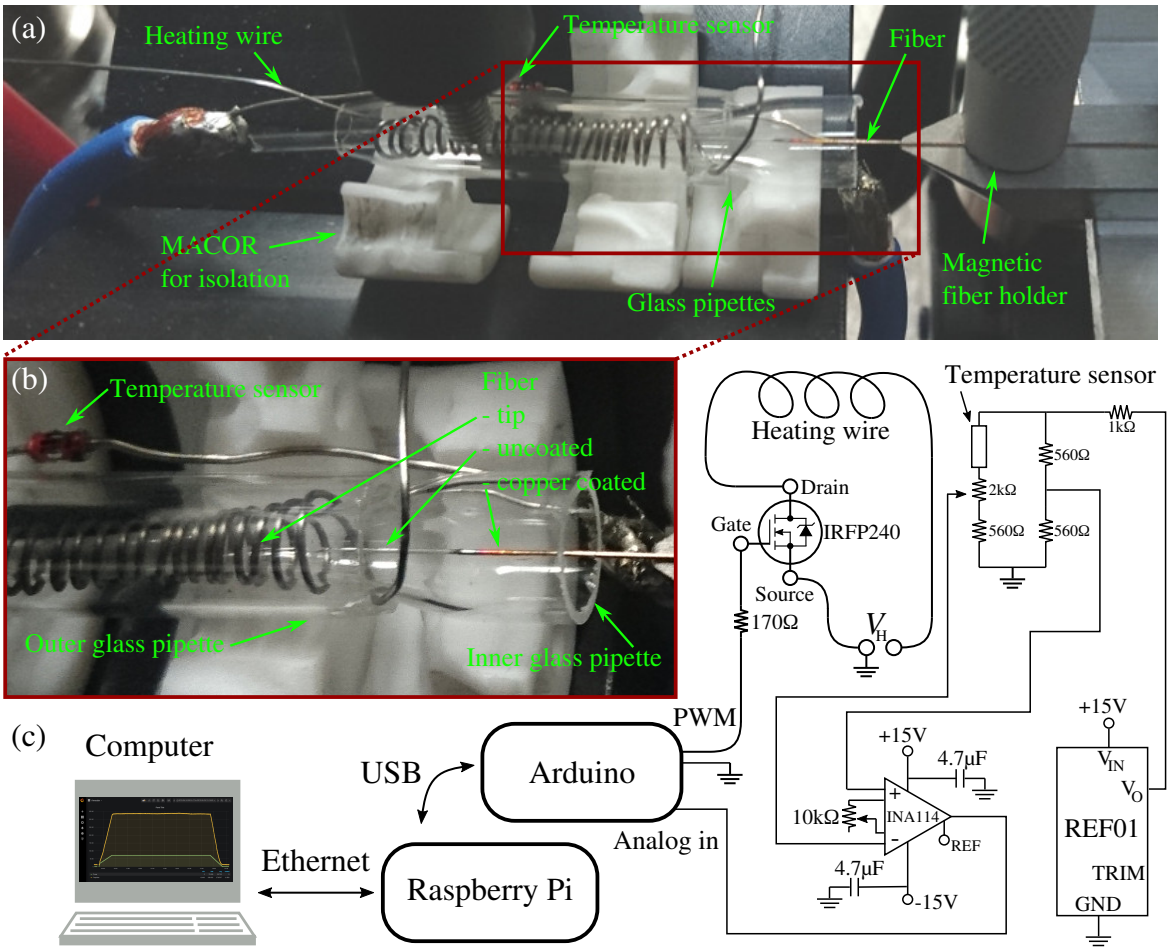

Figure A.1: (a) Photograph of the annealing setup. (b) Zoomed view of the heater around the fiber tip. (c) Schematics of the electronics to control the heater and to monitor the oven via a temperature sensor.

and read by a single-board computer[7] via a universal serial connection (USB). A python script ran on the single-board computer. With a configuration file, the starting time, the length, and final duty cycle of the PWM signal of multiple steps were set, and could be adapted while the program was running. Both the value of the digital output and the value of the analog input were saved on an open-source time series database[8]. Via an open-source analytics and monitoring solution[9], the values of the pulse-width modulated signal and the digitized voltage were monitor in real time.

[7]Raspberry Pi
[8]InfluxDB
[9]Grafana

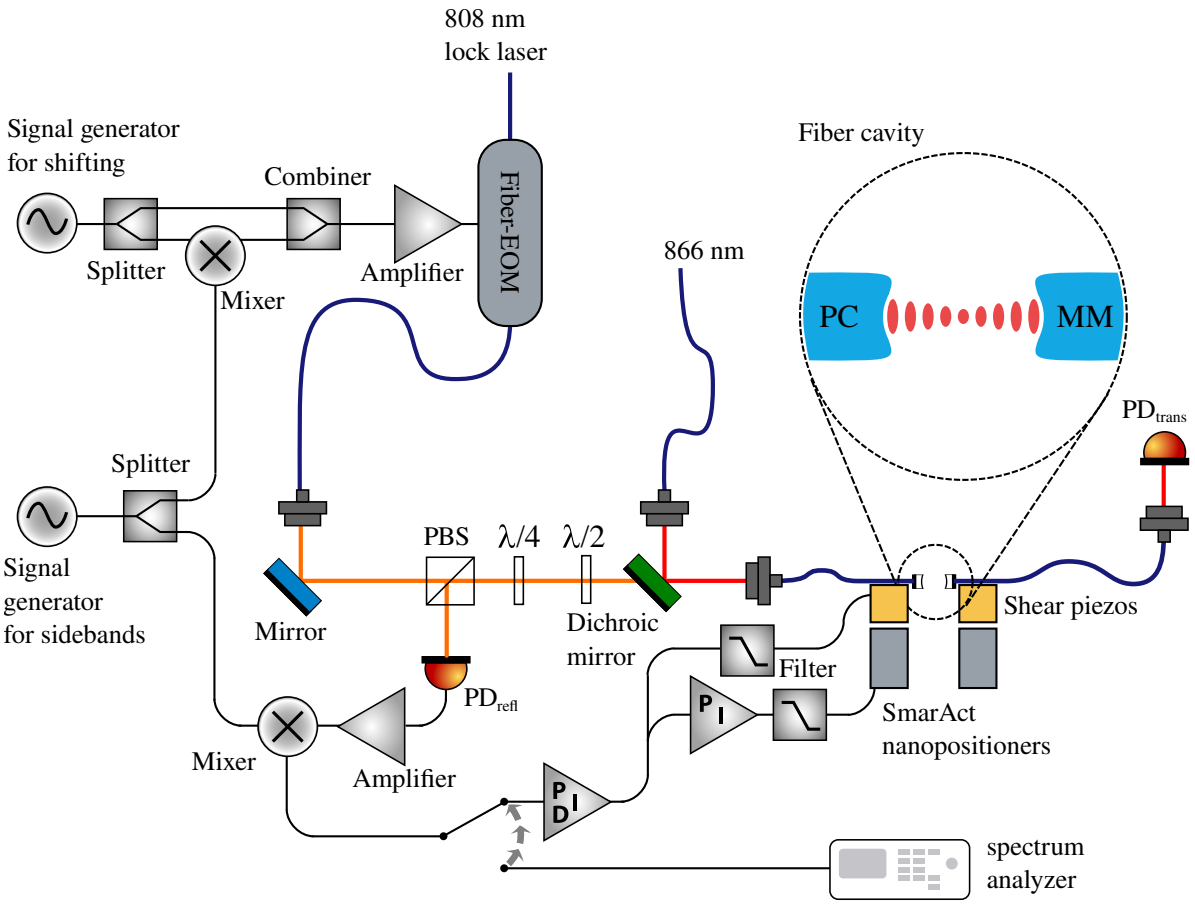

Figure A.2: Optical and electric setup of transfer lock.

A.2 Cavity lock feedback

The experimental setup of the fiber cavity was built in such a way that it could be used to analyze vibrations of the fiber cavity or stabilize the length of the fiber cavity. The setup (sketched in Figure A.2) is divided into two parts: optics and electronics.

In the optical setup, two laser beams were coupled into the fiber cavity. A 866 nm laser was used to drive the ion inside the cavity, as described in Chapter 5. At the same time, a 808 nm laser was resonant with the cavity and it was used as a precise meter to lock the length of the fiber cavity. For a Pound-Drever-Hall (PDH) locking scheme [175, 176], the 808 nm light was modulated by a fiber-based electro-optic modulator (fiber-EOM)[10] with a bandwidth of 10 GHz. Both laser beams were overlapped by a dichroic mirror and coupled into the fiber cavity. With a polarizing beam splitter (PBS), a $\lambda/2$-waveplate, and a $\lambda/4$-waveplate, the reflected light of the cavity was adjusted onto a photodiode $\mathrm{PD}_{\mathrm{refl}}$ to detect the reflection of the fiber cavity. Another photodiode $\mathrm{PD}_{\mathrm{trans}}$ was set up after the fiber cavity to monitor the transmission.

The electrical setup consisted of two parts. In the first part, a first signal generator created a RF drive to shift the laser up to 10 GHz. Its signal was divided by a RF-splitter. One output was

[10] iXblue Photonics NIR-MPX800-LN-10

mixed with a $5\ \mathrm{MHz}$ RF-signal from a second function generator to generate sidebands for the PDH lock. Next, both paths were combined again and applied to the fiber EOM, see Figure A.2. Summarizing, sidebands of sidebands were created with this first part of the electrical setup.

In the second part, the error signal for the PDH lock was generated by mixing the RF signal of the second signal generator as local oscillator with the signal of $\mathrm{PD}_{\mathrm{refl}}$. The error signal could be used to lock the length of fiber cavity onto the stable $808\ \mathrm{nm}$ laser by applying a feedback on the piezos of the fiber cavity. A first proportional-integral-derivative (PID) controller generated a fast feedback onto the shear piezos. A second proportional-integral (PI) controller kept the offset of the first PID controller low by a slow feedback onto the piezo of the Smaract nanopositioner such that slow drifts were compensated up to few micrometers as the voltage applied to the shear piezo was limited to a range corresponding to a few nanometers.

Furthermore, the described setup was used to analyze the cavity vibrations. Therefore, the error signal was recorded by a spectrum analyzer instead of applying a feedback with the PID controllers (switch at lower position in Figure A.2). By changing the wavelength of the laser, the precision and the maximal amplitude of the error signal could be adjusted. The longer the wavelength, the lower was the transmission of the fiber mirrors, see Figure 3.8 for wavelengths from $770\ \mathrm{nm}$ to $850\ \mathrm{nm}$. With a lower transmission, the linewidth was narrower. Note that the frequency of the sidebands for the error signal needed be adjusted to the new linewidth, too. A narrow linewidth results in a sensitive error signal with a high precision. At the same time, the linear range of the error signal is decreased so that only smaller amplitudes of the noise can be analyzed. Using a noise spectrum with an optimized precision, the vibrations of our system were discussed in Section 4.5.2.

For an analysis of the piezos, an active scheme of the analysis was carried out. A network analyzer excited one piezo, and recorded the transfer function by measuring the response of the locking system via the error signal. With the transfer function taken by the network analyzer, the eigen resonances of the system were further characterized, and a filter could be tailored specifically to the resonance characteristics of the locking system [128]. In particular, a feedback to both fibers with individual filters of each stage could open the possibility to compensate the resonance of one nanopositioner with the other one and vice versa if the resonance frequencies of the nanopositioners differ sufficiently.

Appendix B

Publications

This appendix contains a list of papers published during the course of my thesis. My first contribution to a publication [124] was during my Master's thesis as I measured the birefringences of our fiber cavities. In the beginning of my PhD work, I continued to help my predecessor Birgit Brandstätter with the data analysis of the birefringence and corrections of the publication. Besides the work on the fiber cavity experiment, I contributed to the two-ion Cavity-QED experiments [48, 49] of Bernardo Casabone and Konstantin Friebe by discussing their measurements, as well as creating figures and graphics. During the collaboration with Prof. Jakob Reichel (Chapter 3), we, Konstantin Ott, Sebastién Garcia, and I, built a revised version of their CO_2-laser ablation setup so that Konstantin Ott was able to fabricate fiber mirrors for $1\,\mathrm{mm}$-and-longer cavities [115]. Back in Innsbruck, I helped Moonjoo Lee and Konstantin Friebe to measure photon numbers in our substrate cavity setup by installing measurement devices, discussing measurements and results, designing graphics and creating figures [55]. In the scope of a collaboration with Prof. Dong-Il "Dan" Cho, we wrote an article [5] about the design of a microelectromechanical-based system in which a fiber-cavity is integrated into an ion-trap. I contributed with my experiences in fiber cavities, and I did calculations of the expected Cavity-QED parameters. Concerning my own project, the fiber-cavity experiment, our postdoc Florian Ong measured the ion's characteristics in the vicinity of our optical fibers (Chapter 6) with the help of Pierre Jobez and me. Florian Ong started with the analysis of these measurements, which I finalized after he left our research group. We, Tracy Northup, Florian Ong, Markus Teller, and I, completed then the publication [188]. Furthermore, I measured our fiber cavities in the concentric regime (Chapter 7) and prepared an article for publication [198].

My publications

[124] Brandstätter, B., McClung, A., Schüppert, K., Casabone, B., Friebe, K., Stute, A., Schmidt, P. O., Deutsch, C., Reichel, J., Blatt, R., and Northup, T. E. (2013). Integrated fiber-mirror ion trap for strong ion-cavity coupling. *Rev. Sci. Instrum.*, 84(12):123104.

[49] Casabone, B., Friebe, K., Brandstätter, B., Schüppert, K., Blatt, R., and Northup, T. E. (2015). Enhanced quantum interface with collective ion-cavity coupling. *Phys. Rev. Lett.*, 114(2):023602.

[48] Casabone, B., Stute, A., Friebe, K., Brandstätter, B., Schüppert, K., Blatt, R., and Northup, T. E. (2013). Heralded entanglement of two ions in an optical cavity. *Phys. Rev. Lett.*, 111(10):100505.

[55] Lee, M., Friebe, K., Fioretto, D. A., Schüppert, K., Ong, F. R., Plankensteiner, D., Torggler, V., Ritsch, H., Blatt, R., and Northup, T. E. (2019a). Ion-based quantum sensor for optical cavity photon numbers. *Phys. Rev. Lett.*, 122(15):153603.

[5] Lee, M., Lee, M., Hong, S., Schüppert, K., Kwon, Y.-D., Kim, T., Colombe, Y., Northup, T. E., Cho, D.-I. D., and Blatt, R. (2019b). Microelectromechanical-system-based design of a high-finesse fiber cavity integrated with an ion trap. *Phys. Rev. Applied*, 12(4):044052.

[188] Ong, F. R., Schüppert, K., Jobez, P., Teller, M., Ames, B., Fioretto, D. A., Friebe, K., Lee, M., Colombe, Y., Blatt, R., and Northup, T. E. (2020). Probing surface charge densities on optical fibers with a trapped ion. *New J. Phys. in press*.

[115] Ott, K., Garcia, S., Kohlhaas, R., Schüppert, K., Rosenbusch, P., Long, R., and Reichel, J. (2016). Millimeter-long Fabry-Pérot cavities. *Opt. Express*, 24:9839–9853.

[198] Schüppert, K., Blatt, R., and Northup, T. E. (2020). High-finesse fiber-based optical resonators in the concentric regime. *in preparation*.

List of abbreviations

2D:	two-dimensional
AC:	alternating current, time-varying
Ca:	calcium
CCD:	charge-coupled device
CO_2:	carbon dioxide
CQED:	cavity quantum electrodynamics
DC:	direct current
EOM:	electro-optic modulator
FFT:	fast Fourier transform
FIBS:	focused-ion-beam sputtering
FPGA:	field-programmable gate array
FSR:	free spectral range
GND:	ground
GPS:	Global Positioning System
LMA:	large mode area
MM fiber:	multi mode fiber
PBS:	polarizing beam splitter
PC fiber:	photonic-crystal fiber
PD:	photodiode
PDH:	Pound-Drever-Hall
PhD:	Doctor of Philosophy
PI(D):	proportional-integral(-derivative)
PMT:	photomultiplier tube
ppm:	parts per million
RF:	radio frequency
SEE:	secondary electron emission
SM fiber:	single-mode fiber
SPCM:	single-photon counting module
TEM:	transverse electromagnetic
Ti:sapph:	titanium-sapphire laser
UHV:	ultra-high vacuum
UV:	ultraviolet

List of Figures

List of Tables

Bibliography

[1] E. J. Lilienfeld, "Method and apparatus for controlling electric currents," (1926).

[2] G. E. Moore, IEEE Solid-State Circuits Society Newsletter **11**, 33 (2006).

[3] M. Dubash, Techworld from IDG (2010).

[4] L. Su, "Delivering the future of high-performance computing with system, software and silicon co-optimization," (2019) 2019.

[5] E. Schrödinger, Naturwissenschaften **23**, 807 (1935).

[6] M. A. Nielsen and I. L. Chuang, *Quantum Computation and Quantum Information* (Cambridge University Press, Cambridge, 2010).

[7] A. Einstein, B. Podolsky, and N. Rosen, Phys. Rev. **47**, 777 (1935).

[8] J. P. Dowling and G. J. Milburn, Philosophical Transactions of the Royal Society of London. Series A: Mathematical, Physical and Engineering Sciences **361**, 1655 (2003).

[9] European-Commission, European Cloud Initiative - Building a competitive data and knowledge economy in Europe (2016).

[10] C. L. Degen, F. Reinhard, and P. Cappellaro, Rev. Mod. Phys. **89**, 035002 (2017).

[11] BIPM, "Resolution 1 of the 13th CGPM," (1967).

[12] H. J. Mamin, M. Kim, M. H. Sherwood, C. T. Rettner, K. Ohno, D. D. Awschalom, and D. Rugar, Science **339**, 557 (2013).

[13] C. Bennett and G. Brassard, in *Proceedings of IEEE International Conference on Computers, Systems and Signal Processing*, Vol. 175 (Bangalore, India, New York, 1984) p. 8.

[14] M. Krenn, M. Malik, T. Scheidl, R. Ursin, and A. Zeilinger, "Quantum communication with photons," in *Optics in Our Time*, edited by M. D. Al-Amri, M. El-Gomati, and M. S. Zubairy (Springer International Publishing, Cham, 2016) pp. 455–482.

[15] J. Yin, Y. Cao, Y.-H. Li, S.-K. Liao, L. Zhang, J.-G. Ren, W.-Q. Cai, W.-Y. Liu, B. Li, H. Dai, G.-B. Li, Q.-M. Lu, Y.-H. Gong, Y. Xu, S.-L. Li, F.-Z. Li, Y.-Y. Yin, Z.-Q. Jiang, M. Li, J.-J. Jia, G. Ren, D. He, Y.-L. Zhou, X.-X. Zhang, N. Wang, X. Chang, Z.-C. Zhu, N.-L. Liu, Y.-A. Chen, C.-Y. Lu, R. Shu, C.-Z. Peng, J.-Y. Wang, and J.-W. Pan, Science **356**, 1140 (2017).

[16] H.-L. Yin, T.-Y. Chen, Z.-W. Yu, H. Liu, L.-X. You, Y.-H. Zhou, S.-J. Chen, Y. Mao, M.-Q. Huang, W.-J. Zhang, H. Chen, M. J. Li, D. Nolan, F. Zhou, X. Jiang, Z. Wang, Q. Zhang, X.-B. Wang, and J.-W. Pan, Phys. Rev. Lett. **117**, 190501 (2016).

[17] H.-J. Briegel, W. Dür, J. I. Cirac, and P. Zoller, Phys. Rev. Lett. **81**, 5932 (1998).

[18] H. J. Kimble, Nature **453**, 1023 (2008).

[19] S. Wehner, D. Elkouss, and R. Hanson, Science **362** (2018).

[20] J. A. Vaccaro, J. Spring, and A. Chefles, Phys. Rev. A **75**, 012333 (2007).

[21] P. Benioff, Journal of Statistical Physics **22**, 563 (1980).

[22] R. P. Feynman, Int. J. Theor. Phys. **21**, 467 (1982).

[23] C. Kokail, C. Maier, R. van Bijnen, T. Brydges, M. K. Joshi, P. Jurcevic, C. A. Muschik, P. Silvi, R. Blatt, C. F. Roos, and P. Zoller, Nature **569**, 355 (2019).

[24] L. Grover, in *Proceedings of the twenty-eighth annual ACM symposium on Theory of computing* (ACM, 1996) pp. 212–219.

[25] P. W. Shor, in *Proc. Annu. Symp. Found. Comput. Sci.* (1994) pp. 124–134.

[26] J. I. Cirac and P. Zoller, Phys. Rev. Lett. **74**, 4091 (1995).

[27] H. Häffner, C. F. Roos, and R. Blatt, Phys. Rep. **469**, 155 (2008).

[28] M. D. Barrett, J. Chiaverini, T. Schaetz, J. Britton, W. M. Itano, J. D. Jost, E. Knill, C. Langer, D. Leibfried, R. Ozeri, and D. J. Wineland, Nature **429**, 737 (2004).

[29] M. Riebe, H. Häffner, C. F. Roos, W. Hansel, J. Benhelm, G. P. T. Lancaster, T. W. Korber, C. Becher, F. Schmidt-Kaler, D. F. V. James, and R. Blatt, Nature **429**, 734 (2004).

[30] Y. Wang, M. Um, J. Zhang, S. An, M. Lyu, J.-N. Zhang, L.-M. Duan, D. Yum, and K. Kim, Nat. Photonics **11**, 646 (2017).

[31] P. Schindler, J. T. Barreiro, T. Monz, V. Nebendahl, D. Nigg, M. Chwalla, M. Hennrich, and R. Blatt, Science **332**, 1059 (2011).

[32] C. Monroe and J. Kim, Science **339**, 1164 (2013).

[33] D. Kielpinski, C. Monroe, and D. J. Wineland, Nature **417**, 709 (2002).

[34] M. D. Hughes, B. Lekitsch, J. A. Broersma, and W. K. Hensinger, Contemp. Phys. **52**, 505 (2011).

[35] C. D. Bruzewicz, J. Chiaverini, R. McConnell, and J. M. Sage, Appl. Phys. Rev. **6**, 021314 (2019).

[36] C. Monroe, Nature **416**, 238 (2002).

[37] L.-M. Duan and C. Monroe, Rev. Mod. Phys. **82**, 1209 (2010).

[38] C. Monroe, R. Raussendorf, A. Ruthven, K. R. Brown, P. Maunz, L.-M. Duan, and J. Kim, Phys. Rev. A **89**, 022317 (2014).

[39] T. E. Northup and R. Blatt, Nat. Photonics **8**, 356 (2014).

[40] B. B. Blinov, D. L. Moehring, L.-M. Duan, and C. Monroe, Nature **428**, 153 (2004).

[41] J. McKeever, A. Boca, A. D. Boozer, R. Miller, J. R. Buck, A. Kuzmich, and H. J. Kimble, Science **303**, 1992 (2004).

[42] M. Keller, B. Lange, K. Hayasaka, W. Lange, and H. Walther, Appl. Phys. B **76**, 125 (2003).

[43] H. G. Barros, A. Stute, T. E. Northup, C. Russo, P. O. Schmidt, and R. Blatt, New J. Phys. **11**, 103004 (2009).

[44] A. Steane and D. Lucas, Fortschr. Phys. **48**, 839 (2000).

[45] C. Russo, H. G. Barros, A. Stute, F. Dubin, E. S. Phillips, T. Monz, T. E. Northup, C. Becher, T. Salzburger, H. Ritsch, P. O. Schmidt, and R. Blatt, Appl. Phys. B **95**, 205 (2009).

[46] A. Stute, B. Casabone, P. Schindler, T. Monz, P. O. Schmidt, B. Brandstätter, T. E. Northup, and R. Blatt, Nature **485**, 482 (2012).

[47] A. Stute, B. Casabone, B. Brandstätter, K. Friebe, T. E. Northup, and R. Blatt, Nat. Photonics **7**, 219 (2013).

[48] B. Casabone, A. Stute, K. Friebe, B. Brandstätter, K. Schüppert, R. Blatt, and T. E. Northup, Phys. Rev. Lett. **111**, 100505 (2013).

[49] B. Casabone, K. Friebe, B. Brandstätter, K. Schüppert, R. Blatt, and T. E. Northup, Phys. Rev. Lett. **114**, 023602 (2015).

[50] P. Kómár, E. M. Kessler, M. Bishof, L. Jiang, A. S. Sørensen, J. Ye, and M. D. Lukin, Nature Physics **10**, 582 (2014).

[51] Z. Eldredge, M. Foss-Feig, J. A. Gross, S. L. Rolston, and A. V. Gorshkov, Phys. Rev. A **97**, 042337 (2018).

[52] T. J. Proctor, P. A. Knott, and J. A. Dunningham, Phys. Rev. Lett. **120**, 080501 (2018).

[53] F. Yoshihara, T. Fuse, S. Ashhab, K. Kakuyanagi, S. Saito, and K. Semba, Nature Physics **13**, 44 (2016).

[54] P. Forn-Díaz, J. García-Ripoll, B. Peropadre, J.-L. Orgiazzi, M. Yurtalan, R. Belyansky, C. Wilson, and A. Lupascu, Nat. Phys. **13**, 39 (2016).

[55] M. Lee, K. Friebe, D. A. Fioretto, K. Schüppert, F. R. Ong, D. Plankensteiner, V. Torggler, H. Ritsch, R. Blatt, and T. E. Northup, Phys. Rev. Lett. **122**, 153603 (2019).

[56] M. G. Raizen, J. M. Gilligan, J. C. Bergquist, W. M. Itano, and D. J. Wineland, Phys. Rev. A **45**, 6493 (1992).

[57] W. Paul, O. Osberghaus, and E. Fischer, *Ein Ionenkäfig*, Tech. Rep. 415 (1958).

[58] F. M. Penning, Physica **3**, 873 (1936).

[59] P. K. Ghosh, *Ion traps* (Clarendon Press, Oxford, 1996).

[60] D. Leibfried, R. Blatt, C. Monroe, and D. Wineland, Rev. Mod. Phys. **75**, 281 (2003).

[61] L.-M. Duan, M. D. Lukin, J. I. Cirac, and P. Zoller, Nature **414**, 413 (2001).

[62] D. James, Appl. Phys. B **66**, 181 (1998).

[63] P. A. Barton, C. J. S. Donald, D. M. Lucas, D. A. Stevens, A. M. Steane, and D. N. Stacey, Phys. Rev. A **62**, 032503 (2000).

[64] A. Kreuter, C. Becher, G. P. T. Lancaster, A. B. Mundt, C. Russo, H. Häffner, C. Roos, W. Hänsel, F. Schmidt-Kaler, R. Blatt, and M. S. Safronova, Phys. Rev. A **71**, 032504 (2005).

[65] R. Gerritsma, G. Kirchmair, F. Zähringer, J. Benhelm, R. Blatt, and C. Roos, The European Physical Journal D **50**, 13 (2008).

[66] M. Hettrich, T. Ruster, H. Kaufmann, C. F. Roos, C. T. Schmiegelow, F. Schmidt-Kaler, and U. G. Poschinger, Phys. Rev. Lett. **115**, 143003 (2015).

[67] A. H. Myerson, D. J. Szwer, S. C. Webster, D. T. C. Allcock, M. J. Curtis, G. Imreh, J. A. Sherman, D. N. Stacey, A. M. Steane, and D. M. Lucas, Phys. Rev. Lett. **100**, 200502 (2008).

[68] M. O. Scully and M. S. Zubairy, *Quantum Optics* (Cambridge University Press, Cambridge, 1997).

[69] A. Sørensen and K. Mølmer, Phys. Rev. Lett. **82**, 1971 (1999).

[70] P. Schindler, D. Nigg, T. Monz, J. T. Barreiro, E. Martinez, S. X. Wang, S. Quint, M. F. Brandl, V. Nebendahl, and C. F. Roos, New J. Phys. **15**, 123012 (2013).

[71] T. Monz, K. Kim, A. S. Villar, P. Schindler, M. Chwalla, M. Riebe, C. F. Roos, H. Häffner, W. Hänsel, M. Hennrich, and R. Blatt, Phys. Rev. Lett. **103**, 200503 (2009).

[72] M. Zwerger, B. P. Lanyon, T. E. Northup, C. A. Muschik, W. Dür, and N. Sangouard, Quantum Science and Technology **2**, 044001 (2017).

[73] C. F. Roos, M. Riebe, H. Häffner, W. Hänsel, J. Benhelm, G. P. T. Lancaster, C. Becher, F. Schmidt-Kaler, and R. Blatt, Science **304**, 1478 (2004).

[74] T. Ruster, C. T. Schmiegelow, H. Kaufmann, C. Warschburger, F. Schmidt-Kaler, and U. G. Poschinger, Appl. Phys. B **122**, 254 (2016).

[75] C. Flühmann, T. L. Nguyen, M. Marinelli, V. Negnevitsky, K. Mehta, and J. P. Home, Nature **566**, 513 (2019).

[76] U. L. Andersen, J. S. Neergaard-Nielsen, P. van Loock, and A. Furusawa, Nature Physics **11**, 713 (2015).

[77] D. Wineland and W. Itano, Phys. Rev. A **20**, 1521 (1979).

[78] H. J. Metcalf and P. van der Straten, *Laser Cooling and Trapping*, 2nd ed. (Springer, 2001).

[79] F. Diedrich, J. C. Bergquist, W. M. Itano, and D. J. Wineland, Phys. Rev. Lett. **62**, 403 (1989).

[80] C. Roos, T. Zeiger, H. Rohde, H. C. Nägerl, J. Eschner, D. Leibfried, F. Schmidt-Kaler, and R. Blatt, Phys. Rev. Lett. **83**, 4713 (1999).

[81] C. M. Russo, *Photon Statistics of a Single Ion Coupled to a High-Finesse Cavity*, Ph.D. thesis, Leopold-Franzens-Universität Innsbruck (2008).

[82] A. Stute, *A Light-Matter Quantum Interface: Ion-Photon Entanglement and State Mapping*, Ph.D. thesis, Leopold-Franzens-Universität Innsbruck (2012).

[83] B. Brandstätter, *Integration of Fiber Mirrors and Ion Traps for a High-Fidelity Quantum Interface*, Ph.D. thesis, Leopold-Franzens-Universität Innsbruck (2013).

[84] K. Friebe, *On dispersive interactions between a trapped ion and a cavity field*, Ph.D. thesis, Leopold-Franzens-Universität Innsbruck (2019).

[85] E. T. Jaynes and F. W. Cummings, Proc. IEEE **51**, 89 (1963).

[86] C. Cohen-Tannoudji, J. Dupont-Roc, and G. Grynberg, *Atom-Photon Interactions* (John Wiley & Sons, Inc., 1998).

[87] H. Carmichael, *An Open Systems Approach to Quantum Optics* (Springer-Verlag, Berlin, 1993).

[88] J. I. Cirac, P. Zoller, H. J. Kimble, and H. Mabuchi, Phys. Rev. Lett. **78**, 3221 (1997).

[89] C. J. Foot, *Atomic Physics* (Oxford University Press, 2005).

[90] C. C. Gerry and J. H. Eberly, Phys. Rev. A **42**, 6805 (1990).

[91] A. Stute, B. Casabone, B. Brandstätter, D. Habicher, P. O. Schmidt, T. E. Northup, and R. Blatt, Appl. Phys. B **107**, 1145 (2012).

[92] H. Goto, S. Mizukami, Y. Tokunaga, and T. Aoki, Phys. Rev. A **99**, 053843 (2019).

[93] A. V. Gorshkov, A. André, M. D. Lukin, and A. S. Sørensen, Phys. Rev. A **76**, 033804 (2007).

[94] C. Law and H. Kimble, J. Mod. Opt. **44**, 2067 (1997).

[95] G. R. Guthöhrlein, M. Keller, K. Hayasaka, W. Lange, and H. Walther, Nature **414**, 49 (2001).

[96] A. B. Mundt, A. Kreuter, C. Becher, D. Leibfried, J. Eschner, F. Schmidt-Kaler, and R. Blatt, Phys. Rev. Lett. **89**, 103001 (2002).

[97] M. Keller, B. Lange, K. Hayasaka, W. Lange, and H. Walther, Nature **431**, 1075 (2004).

[98] D. R. Leibrandt, J. Labaziewicz, V. Vuletić, and I. L. Chuang, Phys. Rev. Lett. **103**, 103001 (2009).

[99] M. Cetina, A. Bylinskii, L. Karpa, D. Gangloff, K. M. Beck, Y. Ge, M. Scholz, A. T. Grier, I. Chuang, and V. Vuletić, New J. Phys. **15**, 053001 (2013).

[100] J. D. Sterk, L. Luo, T. A. Manning, P. Maunz, and C. Monroe, Phys. Rev. A **85**, 062308 (2012).

[101] V. Krutyanskiy, M. Meraner, J. Schupp, V. Krcmarsky, H. Hainzer, and B. P. Lanyon, npj Quantum Inf. **5**, 72 (2019).

[102] H. Walther, B. T. H. Varcoe, B.-G. Englert, and T. Becker, Rep. Prog. Phys. **69**, 1325 (2006).

[103] S. Haroche and J. M. Raimond, *Exploring the Quantum: Atoms, Cavities and Photons* (Oxford University Press, New York, 2006).

[104] A. Reiserer and G. Rempe, Rev. Mod. Phys. **87**, 1379 (2015).

[105] C. H. Nguyen, A. N. Utama, N. Lewty, and C. Kurtsiefer, Phys. Rev. A **98**, 063833 (2018).

[106] Y. Colombe, T. Steinmetz, G. Dubois, F. Linke, D. Hunger, and J. Reichel, Nature **450**, 272 (2007).

[107] D. Hunger, T. Steinmetz, Y. Colombe, C. Deutsch, T. W. Hänsch, and J. Reichel, New J. Phys. **12**, 065038 (2010).

[108] M. Steiner, H. M. Meyer, C. Deutsch, J. Reichel, and M. Köhl, Phys. Rev. Lett. **110**, 043003 (2013).

[109] M. Steiner, H. M. Meyer, J. Reichel, and M. Köhl, Phys. Rev. Lett. **113**, 263003 (2014).

[110] T. G. Ballance, H. M. Meyer, P. Kobel, K. Ott, J. Reichel, and M. Köhl, Phys. Rev. A **95**, 033812 (2017).

[111] H. Takahashi, E. Kassa, C. Christoforou, and M. Keller, Phys. Rev. A **96**, 023824 (2017).

[112] M. Brownnutt, M. Kumph, P. Rabl, and R. Blatt, Rev. Mod. Phys. **87**, 1419 (2015).

[113] M. Hettrich, *Measurement of Reduced Dipole Matrix Elements in $^{40}Ca^{+}$ and Construction of a Scalable Light-Ion Interface*, Ph.D. thesis (2016).

[114] S. Ragg, C. Decaroli, T. Lutz, and J. P. Home, Rev. Sci. Instrum. **90**, 103203 (2019).

[115] K. Ott, S. Garcia, R. Kohlhaas, K. Schüppert, P. Rosenbusch, R. Long, and J. Reichel, Opt. Express **24**, 9839 (2016).

[116] H. Takahashi, E. Kassa, C. Christoforou, and M. Keller, Phys. Rev. Lett. **124**, 013602 (2020).

[117] C. H. Bennett, G. Brassard, S. Popescu, B. Schumacher, J. A. Smolin, and W. K. Wootters, Phys. Rev. Lett. **76**, 722 (1996).

[118] H. Kogelnik and T. Li, Appl. Opt. **5**, 1550 (1966).

[119] A. E. Siegman, *Lasers* (University Science Books, Sausalito, CA, 1986).

[120] W. B. Joyce and B. C. DeLoach, Appl. Opt. **23**, 4187 (1984).

[121] C. J. Hood, H. J. Kimble, and J. Ye, Phys. Rev. A **64**, 033804 (2001).

[122] G. Rempe, R. J. Thompson, H. J. Kimble, and R. Lalezari, Opt. Lett. **17**, 363 (1992).

[123] J. M. Bennett, Meas. Sci. Technol. **3**, 1119 (1992).

[124] B. Brandstätter, A. McClung, K. Schüppert, B. Casabone, K. Friebe, A. Stute, P. O. Schmidt, C. Deutsch, J. Reichel, R. Blatt, and T. E. Northup, Rev. Sci. Instrum. **84**, 123104 (2013).

[125] M. E. Shaheen, J. E. Gagnon, and B. J. Fryer, Laser Physics **24**, 106102 (2014).

[126] A. A. P. Trichet, P. R. Dolan, D. M. Coles, G. M. Hughes, and J. M. Smith, Opt. Express **23**, 17205 (2015).

[127] M. Salz, *Optimierung einer segmentierten Paulfalle mit optischer Schnittstelle*, Master's thesis, Universität Mainz (2013).

[128] R. Albrecht, A. Bommer, C. Pauly, F. Mücklich, A. W. Schell, P. Engel, T. Schröder, O. Benson, J. Reichel, and C. Becher, Appl. Phys. Lett. **105**, 073113 (2014).

[129] D. Kunert, T. Meyrath, and H. Giessen, Appl. Phys. B **98**, 707 (2010).

[130] D. A. Fioretto, *Production of fiber-based cavities by pressing heated balls into fiber tip*, Master's thesis, Universitá degli Studi di Padova (2017).

[131] IVG-Fiber, *Step index multimode fibers*, IVG Fiber, 601 Magnetic Dr., Unit 46 Toronto, Ontario M3J 3J2 Canada (2014).

[132] IVG-Fiber, *Single mode fibers*, IVG Fiber, 601 Magnetic Dr., Unit 46 Toronto, Ontario M3J 3J2 Canada (2014).

[133] NKT-Phonotics, *PCF - LMA 20*, Blokken 84, 3460 Birkerod, Denmark (2014).

[134] NKT-Phonotics, *PCF - LMA 25*, Blokken 84, 3460 Birkerod, Denmark (2014).

[135] MicroSystems-HD, *PI-2525, PI-2555, PI-2556 and PI-2574 Polyimide*, 250 Cheesequake Road Parlin, NJ 08859-1241 (2008).

[136] K. Ott, *Towards a squeezing-enhanced atomic clock on a chip*, Ph.D. thesis, Université Pierre et Marie Curie - Paris VI (2016).

[137] D. Hunger, C. Deutsch, R. J. Barbour, R. J. Warburton, and J. Reichel, AIP Advances **2**, 012119 (2012).

[138] S. Garcia, *Fiber interfaces between single atoms and single photons*, Ph.d. thesis, Ecole normale supérieure - ENS Paris (2015).

[139] S. Garcia, F. Ferri, K. Ott, J. Reichel, and R. Long, Opt. Express **26**, 22249 (2018).

[140] M. Uphoff, M. Brekenfeld, G. Rempe, and S. Ritter, New J. Phys. **17**, 013053 (2015).

[141] Y. Colombe, D. H. Slichter, A. C. Wilson, D. Leibfried, and D. J. Wineland, Opt. Express **22**, 19783 (2014).

[142] C. Deutsch, *High finesse fibre Fabry-Pérot resonators. Production, characterization and applications*, Master's thesis, Fakultät für Physik, Ludwig-Maximilians Universität München (2008).

[143] D. Gangloff, M. Shi, T. Wu, A. Bylinskii, B. Braverman, M. Gutierrez, R. Nichols, J. Li, K. Aichholz, M. Cetina, L. Karpa, B. Jelenković, I. Chuang, and V. Vuletić, Opt. Express **23**, 18014 (2015).

[144] H. A. MacLeod, *Thin-Film Optical Filters* (CRC Press, 2001).

[145] Y. Zhao, Y. Wang, H. Gong, J. Shao, and Z. Fan, Applied Surface Science **210**, 353 (2003).

[146] E. Atanassova, T. Dimitrova, and J. Koprinarova, Appl. Surf. Sci. **84**, 193 (1995).

[147] NKT-Photonics, *Splicing single mode PCFs*, Blokken 84, 3460 Birkerod, Denmark, v1.0 ed. (2009).

[148] J. Gallego, S. Ghosh, S. K. Alavi, W. Alt, M. Martinez-Dorantes, D. Meschede, and L. Ratschbacher, Appl. Phys. B **122**, 47 (2016).

[149] F. Kranzl, *Charakterisierung optischer faserbasierter Fabry-Pérot Resonatoren*, Master's thesis, Leopold-Franzens-Universität Innsbruck (2017).

[150] J. Benedikter, T. Hümmer, M. Mader, B. Schlederer, J. Reichel, T. W. Hänsch, and D. Hunger, New J. Phys. **17**, 053051 (2015).

[151] A. L. Cullen, IEEE Trans. Microw. Theory Tech. **24**, 534 (1976).

[152] T. Martynkien, J. Olszewski, M. Szpulak, G. Golojuch, W. Urbanczyk, T. Nasilowski, F. Berghmans, and H. Thienpont, Opt. Express **15**, 13547 (2007).

[153] H. Takahashi, A. Wilson, A. Riley-Watson, F. Oručević, N. Seymour-Smith, M. Keller, and W. Lange, New J. Phys. **15**, 053011 (2013).

[154] H. Rohde, S. T. Gulde, C. F. Roos, P. A. Barton, D. Leibfried, J. Eschner, F. Schmidt-Kaler, and R. Blatt, J. Opt. B **3**, S34 (2001).

[155] S. T. Gulde, *Experimental Realization of Quantum Gates and the Deutsch-Jozsa Algorithm with Trapped* $^{40}\mathrm{Ca}^{+}$ *Ions*, Ph.D. thesis, Leopold-Franzens-Universität Innsbruck (2003).

[156] M. Guggemos, *Precision spectroscopy with trapped* $^{40}Ca^{+}$ *and* $^{27}Al^{+}$ *ions*, Ph.D. thesis, Leopold-Franzens-Universität Innsbruck (2017).

[157] F. Zähringer, *Quantum walks and relativistic quantum simulations with trapped ions*, Ph.D. thesis, Leopold-Franzens-Universität Innsbruck (2012).

[158] B. Casabone, *Two Ions Coupled to a Cavity: From an Enhanced Quantum Computer Interface Towards Distributed Quantum Computing*, Ph.D. thesis, Leopold-Franzens-Universität Innsbruck (2015).

[159] J. Ghetta, *Über die elektrische Aufladung und Charakterisierung des Ladungszustands von Glasfasern in Paul-Fallen*, Master's thesis (2019).

[160] J. Chiaverini, R. B. Blakestad, J. Britton, J. D. Jost, C. Langer, D. Leibfried, R. Ozeri, and D. J. Wineland, Quantum Inf. Comput. **5**, 419 (2005).

[161] M. Niedermayr, *Cryogenic surface ion traps*, Ph.D. thesis, Leopold-Franzens-Universität Innsbruck (2015).

[162] K. Okada, M. Wada, T. Nakamura, T. Takayanagi, I. Katayama, and S. Ohtani, Jpn. J. Appl. Phys. **45**, 956 (2006).

[163] A. K. Hansen, M. A. Sørensen, P. F. Staanum, and M. Drewsen, Angew. Chem. **51**, 7960 (2012).

[164] M. Drewsen, A. Mortensen, R. Martinussen, P. Staanum, and J. L. Sørensen, Phys. Rev. Lett. **93**, 243201 (2004).

[165] N. B. Khanyile, G. Shu, and K. R. Brown, Nat. Commun. **6**, 7825 (2015).

[166] D. J. Berkeland, J. D. Miller, J. C. Bergquist, W. M. Itano, and D. J. Wineland, J. Appl. Phys. **83**, 5025 (1998).

[167] T. Pruttivarasin, M. Ramm, and H. Häffner, J. Phys. B **47**, 135002 (2014).

[168] J. Keller, H. L. Partner, T. Burgermeister, and T. E. Mehlstäubler, Journal of Applied Physics **118**, 104501 (2015).

[169] C. F. Roos, *Controlling the Quantum State of Trapped Ions*, Ph.D. thesis, Leopold-Franzens-Universität Innsbruck (2000).

[170] H. C. Nägerl, D. Leibfried, F. Schmidt-Kaler, J. Eschner, and R. Blatt, Opt. Express **3**, 89 (1998).

[171] S. Narayanan, N. Daniilidis, S. A. Möller, R. Clark, F. Ziesel, K. Singer, F. Schmidt-Kaler, and H. Häffner, J. Appl. Phys. **110**, 114909 (2011).

[172] Q. A. Turchette, Kielpinski, B. E. King, D. Leibfried, D. M. Meekhof, C. J. Myatt, M. A. Rowe, C. A. Sackett, C. S. Wood, W. M. Itano, C. Monroe, and D. J. Wineland, Phys. Rev. A **61**, 063418 (2000).

[173] M. Harlander, M. Brownnutt, W. Hänsel, and R. Blatt, New J. Phys. **12**, 093035 (2010).

[174] C. Hempel, *Digital Quantum Simulation, Schrödinger Cat State Spectroscopy and Setting Up a Linear Ion Trap*, Ph.D. thesis, Leopold-Franzens-Universität Innsbruck (2014).

[175] R. W. P. Drever, J. L. Hall, F. V. Kowalski, J. Hough, G. M. Ford, A. J. Munley, and H. Ward, Appl. Phys. B **31**, 97 (1983).

[176] E. Black, Am. J. Phys. **69**, 79 (2001).

[177] A. I. Oliva, M. Aguilar, and V. Sosa, Meas. Sci. Technol. **9**, 383 (1997).

[178] I. Sorbothane, *Sorbothane - Engineering Design Guide* (2015).

[179] I. Sorbothane, *Sorbothane - Standard Products Guide* (2015).

[180] R. Stricker, *Gatteroperationen hoher Güte in einem optischen Quantenbit*, Master's thesis (2017).

[181] A. Ryou and J. Simon, Rev. Sci. Instrum. **88**, 013101 (2017).

[182] H. Takashashi, Appl. Opt. **34**, 667 (1995).

[183] A. Stiebeiner, R. Garcia-Fernandez, and A. Rauschenbeutel, Opt. Express **18**, 22677 (2010).

[184] H. Bruining, *Physics and Applications of Secondary Electron Emission* (Pergamon Press / McGraw-Hill Book Co., 1962).

[185] E. Kassa, H. Takahashi, C. Christoforou, and M. Keller, Journal of Modern Optics **65**, 520 (2018).

[186] R. Lechner, C. Maier, C. Hempel, P. Jurcevic, B. P. Lanyon, T. Monz, M. Brownnutt, R. Blatt, and C. F. Roos, Phys. Rev. A **93**, 053401 (2016).

[187] M. K. Joshi, A. Fabre, C. Maier, T. Brydges, D. Kiesenhofer, H. Hainzer, R. Blatt, and C. F. Roos, in preparation (2020).

[188] F. R. Ong, K. Schüppert, P. Jobez, M. Teller, B. Ames, D. A. Fioretto, K. Friebe, M. Lee, Y. Colombe, R. Blatt, and T. E. Northup, New J. Phys. in press (2020).

[189] A. Van Rynbach, P. Maunz, and J. Kim, *Applied Physics Letters*, Appl. Phys. Lett. **109**, 221108 (2016).

[190] C. Guerlin, E. Brion, T. Esslinger, and K. Mølmer, Phys. Rev. A **82**, 053832 (2010).

[191] A. C. J. Wade, M. Mattioli, and K. Mølmer, Phys. Rev. A **94**, 053830 (2016).

[192] J. D. Siverns and Q. Quraishi, Quantum Inf. Process. **16**, 314 (2017).

[193] N. Daniilidis, S. Narayanan, S. A. Möller, R. Clark, T. E. Lee, P. J. Leek, A. Wallraff, S. Schulz, F. Schmidt-Kaler, and H. Häffner, New J. Phys. **13**, 013032 (2011).

[194] K. K. Mehta, C. D. Bruzewicz, R. McConnell, R. J. Ram, J. M. Sage, and J. Chiaverini, Nat. Nanotechnol. **11**, 1066 (2016).

[195] A. Jechow, E. W. Streed, B. G. Norton, M. J. Petrasiunas, and D. Kielpinski, Opt. Lett. **36**, 1371 (2011).

[196] A. M. Eltony, S. X. Wang, G. M. Akselrod, P. F. Herskind, and I. L. Chuang, Appl. Phys. Lett. **102**, 054106 (2013).

[197] A. P. VanDevender, Y. Colombe, J. Amini, D. Leibfried, and D. J. Wineland, Phys. Rev. Lett. **105**, 023001 (2010).

[198] K. Schüppert, R. Blatt, and T. E. Northup, in preparation (2020).

[199] J. Degallaix, J. Phys. Conf. Ser. **228**, 012021 (2010).

[200] N. Podoliak, H. Takahashi, M. Keller, and P. Horak, J. Phys. B **50**, 085503 (2017).

[201] G. K. Gulati, H. Takahashi, N. Podoliak, P. Horak, and M. Keller, Sci. Rep. **7** (2017).

[202] G. D. Cole, W. Zhang, B. J. Bjork, D. Follman, P. Heu, C. Deutsch, L. Sonderhouse, J. Robinson, C. Franz, A. Alexandrovski, M. Notcutt, O. H. Heckl, J. Ye, and M. Aspelmeyer, Optica **3**, 647 (2016).

[203] J.-S. Chen, *Ticking near the Zero-Point Energy: Towards 1 x* 10^{-18} *Accuracy in* Al^{+} *Optical Clocks*, Ph.D. thesis, University of Colorado at Boulder (2017).

[204] S. M. Brewer, J.-S. Chen, A. M. Hankin, E. R. Clements, C. W. Chou, D. J. Wineland, D. B. Hume, and D. R. Leibrandt, Phys. Rev. Lett. **123** (2019)

Acknowledgement – Danksagung

Diese Arbeit konnte ich nur in Zusammenarbeit mit vielen verschiedenen Menschen bewältigen. Daher möchte ich im folgenden allen Professoren, Kollegen, Freunden und Angehörigen, die mich mit ihrer Hilfe, Mühe und Geduld unterstützt haben, meinen Dank aussprechen.

Als erstes möchte ich Prof. Rainer Blatt dafür danken, dass er mir die Forschung und Ausbildung in seiner Arbeitsgruppe ermöglicht hat. Ein großer Teil diesen Danks geht dabei an meine zweite Betreuerin Tracy Northup, die zu Beginn meiner Arbeit als Assistenzprofessorin unter Prof. Rainer Blatt das Cavity-QED geleitet hat. Inzwischen darf ich in ihrer eigenen Forschungsgruppe arbeiten. Vielen herzlichen Dank an euch beide!

Die Sekretariate unterstützen nicht nur unsere Professoren, sondern helfen auch uns Mitarbeitern mit sämlichten bürokratischen Angelegenheiten. Patricia Moser (Prof. Rainer Blatt), Claudia Mevenkamp (Prof. Tracy Northup), Karina Köhl und Michala Palz (SFB), und auch Verena Tanzer und Carina-Therse Sassermann (Institut) halfen mir bei jeglichen noch so kleinen, selbstverschuldeten oder sonstigen Schwierigkeiten.

Eine Vielzahl unserer Arbeit im Labor wird erst durch unseren Werkstätten ermöglicht. Wolfgang Kuen ist und Wolfgang Kratz (RIP) war (wenn auch zu Beginn nur zu ganz bestimmten Zeiten:) bei allen elektronischen Angelegenheiten immer helfende Ansprechpartner. Ohne die mechanische Werkstatt mit Armin Sailer, Christoph Wegscheider, Toni Schönherr und dem ehemaligen Mitarbeiter Helmut "Heli" wäre unser Experiment nie aufzubauen gewesen. Für die Ionenfalle selbst konnten wir glücklicher Weise auch auf die IQOQI Werkstatt und Stefan Haslwanters erfahrene Hände zurückgreifen.

Nach den Worten Rainer Blatts ist das Ganze mehr als die Summe der einzelnen Teile. Getreu diesem Motto habe ich unsere große Arbeitsgruppe als eine riesige Bereicherung empfunden: sowohl wissenschaftlich als auch menschlich. Ich danke also nicht nur jedem Einzelnen der im Laufe meiner Arbeit Kollege war, sondern auch der Arbeitsgruppe als Ganzes und bestens funktionierendes Team. Insbesondere möchte ich mich bei meinen direkten Kollegen im Fibercavity-Projekt bedanken: Birgit Brandstätter für ihre Einführung in die Welt der Faserresonatoren, Florian Ong als langjährigen und fleißigen Postdoc-Kollegen, Pierre Jobez für frischen Wind und immer gute Laune und den Masterstudenten Florian Kranzl und Dario Fioretto, die meine Betreuung ertragen haben. Natürlich bin ich auch sehr erfreut zu sehen, dass das Fibercavity-Projekt von tatkräftigen Nachfolgern weitergeführt wird: Danke Markus Teller und Viktor Messerer. Eng verbunden mit unserem Projekt – auch des öfteren als ein gemeinsames Projekt mit der Fibercavity bezeichnet – möchte ich auch den Kollgen des CQED-Experiments danken: Andreas Stute (Photongenerator), Bernardo Casabone (Zwei-Photon-Experte), Moonjoo Lee (Photonzähler), Konstantin Friebe (Durchgehender Tischnachbar), und der italienischen Verstärkung Maria Galli und Dario Fioretto. Auch dem Nanospheres Team in Tracy Northups neuer Forschungsgruppe möchte ich für die angenehme Zusammenarbeit be-

danken. Besonderer Dank gilt auch allen Kollegen des dritten Cavity-QED Experiments – QFC – im Quantennetzwerk Projekt unter Leitung von Ben Lanyon, denen wir helfen durften ein Experiment neu aufzubauen. Ich konnte dabei selbst viel dazu lernen. Allen weiteren Mitarbeitern unter Rainer Blatt in den zahlreichen Projekten möchte ich natürlich auch meinen herzlichen Dank aussprechen.

Wissenschaftlicher Fortschritt basiert zu einem großen Teil auf Austausch. In meinem Fall hat sich dieser Austausch nicht nur auf die über 70 Mitarbeiter meiner Arbeitsgruppe(n) beschränkt. Für die Herstellung unserer Faserspiegel durfte ich in der Arbeitsgruppe von Prof. Jakob Reichel in Paris arbeiten. In der mehrwöchigen Kollaboration lernte ich Konstantin Ott und Sebastién Garcia nicht nur als Arbeitskollegen sondern auch als Freunde kennen: Vielen Dank für die schöne Zeit in Paris. Meine Erfahrungen durfte ich daraufhin weitergeben. Als erstes löcherte mich Sudheer Vanga von Prof. Randall Goldsmith aus Wisconsin mit Fragen über die Herstellung von Faserspiegeln. Als zweites fragte Klara Theophilo aus Zürich nach, wie man Faserresonatoren baut. Ihr Professor Jonathan Homes arbeitet schon seit mehreren Jahren mit Prof. Rainer Blatt zusammen, sodass wir ein paar unserer Faserspiegel zum Testen zur Verfügung stellten. Später unterstütze ich dann auch Thomas Lutz und Simon Ragg bei weiteren Versuchen mit unseren Fasern und der Herstellung eigener Fasern. Vielen Dank für diese überaus angenehmen Kollaborationen!

Neben der Arbeit gab es aber auch genügend Gelegenheit Arbeitskollegen privat kennenzulernen. Insbesondere möchte ich hier unsere Gurken-Gruppe erwähnen. Beachtliche 123 Gurkengläser konnten wir in den letzten zwei Jahren bei unseren "Jaus'n" sammeln: Gratulation und Danke! Allein hätte ich das nie vollbringen können. Dabei haben wir auch tatkäftige Unterstützung aus der Privatwirtschaft erhalten: Danke AQT! Viel Spaß und Tiroler Brauchtumslehre habe ich auch noch in der Führungskräfte-Tarockrunde genossen. Vielen Dank an: Alexander Axel Erhard, Lukas Postler, Martin Meraner, Marian Kremser (Ultracold-AG), and Sven Arne Schiller (Angewandte-Institut).

Zuletzt möchte ich mich noch bei meiner Familie bedanken. Danke liebe Eltern, Barbara und Heiner, dass ihr mir bei all meinen Wünschen bis hin zu dieser Arbeit hinter mir standet. Inzwischen habe ich zwei weitere Eltern, meine Schwiegereltern Ulli und Hago, denen ich auch großen Dank aussprechen möchte: nicht nur für die Hilfe in der Finalen Phase dieser Arbeit. Last but for sure not least danke ich noch meiner Großen Liebe und inzwischen Ehefrau Lilli für ihre stetige Unterstützung, insbesondere auch für unsere Tochter Luise, die mich vielleicht auch ein wenig abgelenkt, aber hauptsächlich doch motiviert hat.